Max-Planck-Institut für Metallforschung
Stuttgart

Synthesis and adhesion of biomimetic contact elements

Holger Pfaff

Dissertation
an der
Universität Stuttgart

Bericht Nr. 191
Februar 2006

Synthesis and adhesion of biomimetic contact elements

Von der Fakultät für Chemie der Universität Stuttgart
zur Erlangung der Würde eines Doktors der
Naturwissenschaften (Dr. rer. nat.) genehmigte Abhandlung

Vorgelegt von

Dipl.-Ing. Holger Pfaff

aus Aschaffenburg

Hauptberichter:	Prof. Dr. phil. Eduard Arzt
Mitberichter:	Prof. Dr. rer. nat. Ralph Spolenak
Tag der mündlichen Prüfung:	09.02.2006

Institut für Metallkunde der Universität Stuttgart und
Max-Planck-Institut für Metallforschung Stuttgart

Stuttgart, Februar 2006

Dedicated to

Prof. Dr. Gerd Busse

and

Dr. Roland Full

in grateful recognition of their

inspiration and encouragement

Abbreviations and Symbols

a	contact radius [m]
A	contact area [m²]
AFM	atomic force microscope
b	bridging distance between two counter surfaces [m]
c	relative cohesive zone length [ ]
δ	penetration depth [m]
Δx	absolute error
DMT	Derjaguin-Muller-Toporov model
DRIE	deep Reactive Ion Etching
DUV	deep UV lithography
E^*	reduced Young's modulus [Pa]
E_{eff}	effective stiffness of a fiber mat [Pa]
E_{detach}	energy for detaching a single fiber [J]
F_c	pull-off force [N]
f	pillar density [-]
FIB	focused ion beam
φ	viscoelastic dissipation function [ ]
F_i	load on a fiber within an annulus i [N]
$F(r)$	profile function depending on radius r [m]
G	energy release rate [J/m²]
G_c	critical energy release rate [J/m²]
γ, γ_{eff}	work of adhesion, effective work of adhesion [J/m²]
γ'	work of adhesion between two fibers [J/m²]
JKR	Johnson-Kendall-Roberts model of adhesion
K	reduced Stiffness according to Hertz [Pa]
K_I	stress intensity factor for crack opening mode 1 [ ]
K_m	stress intensity factor for cohesive forces in a crack [ ]
λ_T, μ	transition parameter (Maugis, Tabor) for *DMT-JKR*
λ	aspect ratio [ ]
LEFM	linear elastic fracture mechanics

LIGA	X-ray based lithography method (*FZK* Karlsruhe)
MEMS	micro-electro-mechanical systems
MWNT	multi walled carbon nano tubes
n	number of contacts [ ]
P	applied load [N]
PDMS	polydimethylsiloxane
PMMA	polymethylmetacrylat
PVS	polyvinylsiloxane
q	number of tests
R	radius of curvature [m]
r_i	radius of ring I to the central loading point of an indenter
RIE	reactive Ion Etching
SEM	scanning electron microscopy
σ_{th}	theoretical strength [Pa]
s	standard deviation
SSLS	Singapore Synchrotron Light Source
SU-8	photo resist
T_g	glass transition temperature [°C]
x	coordinate [ ]

Holger Pfaff:

Synthesis and adhesion of biomimetic contact elements

Institute of Physical Metallurgy, University of Stuttgart and
Max-Planck-Institue for Metals Research Stuttgart, 2005
152 pages, 85 figures, 12 tables

Abstract:

The ability of different animals to walk along ceilings and walls has inspired basic research in order to understand the underlying mechanisms as well as efforts to transfer the working principles to technical products as new dry adhesives. The clinging capabilities result from highly sophisticated fibrillar attachment microstructures under the animal feet.
Several groups have fabricated and tested biomimetic attachment samples. Although there are various contact element geometries in biology, the influence of shape has not been addressed in previous research. In this study a Focused Ion Beam technique was introduced for predefining contact element shapes. The milling of arbitrarily shaped molds and indentation tips was achieved by implementing a software tool for a commercial *FIB* FEI 200™ focused ion beam microscope. The method yields specifically shaped single micro contact elements as well as of periodic arrays. The feasibility of hierarchical structures was also demonstrated. Specimens were characterized using light microscopy, *SEM* and *FIB* as well as white light profilometry.
Adhesion measurements were performed with a modified commercial nanoindenter XP™ (MTS Systems Corporation, Oak Ridge, USA), thus spanning the force and size range gap between coarse load-cell techniques and *AFM* measurements. A procedure for highly automated testing of biomimetic prototypes with sub-µN force and nm displacement resolution was established. The capability of measuring specimens only a few hundred µm² in cross-sectional area resulted in a reduced production effort in sequential fabrication processes. Experiments were performed to experimentally verify the influence of contact element shape and size and to contribute to better understanding of the attachment and detachment mechanisms of bioinspired fibrillar attachment.

The scaling behavior of adhesion forces in microscopic single contacts was determined for spheres and flat punches. It agrees well with contact mechanic estimates. Measurements on microscopic pillar structures were also performed to investigate the collective attachment behavior of fibrillar structures. A numeric model for describing the detachment dynamics of a fibrillar structure was derived. The modelled forces of the single detachment events match the experimental results well. The influence of surface modification was determined for oxidation and fluorosilanisation. In this context, a qualitative model was intoduced to explain the unexpectedly high adhesion forces on fluorinated polymer surfaces.

Synthesis and adhesion of biomimetic contact elements

Institut für Metallkunde, Universität Stuttgart und
Max-Planck-Institut für Metallforschung Stuttgart, 2005
152 Seiten, 85 Abbildungen, 12 Tabellen

Die Fähigkeit verschiedener Tiere an Decken und Wänden entlangzulaufen, hat Untersuchungen zu den grundlegenden Mechanismen angestoßen und den Wunsch geweckt, die Funktionsweisen auf neuartige trockene Klebstoffe zu übertragen. Die Hafteigenschaften sind das Ergebnis hoch komplexer Mikrostrukturen an den Füßen der Tiere. Mehrere Forschungsgruppen haben biomimetische Haftstrukturen hergestellt und deren Haftung untersucht. Obwohl in der Biologie vielfältig geformte Kontaktelemente vorkommen, wurde der Einfluss der Geometrie bisher nicht experimentell untersucht. In der vorliegenden Arbeit wurde eine Methode zur Herstellung definierter Kontaktelemente mit dem fokussierten Ionenstrahlmikroskop eingeführt. Durch ein eigens entwickeltes Computerprogramm für ein kommerzielles *FIB* FEI 200™ Ionenstrahlmikroskop, konnten beliebig geformte Mikrogussformen und Indenterspitzen erzeugt werden. Mit dem Verfahren lassen sich sowohl einzelne Kontaktelemente als auch periodische Anordnungen von Einzelkontakten herstellen. Ferner wurde die Fertigung hierarchischen Säulenstrukturen demonstriert. Die Proben wurden mittels Lichtmikroskopie-, Rasterelektronen-, Ionenstrahlmikroskopie und Weißlichtprofilometrie charakterisiert.

Durch den Einsatz eines modifizierten kommerziellen Nanoindenters XP™ (MTS Systems Corporation, Oak Ridge, USA) für die Adhäsionsmessungen, konnte die Kluft zwischen groben Lastzellenmessungen und der Rasterkraftmikroskopie geschlossen werden. Es wurde ein Verfahren für hochautomatisierte Untersuchungen an biomimetischen Prototypen mit einer Kraftauflösung Submikronewtonbereich und einer Weggenauigkeit im Nanometerbereich etabliert. Durch die Möglichkeit, die Haftung von Proben mit einer Ausdehnung von nur einigen hundert Nanometern zu messen, reduziert sich der Aufwand für die Herstellung von Prototypen bei sequentiellen Strukturierungsverfahren.

Es wurden Messungen durchgeführt, um den theoretischen Einfluss von Größe und Geometrie der Kontaktelemente zu verifizieren, und um ein besseres Verständnis der Haftungs- und Lösungsmechanismen bei biomimetischen Haftstrukturen zu erzielen.

Das Skalierungsverhalten der Adhäsion in mikroskopischen Kontakten wurde für Halbkugeln und Stempel unterschiedlicher Durchmesser bestimmt. Es stimmt gut mit kontaktmechanischen Vorhersagen überein. Mit weiteren Messungen wurde das kollektive Haftverhalten mikroskopischer Säulenstrukturen untersucht. Es wurde ein numerisches Modell zur Beschreibung des Ablösevorgangs erstellt, welches die Kräfte der einzelnen Ablösevorgänge gut beschreibt. Außerdem wurde das Haftverhalten oberflächenbehandelter Kontakte untersucht, bei denen eine Oxidation bzw. eine Silanisierung mit einem Perfluorsilan durchgeführt wurde. In diesem Zusammenhang wurde ein qualitatives Modell vorgestellt, um die unerwartet hohen Haftkräfte bei fluorterminierten Kunststoffoberflächen zu erklären.

1 Introduction

In nature a variety of animals possess the capability of freely walking along walls and ceilings as their feet are equipped with hairlike attachment structures. These devices adhere and detach rapidly thousands of times, generating adhesion forces easily carrying the animal's body weight almost independently of the surface properties. Although the mechanisms of biological dry adhesion have been under scientific discussion for more than a century, the highly complex biological attachment systems have not yet been completely understood. Recent research has improved scientific understanding of the underlying physics [1-5]. As the influence of parameters such as stiffness, surface energy, geometry is not easily studied with living animals, synthetic bioinspired structures are applied for systematic parameter studies. Experiments on these samples with well-specified properties aim at a better understanding of biology as well as at extracting design principles for high- performance technical adhesives.

In contrast to biological attachment devices, common pressure sensitive adhesives (sticky tapes) are prone to particle contamination and the adhesion forces generated are much lower than in bioattachment. Biological devices attach and detach for thousands of times without a decrease in adhesion performance [6].

Recent research work mainly focuses on extracting adequate design rules [3, 4, 7] for bioinspired high performance adhesives . Further progress in the field of biomimetic adhesion requires adequate methods for the fabrication of complex well-defined synthetic attachment prototypes as well as methods for well specified adhesion measurements on the respective structures. Then the influence of material and geometry parameters can be selectively studied by systematically varying one specific sample property without changing the others.

The research on biological attachment devices is driven by two quite dissimilar but not opposing aims: Biology focuses on a detailed understanding of the biological systems and functionalities, whereas engineering science is interested in ways of improving technical products by extracting biological construction principles and solutions. Only by close cooperation may the complexity of the biological attachment systems be fully unraveled.

2 Motivation and Literature Review

2.1 Attachment Devices: Observations from Biology

Being the biggest animals in nature with highly developed clinging abilities, lizards are particularly interesting, but not unique for adhesion studies. Deeper scientific interest in the morphology and function of lizard contact systems goes back to the end of the 19th century with Tornier [8] (taken from [9]) suggesting vacuum as a source for the adhesive properties. Adhesion forces were proposed in 1900 by Haase [10] (taken from [9]). Other approaches considered electrostatic forces and hooking as possible mechanisms. A detailed overview is given by Hiller [9], who revealed the hierarchical design of the gecko attachment system using an *SEM* and separated adhesion from claw force contributions. By determining contact angles of water on different test surface and relating them to the maximum tensile forces a Gecko can sustain without detaching form the respective substrate, he found a linear function between contact angles and pull-off forces. The experiments give first experimental evidence for van der Waals forces causing adhesion.
Hiller also remarked that gecko adhesion is more a dynamic than a static process. He observed that the gecko feet frequently lose and reestablish contact when clinging to a ceiling. Gecko adhesion accordingly has to be seen as a complex interplay between system design and biomechanics.

In similar ways the adhesion of spiders [11], beetles [12], and flies [13] was studied. Biological adhesion systems generally are based on the principle of split contact pads and hierarchal design, despite the diversity of biological attachment systems. As lizards produce particularly high adhesion forces, the following sections will strongly focus on gecko adhesion.

2.1.1 Biological Adhesion

As already proposed by Haase in 1900 [10], van der Waals forces were recently rediscussed as basis for biological adhesion. Combining biological observations and classical contact mechanical considerations, Arzt *et al.* [1] demonstrated the benefits of contact splitting, as found in biology, for enhancing adhesion. Autumn *et al.* [2] gave evidence for van der Waals adhesion in gecko attachment systems by testing the gecko clinging ability on hydrophilic and

hydrophobic surfaces. Adhesion was found to be independent of hydrophilicity. The polarizability of the substratum material plays an important role. As a consequence, the predominance of van der Waals forces was suggested. In a further experiment, the adhesion force of a single seta was measured, yielding adhesion forces that could also be well explained with van der Waals interactions. In contrast to Autumn *et al.* capillary forces due to atmospheric humidity have been found to play a significant role for gecko adhesion as stated by Huber *et al.* [14]. In the gecko no evidence for secretion was given, but moisture in ambient atmosphere could contribute to local capillary effects [14, 15].

2.1.2 Contact Element Shape

Biological contacts are commonly divided into sub contacts, the ends of hairs or lamellae often forming several hierarchical levels. Diverse contact geometries exist, seemingly resulting from the adaptation to a specific purpose (e.g. locomotion, mating) and environment (e.g. dry, wet, diverse plant surfaces) (Figure 2-1).

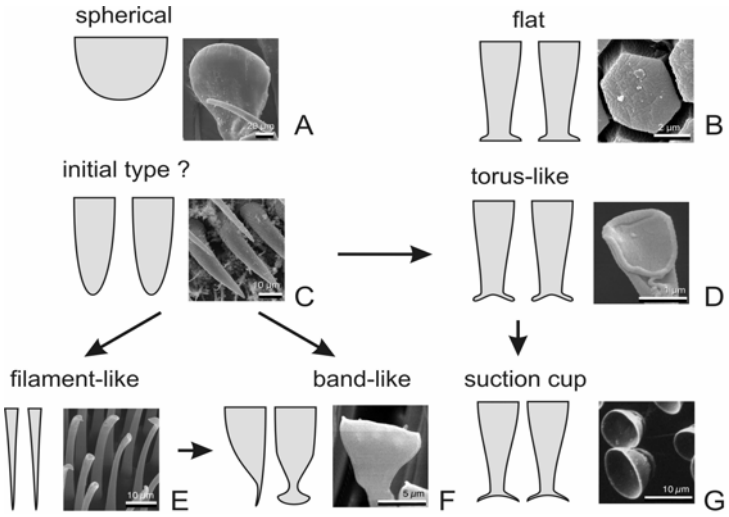

Figure 2-1:Diversely shaped biological contact elements [5] of bugs: Pyrrhocoris apertus (A), grasshoppers: Tettigonia viridissima (B), flies: Myathropa florea (C) Calliphora vicina (D) Harmonia axyridis, beetles: (E) and Chrysolina fastuosa (F)

Spherical contacts are found in bugs like Pyrrhocoris apertus (A). Flat contacts are typical for grasshoppers as Tettigonia viridissima (B). A simple parabolic shape as found in the fly Myathropa florea is (C) considered as a possible evolutionary prototype of contact [5], from which more specific contact elements like the toruses observed in the fly Calliphora vicina (D) and filaments and bands in on the second tarsal segment of certain beetles like Harmonia

axyridis (E) and Chrysolina fastuosa (F). Similar to toric structures, suction cups cover the vertical side of the foreleg tarsi of Dytiscus marginatus male beetles. The variety of contact shapes well indicates some potential for improving the adhesion properties by adequate design.

2.1.3 Hierarchy

Biological attachment devices commonly consist of several levels of hierarchy. Again geckoes are representative for demonstrating this important feature. The morphology will be described in this section, whereas the physical implications and possible functions are treated in section 2.2.5.

The gecko foot pad bears a number of parallel flexible lamellar scansors (Figure 2-2) covered with rectangular clusters (Figure 2-3) of adhesive hairlike setae [16]:

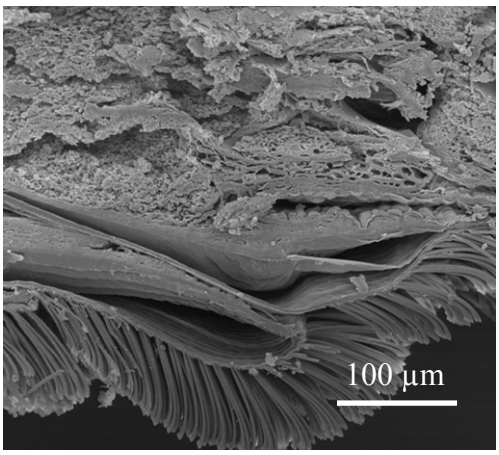

Figure 2-2: Cross section of a lamellar scansor of a gecko bearing hairlike seta structures [16]

The scansor lamella consists of a sponge like material with various channels or pores. The spongeous layer can be considered as one distinct level of hierarchy allowing for the adaptation of the attachment pad to waviness and coarse roughness. Thus the seta, covering the scansors, are positioned close to the counter surface. The Seta clusters cover areas of approximately 5x5 µm².

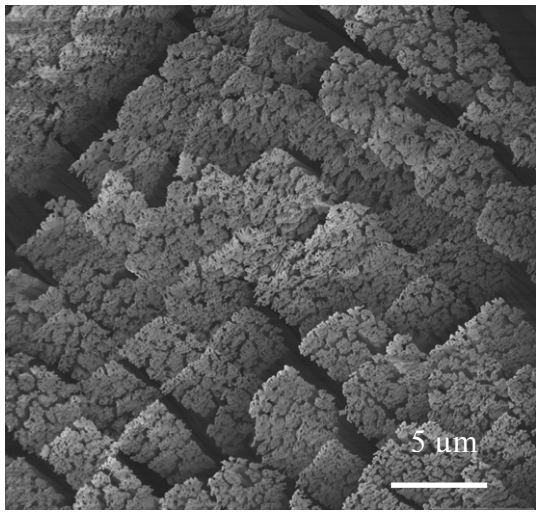

Figure 2-3: Rectangular clusters of Gecko setae (*SEM* micrograph by Dr. S. Gorb [16])

The approximately 100 µm long setae end in a brush of finer hairs terminated with the contact elements (Figure 2-4). These spatulae are only about 300 nm in diameter and flatten out towards the contact elements.

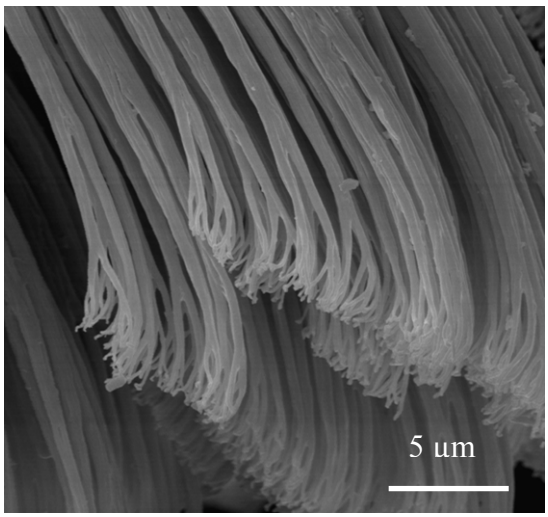

Figure 2-4: Gecko seta with spatulae as terminal contact elements [16]

In a closer look at a single seta, a rough core is found with protruding hairs (Figure 2-5). The surface relief ridges resemble the protrusions in size and have a diameter of a few hundred nm.

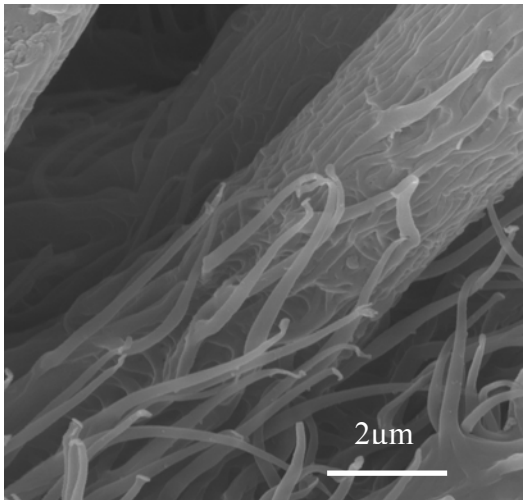

Figure 2-5: Rough core of a gecko seta [16]

2.1.4 Self-Cleaning

In contrast to manmade pressure sensitive adhesives, biological attachment pads are not contaminated significantly by dust particles. Self-cleaning has been discussed in the bio-attachment community and evidence for this phenomenon was provided by Hansen *et al.* [6]. The authors propose a kind of lotus effect and apply a model for the surface-particle- seta interactions similar to the model used by Rollot *et al.*[17]. Self-cleaning is expected when the interaction forces between the surface and the particle exceed those between particle and a single seta. Self-cleaning is a challenging goal for bioinspired adhesives, as a major disadvantage of classical pressure-sensitive adhesives could be overcome: The adhering interface could be de- and reattached for thousands of times without suffering a loss in adhesion due to contamination.

2.2 Mechanics of Adhesive Contacts

Understanding the adhesion of biological and biomimetic attachment devices requires a way of describing and modeling a complex system on all of its hierarchical levels, starting from the single contact element up to the mechanics of the whole system. Although being very diverse (section 2.1.2), certain design principles, e.g. hierarchical fibrillar attachment systems, are found universally among different clinging animals (see section 2.1). The following chapters describe and discuss the function of some of the mentioned features.

2.2.1 Single Contacts and Contact Splitting

In a contact between two perfectly conforming surfaces the energy per area to break the contact equals the theoretical strength, determined by interatomic or intermolecular short and long range forces. As real geometries commonly result in an inhomogeneous distribution of stresses and are sensitive to imperfections, real contact strength ranges between zero and the theoretical contact strength [4, 18]. Hence the description of contact strength implies knowledge of the deformations and stresses within the contacting solids.
Hertz [19] pioneered the field of contact mechanics in 1882 by quantitatively investigating the contact between two glass lenses at different loads P (Figure 2-6).

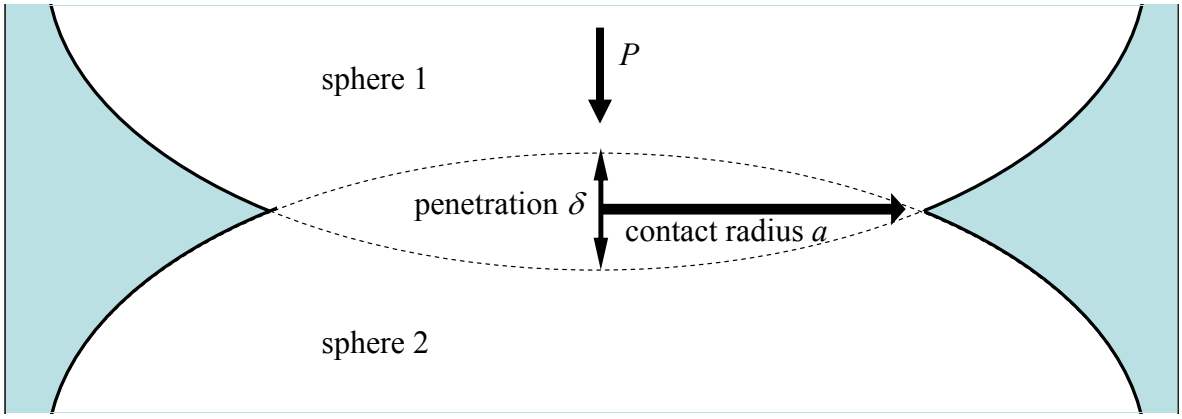

Figure 2-6: Hertz configuration: Two lenses pressed into contact by a force *P* at a penetration depth δ and a contact radius *a*

Two elastic lenses are pressed into contact over the contact radius *a* by an external load *P*, leading to a deformation of the lenses given by the elastic displacement *δ*. In the following this displacement will be called penetration depth as by Maugis *et al.* [20] The contact radius *a* relates to the applied load *P* as:

$$a^3 = \frac{RP}{K} \qquad (2\text{-}1)$$

with the reduced stiffness *K*:

$$\frac{1}{K} = \frac{3}{4}\left(\frac{1-\nu_1^2}{E_1} + \frac{1-\nu_2^2}{E_2}\right) \qquad (2\text{-}2),$$

calculated for Young's Moduli E_i and Poisson ratios v_i for the contacting materials *i*. *R* stands for the reduced radius of curvature *R*:

$$\frac{1}{R} = \frac{1}{R_1} + \frac{1}{R_2} \qquad \text{(2-3)},$$

where R_i is the radius of curvature of lens *i*.

The penetration depth δ is given by:

$$\delta = \frac{a^2}{R} = \frac{P}{Ka} \qquad \text{(2-4)}$$

These equations are still in use for adhesionless contact and for high load indents, as the adhesive contribution then becomes negligible. The sample deformations under a rigid tip are not given by the Hertz equations. Sneddon [21] gave a solution for the penetration depth under axisymmetric punches based on a model proposed by Boussinesq [22]:

$$\delta = \int_0^1 \frac{f'(x)dx}{\sqrt{1-x^2}} + \frac{\pi}{2}\chi(1) \qquad \text{(2-5)}$$

with the force:

$$P = \frac{3aK}{2}\left[\delta - \int_0^1 \frac{xf(x)dx}{\sqrt{1-x^2}}\right] \qquad \text{(2-6)}$$

The derivative *f'(x)* defines the indenter profile slope depending on the lateral coordinate *x*. The parameter χ represents a rigid body displacement, commonly introduced in contact mechanics to account for adhesive interactions. The mentioned models do not account for surface interactions. Johnson-Kendall-Roberts [23] and Derjaguin-Muller-Toporov [24] derived adhesive contact models for spheres in contact with a reduced radius *R*. The *DMT* model considers undeformable spheres with a reduced radius R in contact, attracting each other by interactions outside the contact area. *DMT* provides the following equations for the adhesion force F_c and contact radius *a*:

$$F_c = 2\pi\gamma R \qquad (2\text{-}7)$$

$$a^3 = (P + 2\pi R\gamma)\frac{R}{K} \qquad (2\text{-}8)$$

where the work of adhesion γ is the work done in separating a unit of two contacting surfaces. The penetration depth δ is given by Hertz (2-4). In contact mechanics tensile loads are negative by definition. In the following, the pull-off force F_c always represents the absolute value of the pull-off force, thus being positive. In force vs. displacement and force vs. time plots the pull-off force will nevertheless be displayed as a negative value.

In contrast, the *JKR* theory considers contact deformation but neglects attractive forces outside the contact. It equilibrates the potential energy, the elastic stored energy and the surface energy, according to the Griffith equilibrium criterion

$$G = \gamma \qquad (2\text{-}9),$$

where the energy release rate G corresponds to the work of adhesion γ.
The contact of area A becomes unstable for

$$\frac{\partial G}{\partial A} < 0 \qquad (2\text{-}10).$$

The following equations are found for the pull-off force, contact radius and penetration depth:

$$F_c = m\pi\gamma R \qquad (2\text{-}11)$$

The factor m = 3/2 holds for fixed load condition, whereas 5/6 has to be used for fixed grips, as the stability conditions are different in both cases [20]. The contact radius is given by

$$a^3 = \frac{R}{K}(P + 3\gamma R\pi + \sqrt{6\gamma\pi PR + (3\gamma R\pi)^2}) \qquad (2\text{-}12)$$

The penetration depth δ is

$$\delta = \frac{a^2}{R} - \frac{2}{3}\sqrt{\frac{6\pi\gamma a}{K}} \qquad (2\text{-}13)$$

Neither the lack of tip deformation in *DMT* nor the stress singularities in *JKR* theory due to neglecting attraction outside contact are physical, but approximate experiments under specific conditions. Scientific controversy about the correct model lasted until Tabor [25] proved that both theories were valid boundary cases of adhesive contact. He introduced a dimensionless transition parameter μ for the range between the models. A more generalized theory with the transition parameter λ_t for an interatomic equilibrium distance of z_0 was given by Maugis [20]:

$$\lambda_t = \frac{2.06}{z_0}\sqrt[3]{\frac{R\gamma^2}{\pi K^2}} \qquad (2\text{-}14)$$

The calculations were based on results of Dugdale [26] and Barenblatt [27] for the distribution of cohesive forces near the crack tip. The cohesion within the cohesive zone leads to a stress intensity factor K_m counterbalancing the stress intensity factor due to external loading K_I. The Dugdale model considers a constant stress equal to the material yield stress allover the cohesive zone *c* (Figure 2-7), described by a square well potential (Figure 2-8 b).

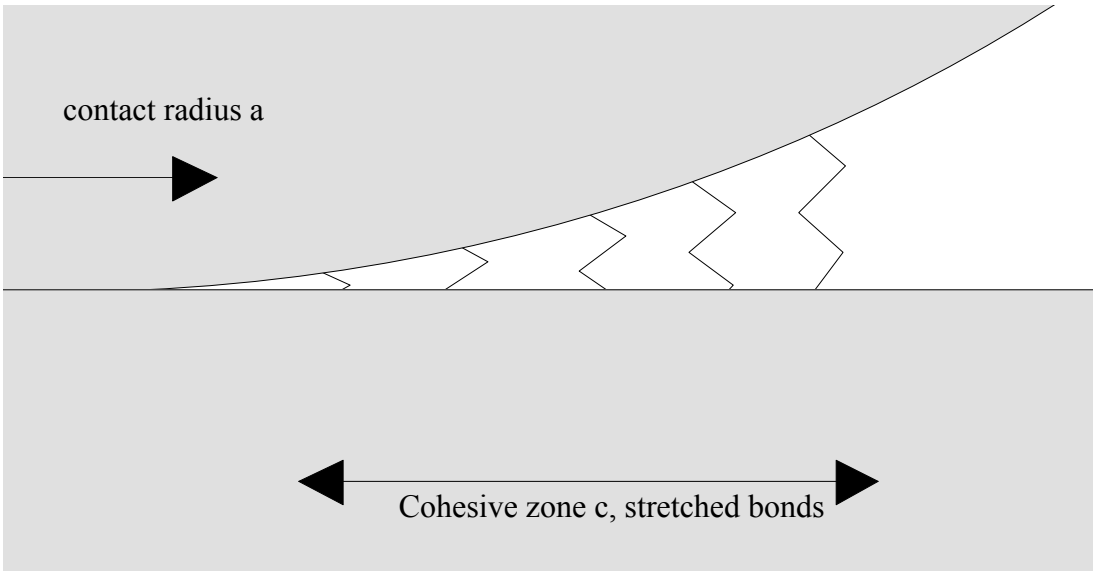

Figure 2-7: Crack analogy in contact mechanics: Contact radius a with undeformed bonds in equilibrium position and stretched bonds within the cohesive zone a<r<c

The overall fracture energy herein matches that of the interaction potential (e.g. Lennard-Jones) (Figure 2-8 a).

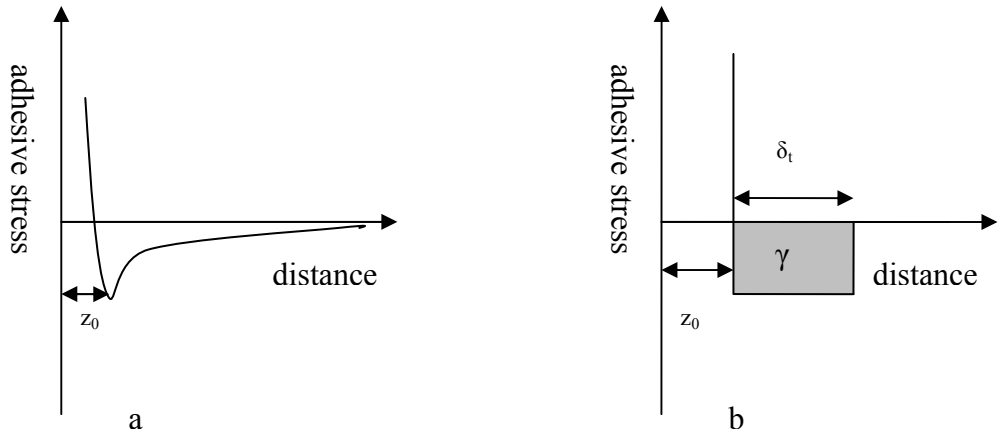

Figure 2-8: Force- Distance potential models: a) actual potential, b) Dugdale square-well potential

Beyond the cohesive zone no stresses are transferred between the two surfaces. *DMT* applies for $\lambda_t \rightarrow 0$ corresponding to a wide cohesive zone c, whereas *JKR* is valid for $\lambda_t \rightarrow \infty$, the cohesive zone *c* being short. For c/*a* $\rightarrow$1 the stress intensity factor K_I approaches zero, thus resulting in a homogeneous stress state as in *DMT*. The theory was supported by numerical calculations [28-30]. For a simplified evaluation of experimental data Carpick *et al.* [31] proposed a way of approximating the Maugis model by a generalized equation. Spolenak *et al.* [5] mapped the regime of biological contact elements within the framework of *JKR*-*DMT* transition (Figure 2-9). In general, *JKR* is valid for contacts of compliant materials, great contact radii and high work of adhesion, whereas *DMT* describes stiff materials, small radii and with a low work of adhesion.

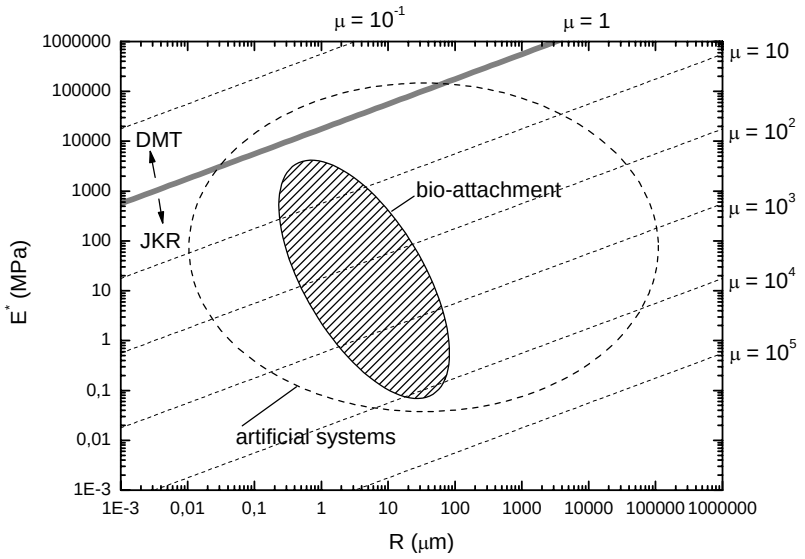

Figure 2-9: Tabor parameter (equation (2-28)) for various reduced material stiffnesses E^*: Bioattachment devices located in the *JKR*- regime [5]

The property map plots the material stiffness vs. the contact element radius. Constant Tabor parameters μ are depicted by inclined dotted lines. The transition between *JKR* and *DMT* is considered for μ=3. Biological contact elements clearly range within the *JKR* domain. The area confined by a broken line maps the estimated range for artificial biomimetic contact devices. Artificial contact element properties may also reach into the *DMT* regime.

2.2.2 Influence of Viscoelasticity and Pull-off Rate

Peeling experiments on polymers [32, 33] revealed that pull-off forces of viscoelastic contacts are rate and temperature dependent. Considering the Griffith model, a crack is subjected to a driving force given by the difference between the energy release rate and the work of adhesion, $G - \gamma$, per unit crack length when $G > \gamma$. This force is counterbalanced by material dependent viscoelastic drag forces. These forces increase with deformation velocity and decrease with temperature. The results at different temperatures relative to the material glass transition temperature T_g can be condensed on a master curve, applying the Williams-Landel-Ferry (*WLF*) shift factor [34]:

$$\log a_T = -\frac{17.4(T - T_G)}{51.6 + T - T_G} \qquad (2\text{-}15).$$

Viscoelastic drag slows down the crack, which leads to a contact area exceeding that of equilibrium. Compared to quasi-static conditions, higher forces are needed to propagate the crack. The forces are limited by the surface interactions and are therefore proportional to the work of adhesion:

$$G - \gamma = \gamma\varphi(a_T v) \qquad (2\text{-}16)$$

where φ is a dimensionless function of temperature and crack velocity v for the dissipation localized at the crack tip. By transforming (2-16), an effective work of adhesion γ_{eff} is calculated [35]:

$$G = \gamma(1 + \varphi(a_T v)) = \gamma_{eff} \qquad (2\text{-}17)$$

After determining φ, the detachment kinetics can be computed. Alternatively the influence of viscoelasticity can be modeled by including stress relaxation and creep in the calculation of stress distribution in the contact area and vicinity. Time dependent stress relaxation and creep functions then replace the quasistatic material properties. Recently several groups have worked out models to describe the advancing and receding contact of viscoelastic spheres [36-41]. Analytical solutions are not sufficient to describe the problem and numerical calculations are necessary. An analytical approximation for the pull-off force vs. retraction velocity relation based on *JKR* and *DMT* has been introduced by Barthel *et al.* [42]. The procedure yields an effective work of adhesion including viscoelastic losses. As a consequence comparable measurements are to be performed at a constant speed. The thermodynamic work of adhesion has either to be determined at very low speeds or by extrapolation of data measured at various velocities.

2.2.3 Scaling of Different Contact Element Shapes

Based on the biological observations Arzt *et al.*[1, 43] and Autumn *et al.* [44] proposed a benefit for adhesion by splitting a contact into finer sub contacts. When the projected area of a single contact is fully divided into n smaller self-similar contacts, the pull-off force is:

$$P'_c = \sqrt{n} P_c \qquad (2\text{-}18)$$

where P'_c stands for the pull-off force of the divided contact in contrast to the pull-off force of the original contact P_c. This equation was derived for self similar contacts (Figure 2-10 a), where the radius of curvature for each contact element equals the contact element radius. The split contacts could also retain the radius of curvature of the original unsplit contact (Figure 2-10 b). For this curvature invariance the exponent for n changes from ½ to 1.

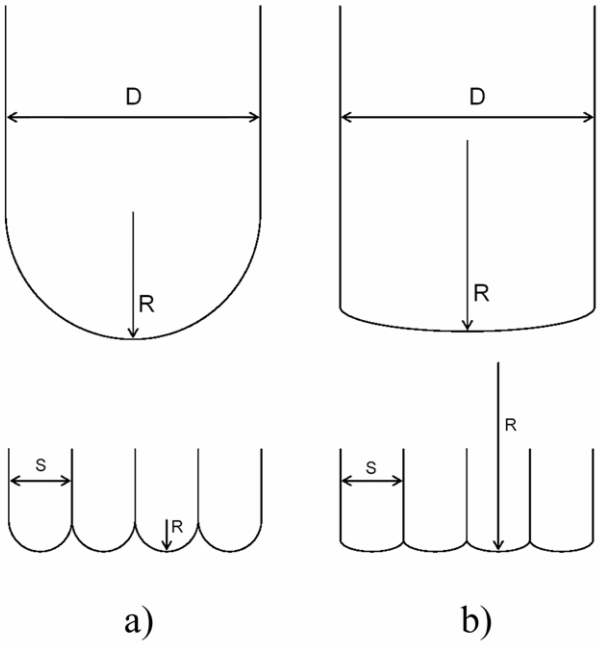

Figure 2-10: Two varieties of splitting up a convex contact with a radius of curvature *R*
a) Self-similar scaling, b) Curvature invariant scaling (from [43])

The benefit of contact splitting follows from the fact that non-conforming contacts generate a true contact size much smaller than the projected contact element area. By reducing the radius of the single contact, the individual contact area is reduced, but parallely the number of contact increases, leading to a net increase of the total contact area. Applying fracture mechanic models, Spolenak *et al.* [5] determined the theoretical scaling behavior of adhesion forces in diversely shaped single contacts. The scaling potential was computed for arrays of such structures. Calculations were performed for spheres, cylindrical punches, toruses, suction cups, elastic bands and generalized axisymmetric punches, either using an energy balance as in *JKR* or the equivalent linear elastic fracture mechanics (*LEFM*) approach, where the stress intensity factor K_I is related to the energy release rate G *by*

$$G = \frac{1}{2E^*} K_I^2 \qquad (2\text{-}19)$$

with E^* defined by

$$\frac{1}{E^*} = \left(\frac{1-\nu_1^2}{E_1} + \frac{1-\nu_2^2}{E_2} \right) = \frac{4}{3} \frac{1}{K} \qquad (2\text{-}20).$$

In the latter case the contact detaches at a critical energy release rate G_c which equals the work of adhesion. Here only two examples are mentioned for illustration. A spherical contact yields the *JKR* adhesion for fixed load (2-11). Toric contacts are treated as looped lying cylinders as computed by Chaudhury *et al.* [45]. For a self similar torus with the radius of curvature r equal to a tenth of the ring radius R, the pull-off force F_c is [5]:

$$F_c = \quad 1.1(\pi E^* \gamma^2)^{\frac{1}{3}} \pi R^{\frac{4}{3}} \qquad (2\text{-}21).$$

The following chart lists the relationship between the adhesion forces F_c of a single contact and the parameters radius, reduced Young's modulus and work of adhesion for selected geometries with feature radius R, stiffness E^* and work of adhesion γ:

Table 2-1: Functional dependencies of selected contact shapes (adapted from [5])

	Hemisphere	**Torus**	**Flat punch**	**Suction cup**
$P \sim R^s$	**1**	**4/3**	**3/2**	**2**
$P \sim E^m$	**0**	**1/3**	**1/2**	**0**
$P \sim \gamma^k$	**1**	**2/3**	**1/2**	**0**

The scaling behavior is visualized by a double-logarithmic plot of the pull-off force F_c for a specific shape vs. the contact radius (Figure 2-11).

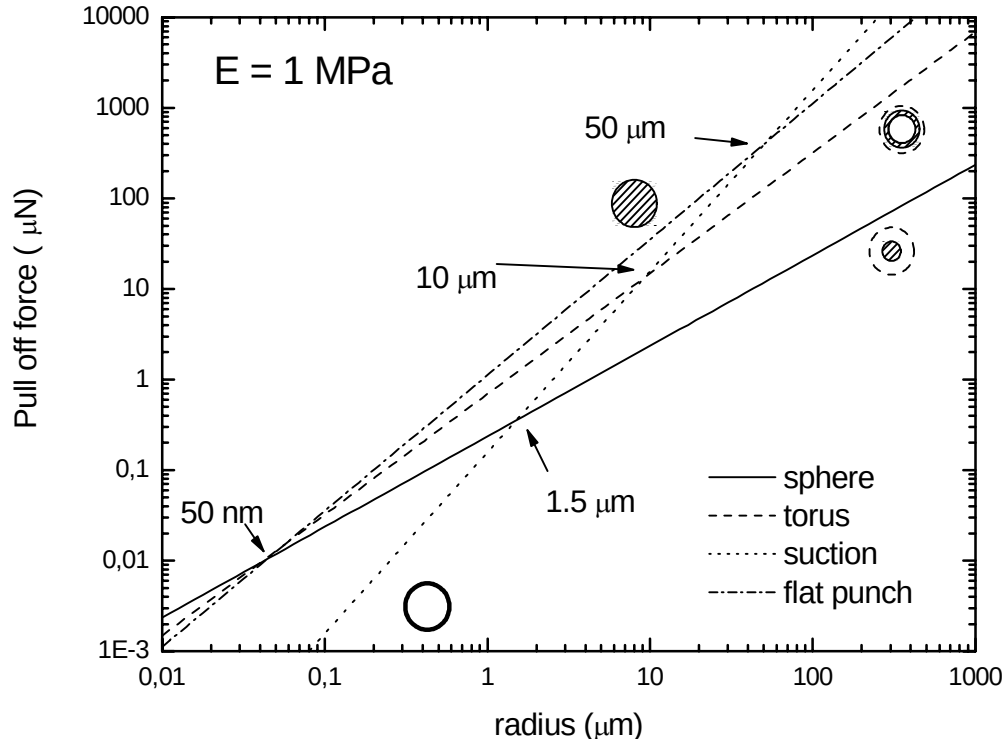

Figure 2-11: Theoretical scaling curve for pull-off forces vs. contact element radius in single contacts (from Spolenak *et al.* [5])

The scaling curves are straight lines of different slopes for the various contact shapes. At the radii corresponding to intersecting curves, the contact efficiency of the two corresponding shapes is reversed. The suction cup is the most efficient geometry at large scale, but due to the different slopes, it is not competitive with any other shape when scaling down to approximately 1 μm. Thus adequate choice of shape and size provides control of the attachment forces. Using a generalized form of equation (2-18) the scaling potential of a specific shape is expressed by an exponent *r*:

$$P'_c = n^r P_c \qquad (2\text{-}22)$$

Thus the total pull-off force is increased by a factor n^r.

Values for *r* are summarized in Table 2-2:

Table 2-2: Functional dependencies of selected contact shapes (adapted from [7])

	Hemisphere	**Torus**	**Flat punch**	**Suction cup**
r	**1/2**	**1/3**	**1/4**	**0**

In particular the adhesion of a flat punch is calculated as:

$$F_c = -\sqrt{8E^* R^3 \gamma \pi} \qquad (2\text{-}23)$$

2.2.4 Hair-like Structures

Roughness decreases adhesion as described by Tabor *et al.* [18]. Fibrillar attachment pads improve the adaptation to rough counter surfaces by stiffness reduction as published by Persson [46]. Hairy structures mainly loaded in bending show less resistance to deformation than under compression [3, 46]. This reduces the stored elastic energy competing with the surface energy. Refined contact elements also improve adhesion on rough surfaces by positioning the terminal elements within the range of attractive surface forces. Peressadko *et al.* [47, 48] have modelled the influence of the terminal element size on the adhesion and friction behavior on rough surfaces. For a set terminal element size, adhesion is at a minimum for a specific roughness. The geometry for contact matches better for bigger surface asperities with a greater radius of curvature and also for negligible or zero roughness (Figure 2-12). Besides, small roughness may be compensated by the deformation of the terminal pad as modelled by Persson [49]. As the influence of roughness was not investigated in the present work, this model is not discussed in detail.

Figure 2-12: Flat element contacting various asperity sizes a) zero roughness, b) intermediate c) waviness

Minimizing the contact diameter for better roughness adaptation is limited by other issues. As in the *JKR-DMT* transition (2-14), decreasing the contact size changes the loading state continuously from Griffith crack-like behavior with stress singularities at the contact edge to homogeneous stress distribution [4, 30, 50]. When the tip radius is reduced below R_c, the contact strength of a frictionless flat punch converges to the theoretical contact strength σ_{th} [30]:

$$R_c = \frac{8E^*\gamma}{\pi\sigma_{th}^2} \qquad (2\text{-}24),$$

and further size reduction does not improve adhesion. Seemingly this condition is followed by the design of biological attachment devices as in geckoes and many insects. By assuming realistic values like 2 GPa for the stiffness, 50 mJ/m² and a theoretical strength of about 100 MPa, a radius of about 100 nm is obtained. The critical radius is similar but not identical to the critical radius given for spherical tips by Spolenak *et al.* [7] :

$$R_c = \frac{8E^{*2}b^3}{3\pi^2\gamma^2} \approx \frac{8E^{*2}b}{3\pi^2\sigma_{th}^2} \qquad (2\text{-}25),$$

where b is the interatomic equilibrium distance and the theoretical strength σ_{th} may be approximated by γ/b [7].

The minimization of contact radius is also limited by the mechanical stability of the fibrillar structures [7]. If poorly designed, the fibers condense to clusters, buckle or bend under their own weight, leading to structures useless for adhesion.
Several authors have pointed out the benefit of using long hair like contact elements for enhancing adhesion. Persson stated qualitatively that long bonding elements improve

adhesion as they elastically bridge long distances *b* between the adhering counter surfaces. In this approach the effective work of adhesion equals the energy stored elastically in *n* long curved fibers with a spring constant *k* over a bridging length *b* of a unit area before the critical detachment force is reached [46]:

$$\gamma_{eff} = \frac{nkb^2}{2} \qquad (2\text{-}26).$$

The equation for γ_{eff} only holds if the work of adhesion can be neglected compared to the high value of the stored elastic energy which has to be dissipated completely during detachment. Persson gives a first remark about the role of dissipation processes for enhanced work of adhesion, a point treated in more detail by calculations of Hui *et al.* [4] and experiments by Ghatak *et al.* [51]. Long hairy contacts improve adhesion by dissipation and crack arresting. In a fibrillar contact each fibril stores deformation energy according to [4]. Analogously to the effect described by Lake and Thomas [52], the energy is fully dissipated during detachment and not redistributed to the crack front as in continuous media. Therefore the energy E_{detach} for detaching a fibril stiffer than the counter substrate consists of the work of adhesion (first term) and the stored elastic energy (second term):

$$E_{\det ach} = \left(\frac{\sigma_0^2 \, h}{2E_{Fiber}} + \gamma \right) \pi a^2 \qquad (2\text{-}27) \, .$$

where σ_0 is the interfacial strength, h the length of the fiber, E_{Fiber} the Young's modulus and a the contact radius of the flat tip. For an elastic fiber on a rigid substrate the equation is somewhat altered but follows the same principle.
The detachment energy is increased compared with a crack in a continuous material, as the periodic structures arrest the crack front [4, 51, 53]. When the contacts break successively as in a crack, contact strength and toughness both increase compared to a opening crack in a non -fibrillar interface as the load for peeling is directly proportional to the work of adhesion [54].

2.2.5 Hierarchy

Although biological attachment systems are generally hierarchical, the underlying design principle of hierarchy has not been thoroughly studied. Obviously the splitting of a coarse hair

into finer sub features allows contact adaptation on different roughness scales. Still the optimal size relations between single levels of hierarchy are not obvious. It was proposed to switch to a new level whenever the respective structures reach a critical length for condensation [3]. This aspect is enforced by calculations applying the non-condensation criterion to the gecko attachment system. Hierarchy also provides a means of switching the loading conditions for the contacting fibrils by asymmetric design [50]. Thus attaching and detaching are performed at a different loading angle by the seta geometry.
For adhesion enhancement, hierarchy could also play a role in providing a homogeneous load distribution. A fibrillar attachment pad detaches, similarly to a single contact, either homogeneously stressed or in a crack-like configuration. The probability for initiating a crack due to imperfections grows with the size of the fiber support. By adequately dimensioning the fiber support, homogeneous loading of the fibrils may be achieved.

2.2.6 Design Guidelines for Arrays of Biomimetic Contact Elements

As copying biology in a trial an error process is very time consuming and not necessarily yields the optimal solution, it is recommendable to define road maps based on scientific knowledge about the working principles and limitations. Spolenak *et al.* [7] visualized design guide lines for fibrillar biomimetic adhesives in design maps in the style of Frost and Ashby's deformation mechanism maps [55]. By plotting the Young's modulus of the material vs. the single contact radius for preset values of further parameters, such as the work of adhesion γ, the interatomic equilibrium distance b and the areal density of fibers f, a design map for fibrillar attachment devices is generated. Plotting the limiting functions for required properties of a working attachment device encircle a property range for optimal dry adhesives. The region of interest within such a chart lies in a triangle limited by the criteria for condensation, apparent contact strengt (tenacity), and adaptability of the fibers with an aspect ratio λ (Figure 2-13).

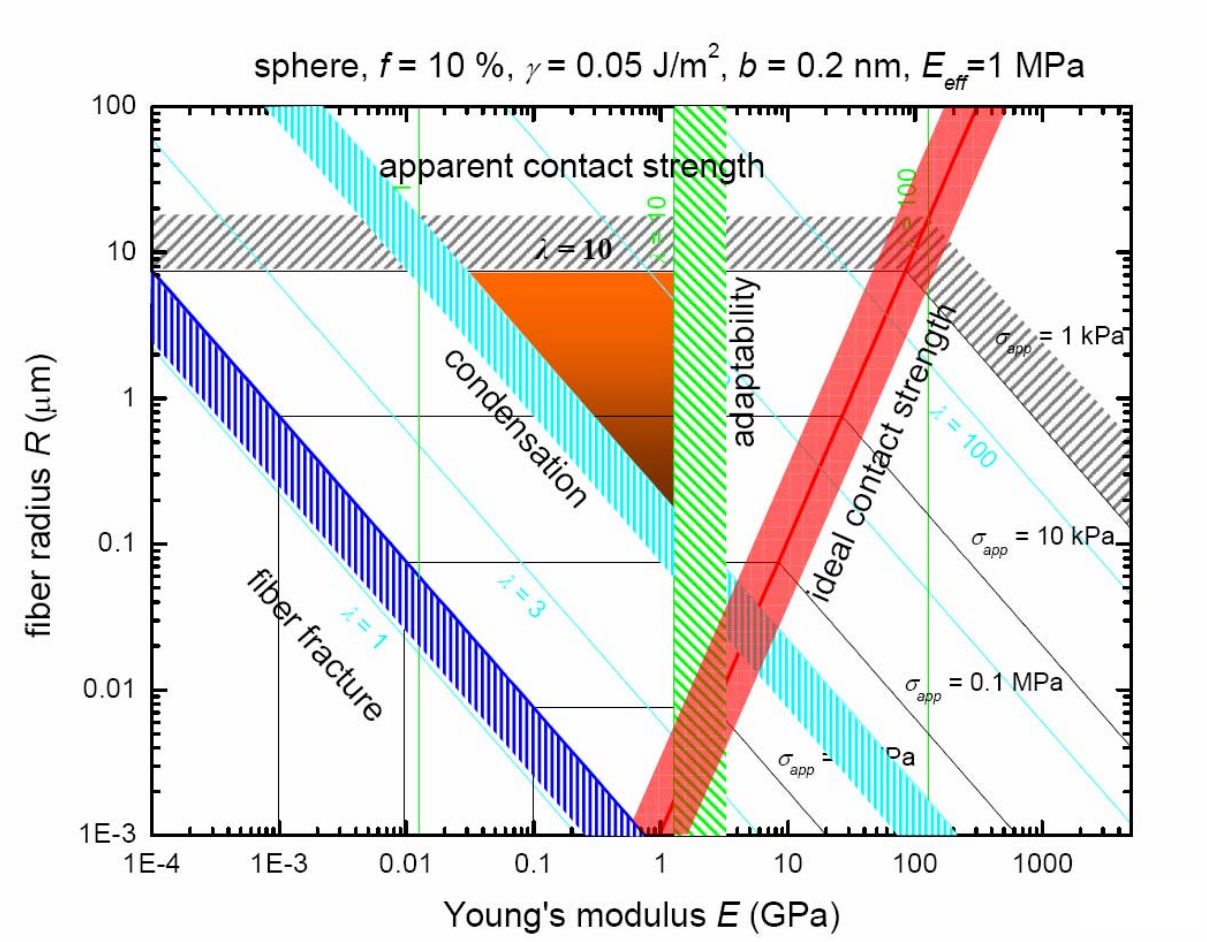

Figure 2-13: Adhesion Design Map [7] showing Fiber radius vs. Young's modulus: Optimal conditions within the filled triangle spanned by the limits for an apparent contact strength of 1 kPa, an adaptability E_{eff} of about 1 MPa and a condensation criterion determined by an aspect ratio of 10

The ideal contact strength limits the triangle of interest towards high moduli and small fiber radii respectively by a linear function with a slope of 2 as in Figure 2-13 on the right side. The contact strength of a single spherical contact element does not increase continuously with reduced radius but reaches the theoretical contact strength. The contact area can never support higher interfacial stresses than given by the theoretical strength σ_{th} resulting from the intermolecular interactions. It should be remembered that reducing the radius or increasing stiffness corresponds to a shifting from *JKR* to *DMT* (2-14). For visualization the Tabor parameter μ is applied:

$$\mu = \frac{R^{\frac{1}{3}} \gamma^{\frac{2}{3}}}{E^{*\frac{2}{3}} \varepsilon} \qquad (2\text{-}28)$$

JKR theory is valid for μ>3. Setting μ to 3 and resolving (2-27) . by *R* yields the *JKR-DMT* transition curve for the adhesion design map:

$$R = \frac{\mu^3 E^{*2} \varepsilon^3}{\gamma^2} \qquad (2\text{-}29).$$

The *JKR-DMT* transition coincides with the limit for optimal contact strength for a Tabor parameter of 0.7. Hence, the critical radius is generally coupled to the transition between crack-like and homogeneous loading of the contact interface.

Expectedly the transition line runs parallel to the ideal contact strength criterion.
In the depicted case, the transition to *DMT*- theory is more restrictive than the ideal contact strength criterion. When crossing the transition line, the boundary conditions for *JKR* are no longer valid and *DMT* should be applied. As the pull-off forces for both models do not depend on the Young's modulus and scale linearly with the radius of curvature, the design maps are still valid, but the adhesion pressures are higher by one third.
As a further limit, the apparent contact strength defines the force needed to detach a specific area of the adhesive. Within the ideal limits the apparent contact strength for an adhesive with areal fiber density *f* is [7]:

$$\sigma_{app} = \frac{3f\gamma}{2R} \qquad (2\text{-}30)$$

and limits the optimization region as an upper horizontal limit for the fiber radius.

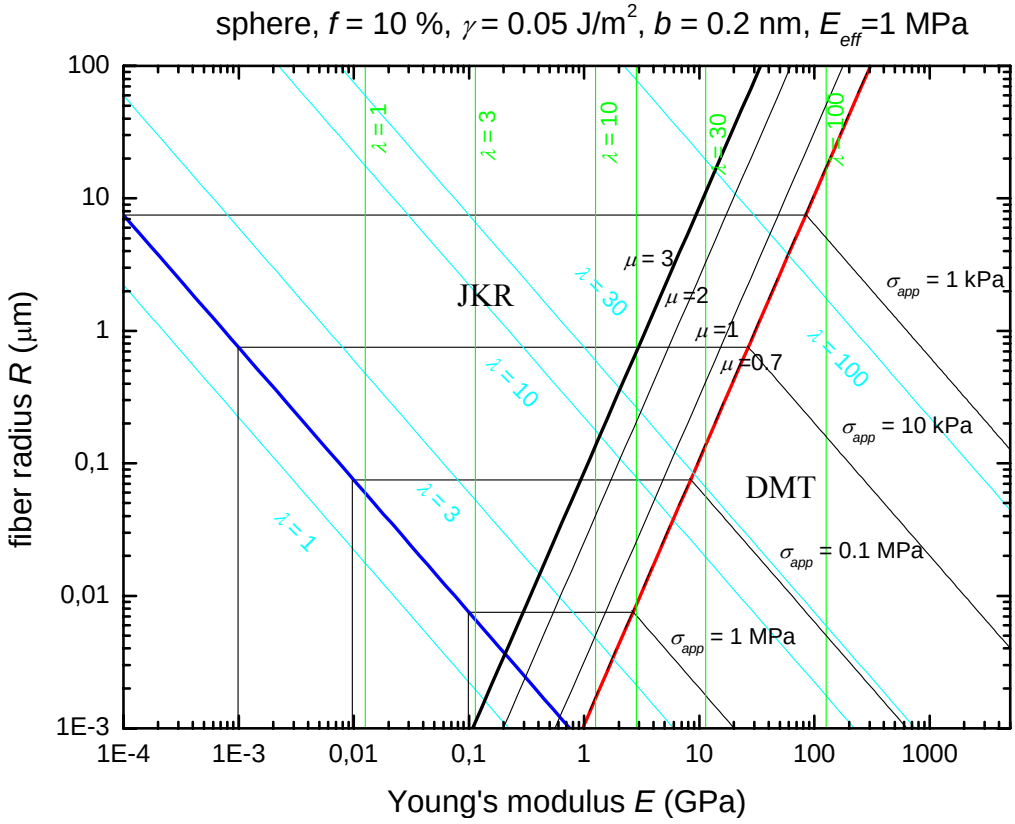

Figure 2-14: Adhesion Design Map [7] replotted with *JKR-DMT* transition limits for different μ = 0.7, 1, 2, 3. The line for μ=0.7 coincides with the limit for optimal contact displayed in the original diagram

Outside the ideal contact strength limit, this criterion is altered to

$$\sigma_{app} = \frac{3f\gamma^{\frac{5}{3}}}{4bE^{\frac{2}{3}}R^{\frac{2}{3}}}\left[9\pi(1-\nu^2)\right]^{\frac{2}{3}} \quad (2\text{-}31),$$

where b is the characteristic length of surface interaction typically in the range of Angstroms [7]. Lines of constant apparent adhesion strength run at a slope of -1 outside the optimal regime.

As a third limit the aspect ratio of the fibers is limited by the condensation tendency of slender fibrils. Neighboring fibers stick to each other when the adhesion force between them exceeds the elastic restoring forces for the bent fibers. Fiber arrays are insensitive to condensation when

$$R \geq \frac{8\gamma'\sqrt{h(f)}}{E}\lambda^3 \qquad \text{(2-32).}$$

with

$$\frac{1}{h(f)} = \left(\sqrt{\frac{\pi}{4f}} - 1\right)^2 \qquad \text{(2-33) [7].}$$

where γ' is the work of adhesion between the fibers with an aspect ratio λ [7]. This criterion limits the region of optimized adhesives with a lower boundary for the modulus as well as for the fiber radius at a slope of -1. All three criteria define the triangle for optimal fiber array design assuming spherical tips. For other tip geometries the theory has to be adequately altered.

The diagram displays two further criteria, the fiber fracture limit and the predefined system adaptability (stiffness). Fiber fracture occurs when the contact strength exceeds the theoretical strength of the fiber material σ_{th}^{f}. For metals the theoretical strength is about 1/10 of the Young's modulus. Then the fracture criterion yields:

$$R > \frac{3\gamma}{2\sigma_{th}^{f}} \qquad \text{(2-34).}$$

The fracture line runs parallel to the condensation limit at a slope of -1 and commonly is less restrictive than the fiber condensation limit. Therefore the latter is more relevant for giving a minimal radius respectively for the Young's modulus of the fiber.
The adaptability limit is given by more technical than physical requirements. In the given diagram, the adaptability function is more restrictive than the ideal contact strength. Adaptability plays an important role for making contact with rough surfaces, as a conform contact has to be formed with the counter surface by deformation of the adhesive pad. A model to evaluate the stiffness E_{eff} of a fiber array under bending load has been introduced by Persson [46]:

$$E < E_{eff}\frac{4\pi}{Cf}\lambda^2 \qquad \text{(2-35).}$$

where *C* is a geometrical factor of about 10. The adaptability is visualized as a vertical line in the fiber radius vs. Young's modulus, limiting the maximum elastic modulus of the fibers. The adaptability limit should not be confused with the limiting stiffness for pressure sensitive adhesives given by Dahlquist [56]. In both cases the adhesion performance is limited by the stiffness of the adherent, nevertheless the mechanisms are different. The Dahlquist criterion yields a limit for spontaneous fibrillation of a soft flat adhesive under tensile loads [57], whereas the adaptability considers the deformation of a fibrillar layer to match the topography of the counter surface as modeled by Persson [46].

The adhesion design maps display the limits of an optimized system for a fixed set of parameters like fiber areal density, effective stiffness, work of adhesion and distance of surface interactions. Variation of these parameters shifts the optimal region within the diagram. It is recommendable to use tabulated values for the theoretical strength of polymers, as in contrast to metals, no simple model for the strength of polymers is available.

Although all described efforts tend to maximize adhesion forces, technological needs may be different. In micromanipulation the forces required for "pick and place" manipulation of parts do not necessarily coincide with the maximum adhesion force. Spolenak *et al.* [5] provide a guideline for controlling adhesion forces in a wide range by adequately dimensioning and designing the single contacts in biomimetic adhesive.

2.3 Measuring Adhesion with Cantilever Instruments and *AFM*

Atomic Force Microscopy combines a powerful metrology tool with a technique for force measurements down to the pico-Newton scale. Despite a variety of setups, the main principle of a tip on a cantilever scanning the surface of an object is universal. By detecting the cantilever deflection, the interacting forces are calculated according to

$$P = k\delta \qquad (2\text{-}36)$$

where *k* is the spring constant of the calibrated cantilever and δ the deflection. Force resolution is determined by the stiffness of the cantilever, but the stiffness cannot be decreased arbitrarily. With reducing the cantilever stiffness system instabilities (snap in and

out) play a more and more important role. Instabilities occur when the spring constant of the cantilever drops below the gradient of the external forces acting on the cantilever [58, 59]:

$$k \leq \frac{dP}{dx} \qquad (2\text{-}37)$$

Using high stiffness cantilevers reduces the problem of instability jumps but also decreases force resolution. Finding the right cantilever for the respective application is an optimization problem. For commercial systems, cantilevers in a wide range of stiffness are available.

In modern instruments the deflection is measured by a laser beam reflected from the cantilever onto a quadrant photo- detector (Figure 2-15).

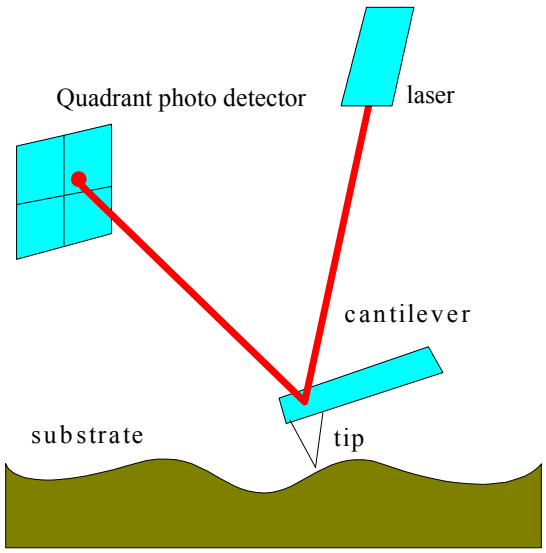

Figure 2-15: *AFM* setup with a quadrant photo detector (schematic)

Vertical forces (*AFM* signal) are determined by the intensity difference between the two upper and lower photo detectors whereas lateral forces (*FFM* signal) is determined by subtracting the right side and left side intensities. Commonly the cantilever bears a needle- like tip, but also custom geometries (e.g. tipless) are in use. In contrast to the surface force apparatus (*SFA)*, the tip-surface distance is not directly accessible.

2.4 Fabrication of Bio-inspired Attachment Specimens

Simply copying biological attachment devices neither is feasible due to their complexity, nor may it be very beneficial for adhesion. Before selecting an appropriate micro structuring method, the purpose and the required properties should be thoroughly analyzed. Defining the design also yields the adequate set of fabrication methods. Several groups fabricated arrays of micro-molded or *RIE*-etched flat ended pillars or cuboids. These techniques will be referred to in the following chapters.

2.4.1 Photolithography

Photolithography is a tool long established for micro fabrication. Structures are generated on a substrate by depositing a photo sensitive resist film (Figure 2-16 a, b) and exposing it through a mask (Figure 2-16c).

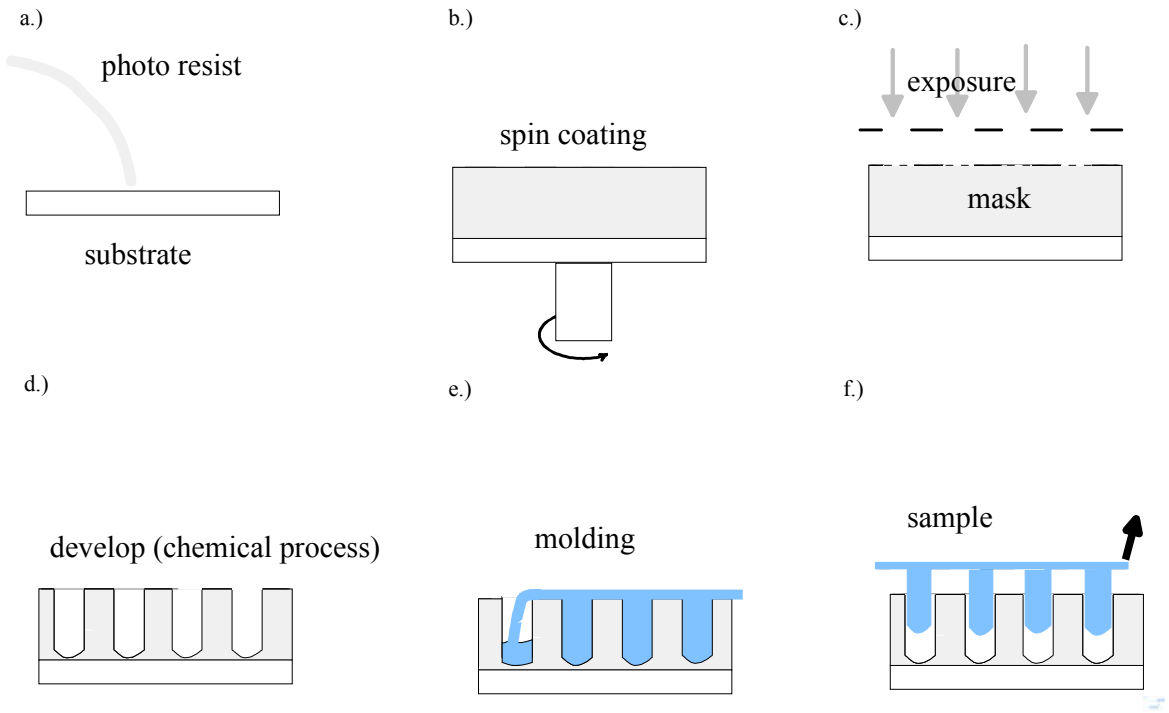

Figure 2-16: Photolithography and molding: a) photo resist deposition, b) spin coating, c) exposure through precision mask, d) developing, e) polymer molding, f) specimen removal

In a subsequent development process the exposed material is dissolved, whereas the non-exposed areas remain, or vice versa, depending on the resist type (Figure 2-16d). The structures either are used directly or provide templates for micromolding. For molding, the

templates are filled with a polymer (Figure 2-16e) that is ejected after hardening (Figure 2-16f).
Glassmaker *et al.* [3] applied photolithography for fabricating several 5x5 mm² fields containing rectangular lamellae 5, 10, 20 and wide 50 µm and 19 times as long. The spacings correspond to the particular structure width. The features were 30 µm high, as determined by the resist thickness.

2.4.2 RIE Techniques

Geim *et al.* [60] produced hair like structures by a dry etching process. After spinning a polyimide film onto a substrate, the surface is coated with a photoresist and structured by e-beam lithography. In a further step a thin aluminium layer is deposited onto the coating. During lift-off the metalized resist structures are stripped off and only the metal features directly attached to the base remain. These form the dry etching mask. The oxygen-plasma etching outside the metal disks proceeds faster than for the polymer covered by the disks. The process is stopped after complete removal of the aluminium.
The etching rate difference results in a pillar structure on the surface. Thus 2 µm high structures, 1 µm in diameter were fabricated.
Deep *RIE* was also used for structuring templates for micromolding [3]. After patterning 4-inch Silicon wafers with deep ultraviolet photolithography (*DUV*), 10 µm deep and 1 µm wide cylindrical channels were etched into the substrate by *DRIE*.

2.4.3 Laser Cut Templates for Micro Molding

Micro-molds of larger diameters were fabricated by micro molding laser cut metal templates [47]. The experiments yielded elliptic pillars (100x 200 µm). Such structures offer access to mechanistic studies as the adhesion to a glass plate can be documented using a video camera.

2.4.4 Imprinting Techniques

In micro- imprinting, patterns are commonly generated by pressing a rigid stamp into a polymer substrate heated beyond the glass transition temperature (hot embossing). Before retracting the stamp, the substrate is cooled down in order to conserve the structures yielded in the polymer. Similar shapes can also be achieved by plastic deformation without heating

[61]. The tip penetrates the surface at the wished locations to a specified depth and after retraction the mold remains in the plastically deformed surface (Figure 2-17).

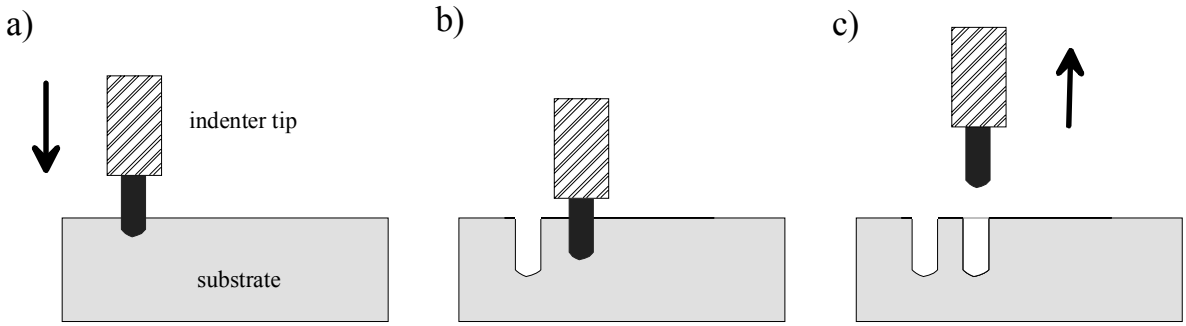

Figure 2-17: Fabrication of micro molds by cold imprinting: a) first imprint, b) second imprint, c) tip retraction after imprinting

For a spherical indenter tip the imprints have hemispherical geometry although the dimensions are different from the original indenter tip [62] due to elastic relaxation. Thus spherical indents possess a radius slightly larger than that of the indenting sphere and conical indents have a slightly enlarged included tip angle. When the pits and the molded specimens are well characterized using white light profilometry, this is not an issue for contact experiments and deviations from the indenter tip are tolerable, as long as the geometries are well known. This reduces production time compared with *FIB* structuring, provided that appropriate indenter tips are available.

Sitti *et al.* [61] proposed the micromolding of *AFM* tip imprints in a wax surface. The casts were done in silicone rubber (Dow Corning Inc., HS II) and polyester resin (TAP Plastics Inc.). The structures were characterized by *AFM* and are about 2 µm wide and 1 to 2 µm high. Therefore they lack the high aspect ratios typical for biological structures.

2.4.5 Incision of Polymer Films

For mechanistic studies Ghatak *et al.* generated *PDMS* films and incised it with a sharp razor blade [51]. Thus arrays of 30, 50,100 and 200 µm squares and bars, 40 to 1000 µm high were obtained.

2.4.6 LIGA Based Specimen Fabrication (Singapore Synchrotron Light source)

The *LIGA* microstructuring technique (an acronyme for the German words of the main processing steps: Lithography, electroforming and casting), developed by the Forschungszentrum Karlsruhe in the early eighties, is well suitable for mass fabrication of straight walled high-aspect-ratio pillar structures [63]. In contrast to classical optical photolithography, deep X-Ray lithography applies sharply collimated and brilliant X-ray illumination. Thus structures up to 1 mm high with a lateral resolution of 0.2 µm for arbitrary lateral geometries can be fabricated. In *LIGA* a subsequent electroplating process with metals such as gold, copper, gold or nickel yields robust negative metal structures either for direct use or as molds for plastic micromolding. For the present work only the first step of deep X-ray lithography was applied.

2.4.7 Bioinspired Attachment Specimens with Multi-walled Carbon Nanotubes (MWNT)

Recently Yurdumakan *et al.* [64] fabricated hairlike attachment structures based on multi-walled carbon nanotubes. The fibers were grown by self-assembly on quartz or silicone substrates and embedded into a *PMMA* matrix. By removing the composite material from the substrate and dissolving the matrix surface partly with acetone or toluene, an array of *MWNT* fibers backed by a *PMMA* film were set free. The adhesion properties were measured via *AFM*.

2.4.8 Hierarchical Bioinspired Specimens

Recently Northen *et al.* [65] demonstrated the fabrication of hierarchical bioinspired attachment devices. First free standing silicon pillars where fabricated, 1 µm wide and up to 50 µm high, supporting rectangular platforms about 100x 100 µm². The etching was done by DRIE and a subsequent isotropic SF_6 etching step generated the slender support pillars. Then the photoresist mask on the platforms used for the DRIE process was structured by a plasma treatment. The biased plasma provided an electric field gradient that led to the spontaneous formation of hairlike nanorods 200 nm wide and about 2 µm long in a second level of hierarchy.

2.5 Electrochemical Wet Etching for the fabrication of Molding Templates

Steinhart *et al.*[66, 67] demonstrated a method for the fabrication of arrays of polymer micro and nanotubes using electrochemically wet etched self-aligning pores in silicon or alumina as molding templates.

Before etching the silicon, an adequately doped silicon wafer is prestructured by photo lithography and anisotropic etching or a similar technique (Figure 2-18 a). The etch pits act as seeds for the pore etching process. The silicon wafer is immersed in HF in an electric field (Figure 2-18 b). As the HF does not attack electro neutral silicon, electronic holes are introduced into the silicon by backside illumination of the wafer. The electric field controls the charge transport and the shape and size of the space charge region. The electronic holes cumulate at the etch pits and transfer the silicon into a positively charged state, thus etchable by the surrounding acid.

The generated pores can be used as templates for micromolding fibrillar structures (Figure 2-18 c and d).

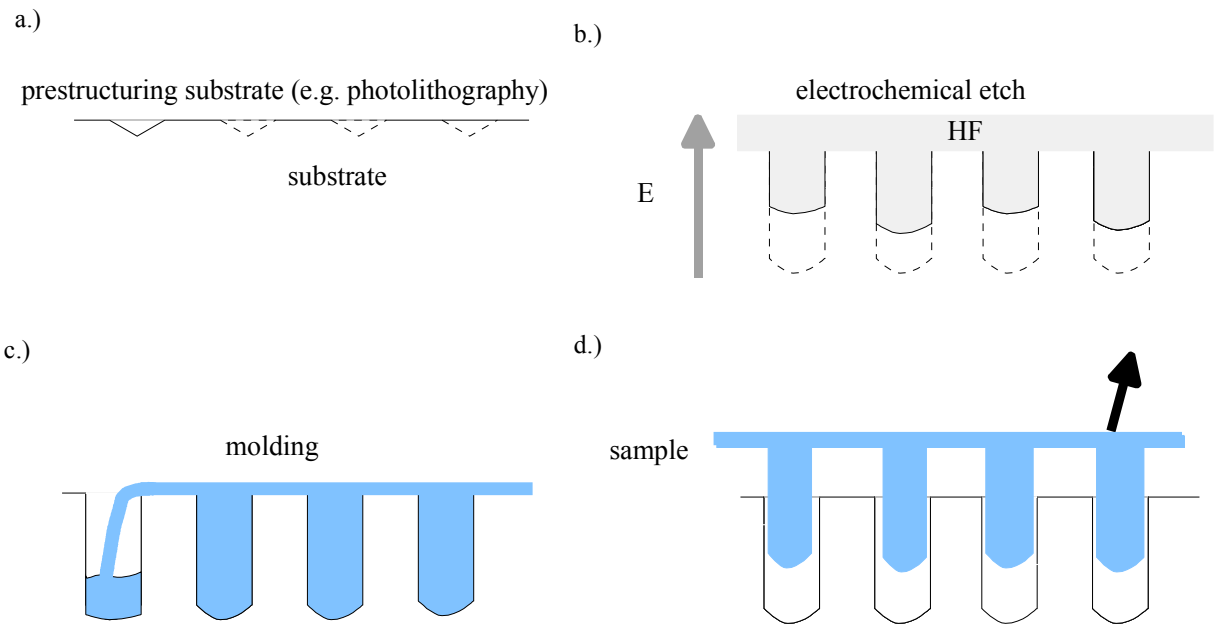

Figure 2-18: Combined *FIB* prestructuring and wet etching process: a) initial trench processing (*FIB*), b) electrochemically enhanced etching in HF, c) molding, d) removal of specimen

The prestrucuring of the initial etch pits commonly performed by photolithography. The electrochemical etching generates the channels for the molding template. In a further step the channels are filled with polymer which is removed after hardening. The electrochemical

etching process allows for varying the channel diameters depending on the etching depth by modifying the etching parameters. Thus highly complex template geometries can be produced (Figure 2-19).

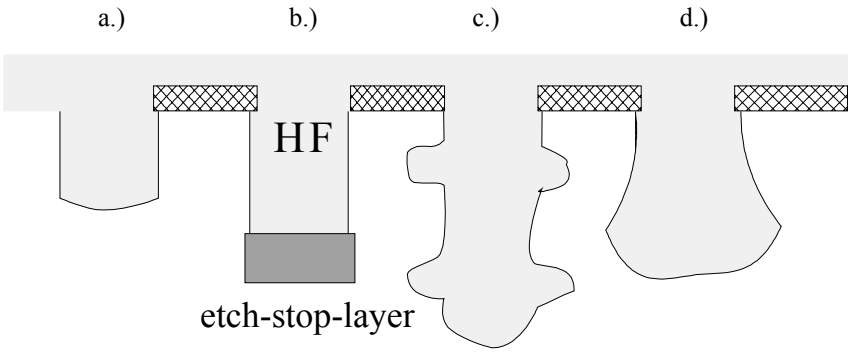

Figure 2-19: Different trench shapes fabricated by electrochemical etching: a) regular, b) etch stop layer controlled, c) varied field over time, d) bottle shaped

2.6 Sample Characterization

As the adhesion properties of microscopic contacts depend strongly on the surface quality and geometry, the specimens for respective adhesion tests have to be thoroughly characterized. This section gives a short overview over the applied microscopy methods.

2.6.1 Light Microscopy

The simplest way of coarsely judging the quality of microstructured samples is to use standard light microscopy. The 2D micrographs show regularity and lateral spacing, the quality of shape contours of single features as well as fiber condensation. Light microscopy is appropriate for characterizing objects in the micrometer regime. For smaller features and topographical information, other imaging techniques (e.g. *AFM*, *SEM*) are more appropriate.

2.6.2 White Light Profilometry

Interference methods are widely used for measuring surface topography. The classical method generates an interference fringe pattern on a surface by illuminating it with interfering beams and evaluating the shape and the distance between the fringes. More accurate information is

gained from phase shifting interferometry [68]. During a measurement, the phase of the interfering beams is shifted continuously while determining the intensity data for four supporting points spaced by a phase difference of $\pi/2$. Successively the phase for each pixel and as a result the vertical distance between adjacent pixels is determined. For monochromatic illumination, the periodicity in intensity leads to ambiguous height information if the difference between two adjacent pixels exceeds a quarter of the used wavelength. The dynamic range of this method can be increased by using at least two different wave lengths for the interfering beams. Modern digital optical profilers prevent height ambiguities by vertical scanning coherence peak sensing, where the light intensity is tracked over the vertical coordinate during a z-scan. The broad wavelength spectrum of the interfering light beams only generate fringe patterns when the optical paths are identical. By scanning a surface in vertical direction, this white light point is detected for each pixel on the surface and referenced to the surrounding pixels (Figure 2-20).

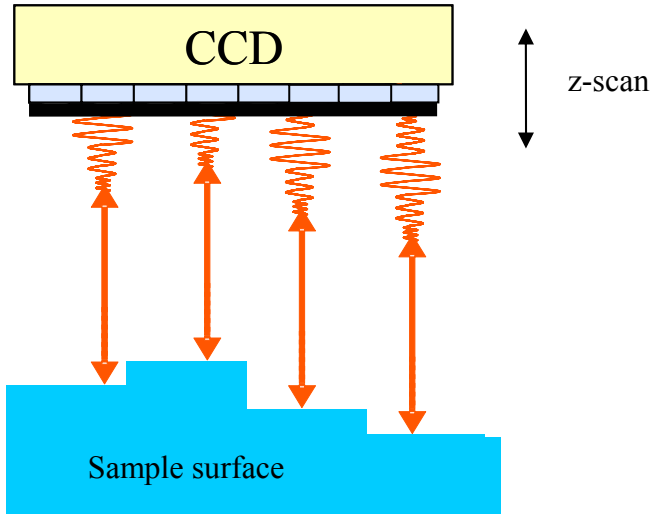

Figure 2-20: Scanning detection of the white light point for every lateral position on the sample surface by a CCD detector for discrete z-positions of the scanning device

As performing a scan for all heights within the measuring range is quite time consuming, modern instruments track the fringe intensity envelope at defined sampling points and find the white light point by demodulating and analyzing the fringe signal envelope, using classical signal processing theory [69]. A comprehensive overview for optical metrology is given by Bhushan [70].

Measurements yield step information in the mm range as well as roughness on the sub-nanometer scale. Problems occur when the measurements are performed on translucent thin

films or multi material samples with different optical properties. In our case the samples generally consist of one material and are thick enough to avoid disturbing back side reflections. The lateral resolution of optical profilometers is generally in the range of 1 micrometer. Sample characterization was performed on a commercial NewView 5000 (Zygo Corporation).

2.6.3 Scanning Electron Microscopy (SEM) and Focused Ion Beam (FIB) Imaging

SEM is a standard method for imaging micro- and nano- scale objects. An electron beam is scanned over the examined surface and the emitted secondary electrons are detected for imaging. *SEM* generally works well on electrically conductive surfaces. On insulators the scan leads to a charging of the surface resulting in a deflection of the beam and sometimes in displacements of the sample by electrostatic forces. By depositing carbon or gold, surface charging is generally reduced. For adhesion samples it is necessary to conserve the generic surface properties for subsequent adhesion measurements. Thus the samples either have to be divided into a test specimen and a reference sample for *SEM* characterization, or the imaging has to take place on a non-coated sample. With the LEO 1530 VP, micrographs on insulator material are obtained by working at an acceleration voltage of around 1 kV in the in-lens-imaging mode. In this mode the detector lies in the e-beam axis and provides a good topography contrast. A spatial view is achieved by tilting the sample.
Focused ion beam (*FIB*) imaging resembles the *SEM* technique, using ions instead of electrons for scanning the surface. Some of the Ga+ - ions are implanted into the surface and improve the surface electronic conductivity. The impact of the Ga+-ions damages the surface by sputtering and also changes the surface properties by implantation. Therefore it is not adequate for characterizing samples intended for adhesion measurements.

Focused ion beam microscopes are indispensable tools for micro technology. *FIB* combines electron imaging and micromachining of surfaces at the micron and sub-micrometer scale. The *FIB* consists of an evacuated beam column connected with the sample chamber (Figure 2-21). A high voltage electric field extracts Ga^{+}-Ions from a Gallium reservoir and accelerates them towards the sample. The beam is focused and directed by a set of apertures and electronic lenses.

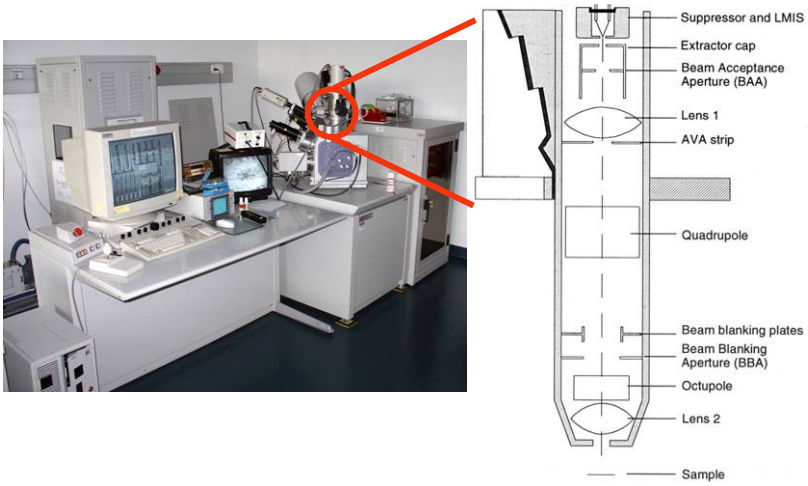

Figure 2-21: Focused Ion Beam *FIB* FEI 200 (image S.Orso)

As the ions collide with the sample surface they emit substrate atoms and secondary electrons. The latter are used for imaging as in common *SEM* technology (Figure 2-22 left). Milling is mainly used for cutting cross sections (Figure 2-22 center). A trench of uniform depth is cut into the surface, and the side wall is imaged after tilting the sample. For some cases the milling process is enhanced by injecting reactive gases that are locally activated by the ion-beam. The *FIB* also is suitable for depositing tungsten or other metals by decomposition of injected gaseous percursor molecules on the sample surface (Figure 2-22 right). This feature is helpful for masking and bonding.

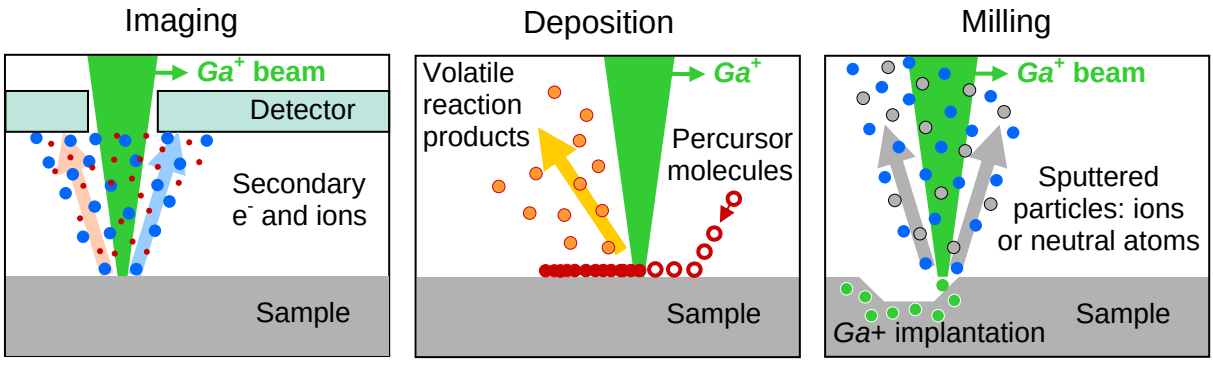

Figure 2-22: *FIB* working modes imaging (left), deposition (center) and milling (right); (drawing U.Wegst)

2.6.4 Atomic Force Microscopy (AFM)

Profile information for structures in the sub-micron range is inaccessible to white light profilometry. Profile data is alternatively gathered by *AFM* imaging. The working principle of an *AFM* was described in section 2.3.

The surface topography of soft samples is measured in tapping mode. The cantilever vibrates at its resonant frequency at an amplitude preventing surface-tip stiction during the surface scan. The z-piezo adjusts the cantilever height in order to keep the average forces constant. The surface profile is tracked by the piezo displacement. The data gathered is used for the visualization of the three-dimensional scanned surface.

2.7 Conclusions for the Present Work and Perspectives for Bioinspired Adhesives

The cited work mainly concentrated on producing straight hair-like structures with undefined tips (Table 2-3).

Table 2-3: Overview over biomimetic attachment structures

	Gorb, Peressadko [47]	Glassmaker *et al.* [3]		Geim *et al.* [60]	Sitti *et al.* [61]	Ghatak *et al.* [51]
Method	micro-molding, laser cut	micromolding, photolithography		E-beam lithography, *RIE*	micro-molding, Imprint	razor blade
Material	*PVS* [MPa]	*PDMS* [MPa], Polyimide		Polyimide [Gpa]	Polyester resin, silicone rubber	*PDMS*
Shape	Elliptic	circular	rectangular	circular	Sharp	squares
Radius, length a [µm]	50	0,5	5, 10, 20, 50	0,5	1	30,50,100, 200
Radius, length b [µm]	100	“	19 x a	0	“	“
height [µm]	300	10	30	2	2	40-800

The recent approaches to bioinspired attachment devices are promising, but also highlight the problems to fabricate successful products.
None of the methods proposed for the fabrication of biomimetic adhesives is appropriate for mass production. Creating roadmaps for technical adhesives is nevertheless sensible, as the rapid developments in micro technology could provide convenient production methods soon. Already today, bioinspired adhesives may contribute to technical solutions e.g. in the field of micromanipulation as proposed by Rollot *et al.* [17]. Section 2.2 described essential functional features of biological attachment devices. Depending on the purpose, only few of them will have to be realized. High aspect ratios and hierarchy mainly improve the adaptation to multi-scale surfaces roughnesses. For planar and very smooth surfaces e.g. silicon micro parts, wafers, compact discs etc., splitting contacts alone improves adhesion properties [1, 43] neglecting hierarchy and fibrillar design. For other tasks, highly complex devices will be necessary to match the needs.
Neither the geometry of biomimetic contact elements nor the influence of hierarchy has been experimentally addressed. A fabrication technique suitable for defined tip geometries and for hierarchical specimens is proposed in this work. All methods are currently limited to the fabrication of prototypes not exceeding several square centimeters.

Research on bioinspired attachment devices requires adequate sample fabrication and adhesion testing methods. In recent works diverse techniques were applied to generate respective prototypes. So far, no method was proposed for generating specifically shaped contact element tips. Such tips were obtained in the present study by a focus ion beam milling process with subsequent replica molding.
Besides, a technique for precisely controlled adhesion tests on single micro contact elements and arrays on a modified commercial nanoindenter was developed and tested.

3 Development of Methods for Specimen Fabrication and Contact Measurements

3.1 Sample Preparation Using a Focused Ion Beam Microscope (*FIB*)

The micro fabrication techniques presented in section 2.4 neither access control of the contact element geometry nor are they useful for producing hierarchy. It extends the established methods by milling specifically shaped micro molds and by generating hierarchical structures. Although *FIB*-prototyping has not been used for biomimetic attachment devices, several groups have applied this technique for micro structuring [71, 72].

3.1.1 FIB-Prototyping as Basis for the Production of Micro-scale Shapes

The *FIB* method was used to mill micro molds with specific contact element geometries. By scanning a surface, a quantity of material, proportional to the ion dose, is sputtered away. Assigning adequate dwell times to each pixel within the field of view, yielded a predefined depth profile [72]. The principle was successfully applied for generating micro-optical lenses [71] . Such a method for producing well defined molds for micro contact samples was implemented in the present study.

The quantity of removed material is proportional to the current and exposure (dwell) time. A code was implemented in *MATLAB* ™ for computing pattern files for mold fabrication as well as for indenter tips in silicon. For better performance the code was translated to *JAVA* ™ (Appendix B.). The calculations were faster by more than a factor 100 and the software is independent of the computer operating system. The maximum pattern size for the *FIB* pattern generator was not precisely determined, but a pattern of 806500 Pixels was successfully loaded to the pattern generator, whereas a pattern of 1.7 million pixels proved too large for processing. As this pattern was computed in a few minutes, any processable pattern file is calculated within an acceptable time. Thus the masks were directly calculated on the *FIB* controller and then transferred into a silicon surface either for direct use or as molding template (Figure 3-1).

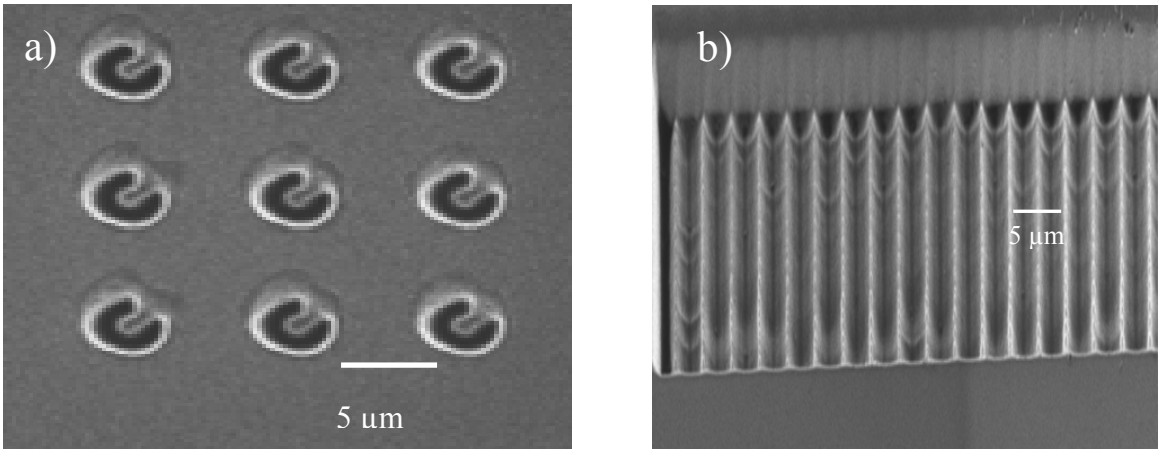

Figure 3-1: *FIB*-milled templates: a) “horse shoes” milled by generating a open ring segment, b) periodic roughness pattern in silicon

3.1.2 Computing Pattern Files (Streams) for FIB- Prototyping

Stream files, which consist of a header and pixel data, provide all instructions necessary for the 3D milling process. The header starts with the letter “s” marking the start of the stream, followed by number of repetitions and the total amount of the pixels. Each pixel is defined by its lateral coordinates (x, y) and the dwell time of the beam. These values are listed in a three column matrix. 4096 by 4096 coordinates may be addressed within the field of view. The software automatically generates pattern files based on given input parameters (Figure 3-2). To generate pattern data for an axially symmetric geometry, the program first determines the structure center point coordinates and then calculates the data for each adjacent pixel in successive annulars starting from the center. The respective dwell times are assigned according to an arbitrary normalized mathematical function *F(r)* that describes the profile as a function of the radial distance to the center point. The dwell time is obtained by multiplying *F(r)* with a given time standard. The patterns are not restricted to axisymmetric shapes. By exchanging the polar with Cartesian coordinates, rectangular layouts may be computed. This extension provides patterns for wedges, rectangular trenches etc. .

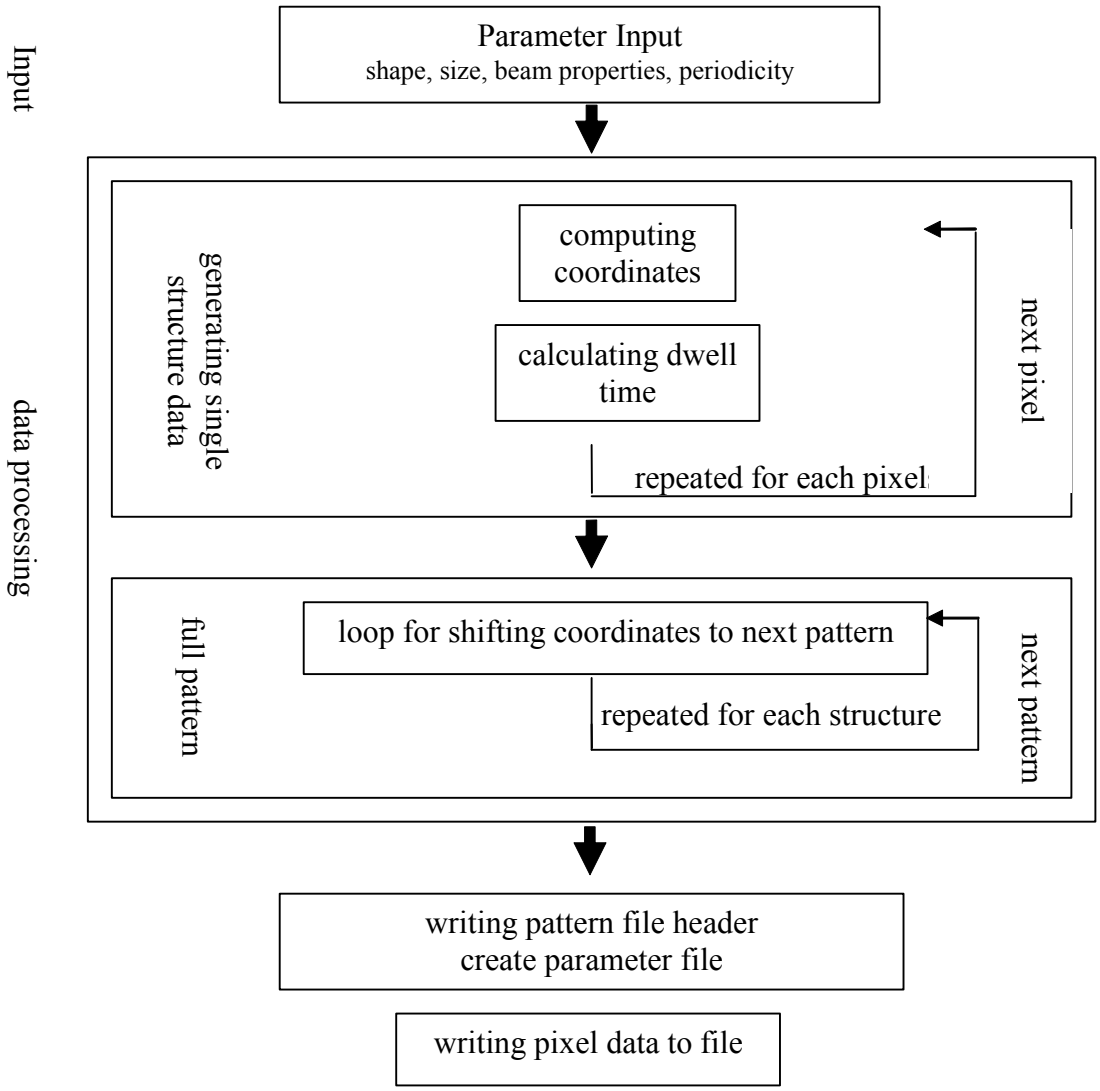

Figure 3-2: Flow chart for the pattern calculation software

The data is stored in a buffer and is periodically written (flushed) to a generated pattern file. At the end of these calculations the software writes the file header including the precise number of pixels. This is important, as the *FEI* 200 *XP* does not read in all data if the specified number is too small and leads to software instabilities if it is too big. After completing the pattern file, the parameters are saved separately.

3.1.3 Generating Axisymmetric Molds and Molded Specimens

The molds were first modelled (Figure 3-3a) and then transferred to the substrate by *FIB* (Figure 3-3 b).

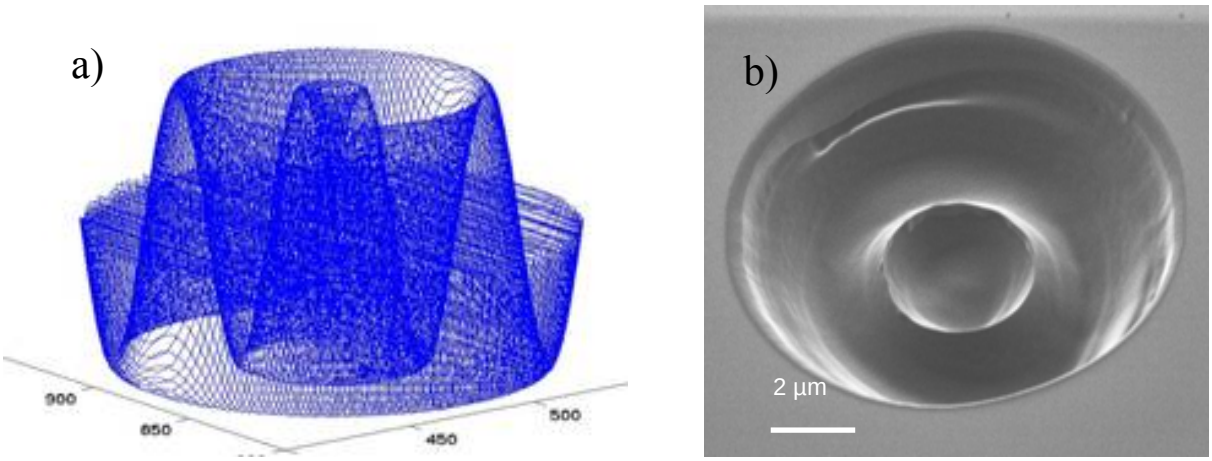

Figure 3-3: a) computed intensity pattern x and y in pixels, b) the resulting milling pattern in silicon

The software also generated periodic patterns of single elements for given lattice parameters. After template preparation the polymer was cast into the molds, hardened and ejected (Figure 3-4). In some cases the stiction of the polymer to the mold was reduced by a silanization to faciliate demolding. We typically applied 1, 1, 2, 2, -Perfluorotrichlorsilane ($C_{10}H_4C_{l3}F_{17}Si$) out of the gas phase in vacuum. Most of our structures were cast in *Sylgard* 184 silicone rubber (Dow Corning), a standard material for micromolding [73]. The prepolymer and the crosslinker were mixed (10:1), applied on the template, degassed in vacuum for 30 minutes and cured in a drying cabinet at 65°C overnight.

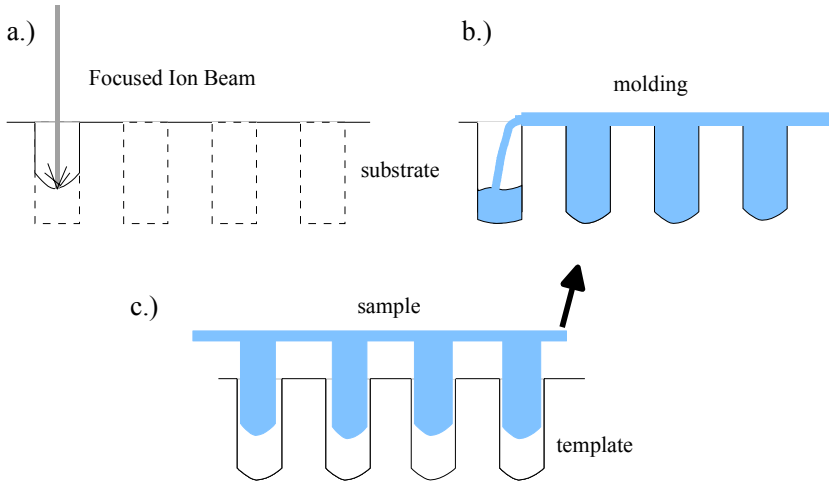

Figure 3-4: *FIB* milling with subsequent molding: a) *FIB* milling, b) molding, c) removal

Due to the great depth of focus, the milling may also be performed on a tilted sample, hence leading to structures inclined to the surface (Figure 3-5). This option was tested for silicon molds in preliminary tests but hitherto not applied for sample fabrication.

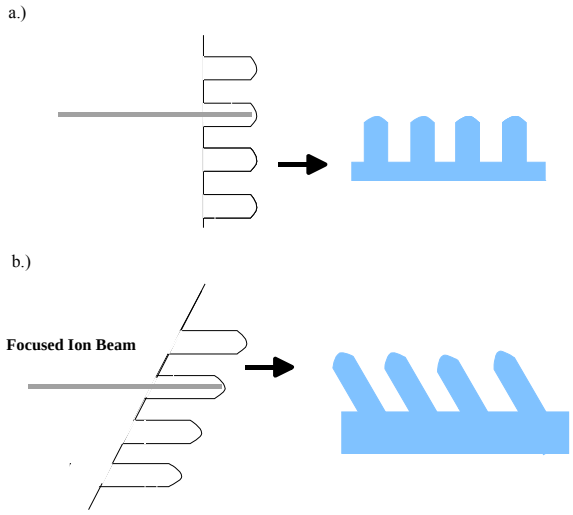

Figure 3-5: *FIB* milling on a perpendicular a) and b) inclined substrate

Periodic structures were either fabricated by moving the stage with subsequent single shape writing (stitching) or by computing an array mask. Writing a complete array in one step requires drift compensation as the beam position is shifted due to surface charges and stage instabilities (Figure 3-6).

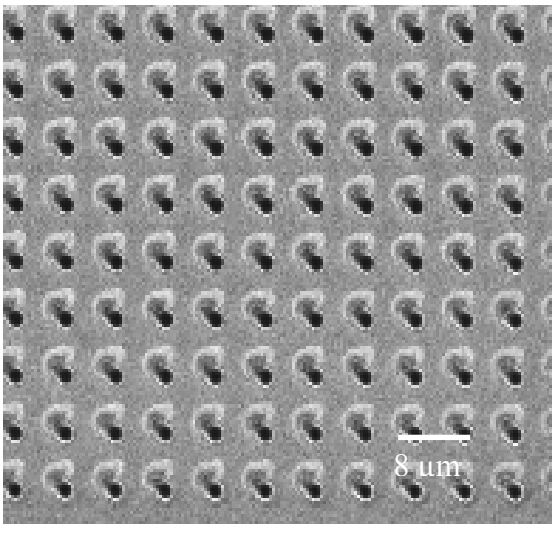

Figure 3-6: Beam drift streaks during 12 hour *FIB* milling process on a silicon surface; the originally round wholes are distorted by beam displacement

Figure 3-6 shows initially round trenches, elliptically distorted due to a beam drift towards the upper left corner. The *FEI* 200 XP offers an automated beam drift correction to avoid such artefacts.

Working in the stage shifting mode reduced the drift problem, as the single structures were written one by one at shorter writing times, compared to milling the whole pattern at once (Figure 3-7). Besides, stitching allowed for patterning areas larger than a single field of view. Thus single structures (Figure 3-7 a) were duplicated as well as whole arrays (Figure 3-7 b)

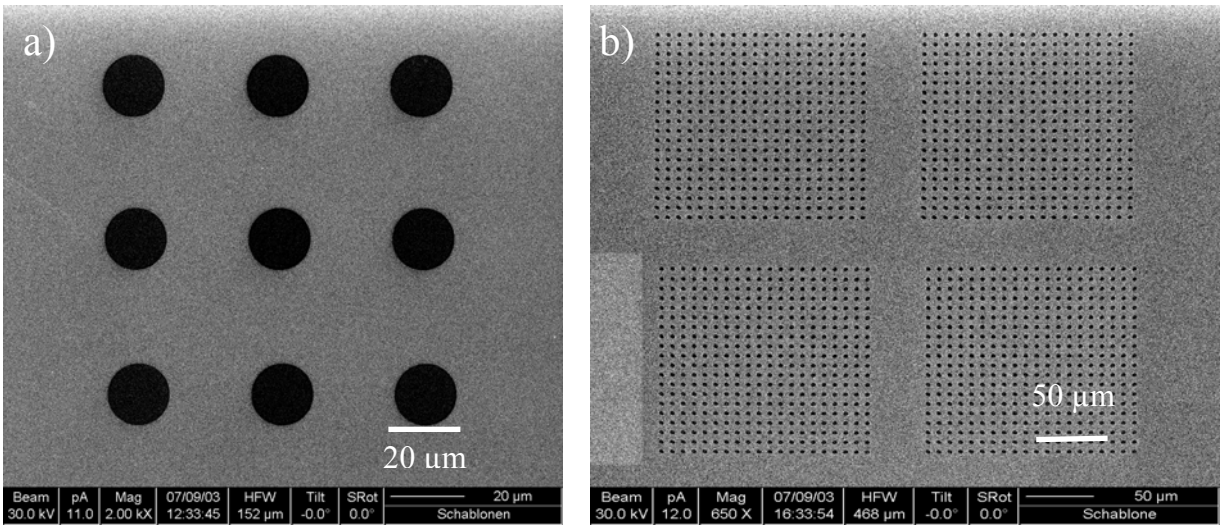

Figure 3-7: Stage shifted structures: a) 9- fold repetition of a single element, b) 4 replicated 20x20 arrays in silicon

In Figure 3-7 a, a single circular pit (r= 10 µm) was milled nine times to generate a regular array at a lattice parameter of 40 µm. In micrograph Figure 3-7 b) four 20 x 20 arrays each 150µm x 150µm wide were generated by stage shifting the single array.

In contrast to static writing, stage shifting reduces the positioning accuracy, as the specified stage precision is limited to 1 µm. The choice of method thus depends on the purpose.

3.1.4 Hierarchical Structures

Furthermore, hierarchical structures were fabricated by *FIB* milling. The *FIB* is capable of first writing an array of coarse elements and then superimposing a second level of finer structures within the border of the first level features. Adequate pattern files were generated for each level (Figure 3-8) and subsequently loaded to the *FIB* pattern generator for stepwise milling.

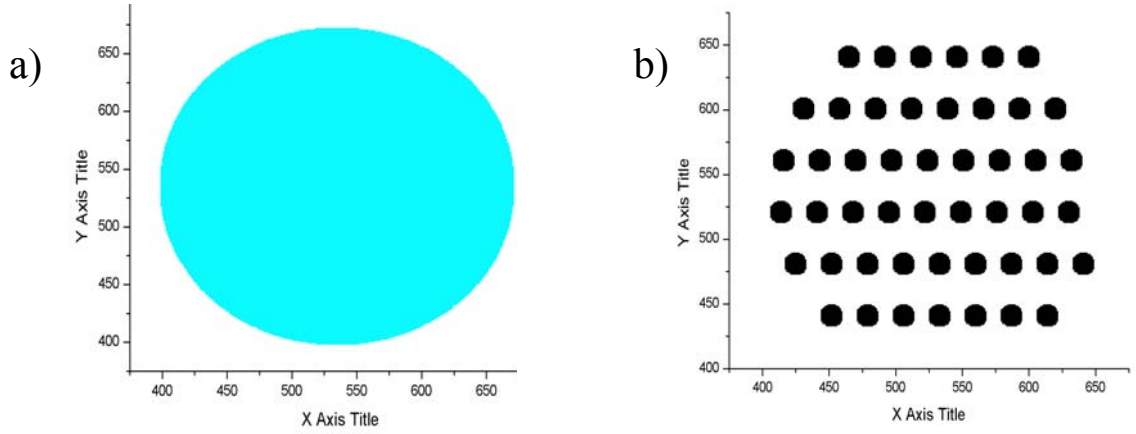

Figure 3-8: Masks for two hierarchy levels: a) continuous base level, b) split second level

The second level was generated to match the border lines of the first level.
The resulting mold had periodic pits ending in several finer channels (Figure 3-9).

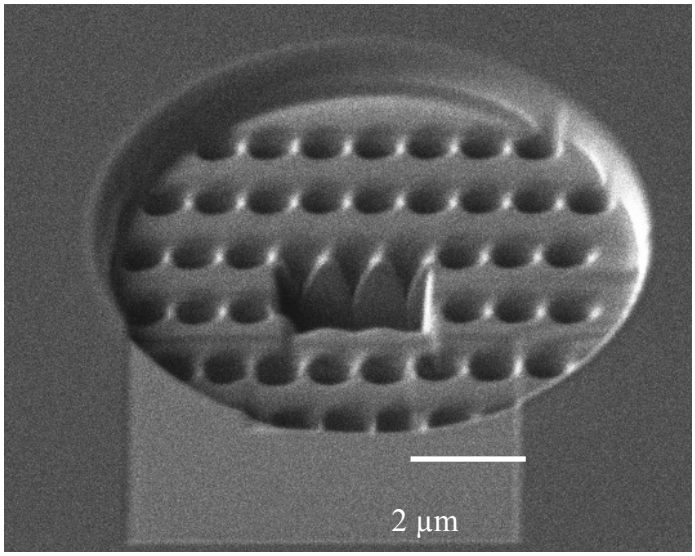

Figure 3-9: Example for *FIB*- milled hierarchical structure with a rectangular cross section for depth imaging

A cross sectional cut in the center gives an impression of the second hierarchy level. Using the same pattern data, arrays of hierarchical pillars can be fabricated by a subsequent molding process.

3.1.5 Reactive Compound Assisted Etching

Enhanced *FIB* milling with reactive gases was excluded, as significant unintended substrate roughening was found (Figure 3-10) in a test with XeF_2. A *FIB* milled trench (circle) was surrounded by a severely pitted silicon surface. The trench side walls were significantly roughened.

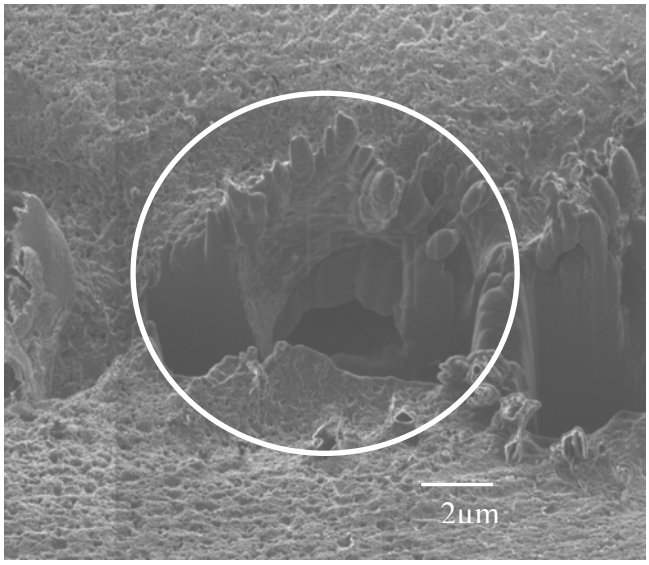

Figure 3-10: Corrosion of silicon surface using XeF_2 enhanced etching (*FIB*-figure)

3.1.6 Structure Height and Depth Control

In *FIB* milling the sputtered volume is directly proportional to the milling time. For milling patterns with constant cross section area, the milling depth therefore was considered to also increase linearly with milling time. For verification and for estimating the milling rate, milling depths were determined for a pattern milled at various milling times. The milling depth was determined either from cross section micrographs prepared by *FIB* or by replica molding and by measuring the height of the molded structures. As a disadvantage, the former method destroyed the template locally and the specimens were possibly modified by the cross sectioning and imaging. Using the molding technique, *PDMS* was poured into the template,

hardened and the replica characterized by *SEM*. For better imaging the replica, in some cases a thin gold layer was plasma deposited as common in *SEM* investigations on non-conducting objects.

3.2 Measuring Adhesion in Single Contacts and on Biomimetic Attachment Pads

Preliminary measurements on biomimetic adhesion pads, fabricated by photolithography, were performed on the Basalt I cantilever instrument and will be described in more detail in section 4.2. Several disadvantages were encountered. The measurements were disturbed by noise of about 20 µN in non-contact for samples generating pull-off forces of approximately 100 µN. Precise positioning on the sample was impossible and the indentation depth could not be predetermined.
An alternative device for measuring the adhesion properties of biomimetic attachment prototypes was to fulfill several requirements:

- better force and distance resolution at reduced noise
- sensitive sample surface detection and surface approach
- high automation and testing of different well defined sample areas

The two following solutions were found. The application of a modified commercial *MTS NanoXp* nanoindenter is subsequently described. Besides, A. Peressadko designed and built an improved version of the Basalt I instrument for enhanced performance. Both variants complement each other, and the choice of the appropriate method depends on the specific purpose.

3.2.1 Nanoindenter

Modern indenters measure various local mechanical properties by tracking the force and displacement continuously during the experiments [62]. Li *et al.* [74] used a Hysitron TriboScope ™ for measuring adhesion on polystyrene films. Recently the adhesion of biomimetic attachment devices has been tested by Northen *et al.* [65].

Within the present work a method was established for precisely controlled adhesion experiments on single microscopic contacts as well as on attachment structure arrays with

displacements and forces spanning the gap between macroscopic (e.g. *SFA*) and *AFM* measurements. A commercial NanoXp ™ (MTS) nanoindenter provides the necessary force and displacement resolution.

3.2.2 Working Principle and Experimental Setup

The *NanoXp* consists of a piston driven against a spring support by an electromagnetic field (Figure 3-11 a). The force is controlled by the current of an electromagnet surrounding the piston. Capacitive measurements determine the piston displacement. The indenter tip is mounted into a tap hole at the piston end. An x-y motorized stage positions the selected sample location below the indenter tip. The experiments are controlled by a computer running the *Testworks 4* software by *MTS* Systems Corporation (Oak Ridge, USA). Loading and unloading speed, indentation depth, sensitivity, test locations are a few of the adjustable parameters. When running a test, the machine first performs a surface find routine, and positions the tip close to the sample surface. In the main procedure the tip approaches the surface until contact is established. The tip indents the specimen to a predefined force or depth and than retracts in a defined way, yielding the force and displacement data. Based on this data, the machine calculates the mechanical properties e.g. Young's modulus and hardness of the specimen. Whole arrays of measurements may be performed automatically. The method allows for measurements on prototypes smaller than a square millimeter.

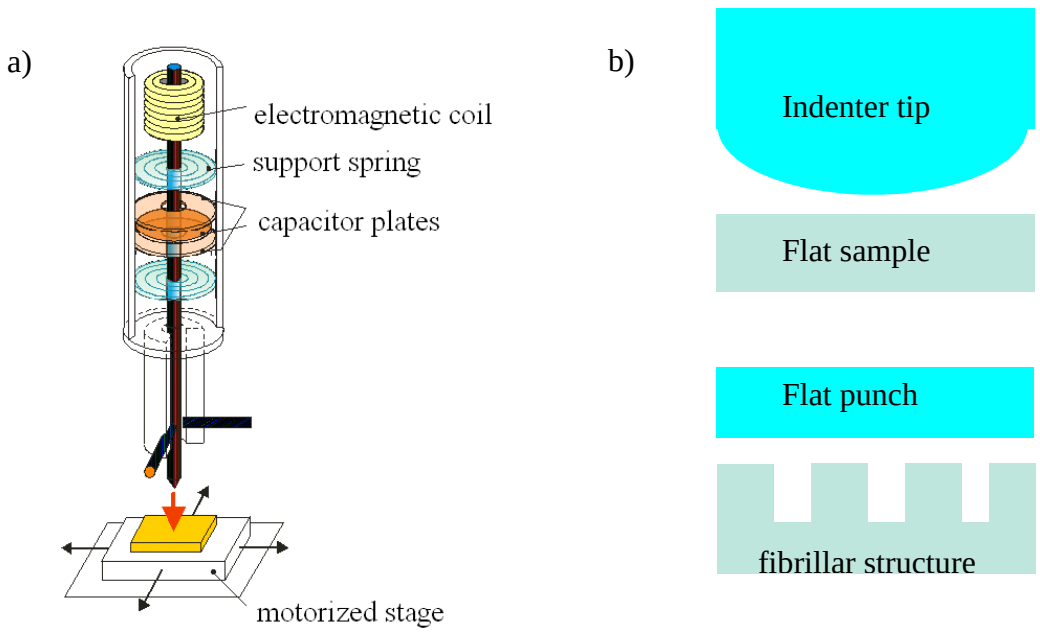

Figure 3-11: Nanoindenter setup (drawing by Dr. S. Enders) and experimental configuration: rigid tip on flat sample or structured soft sample against rigid flat punch

Two configurations are possible for measuring adhesion (Figure 3-11 b): Either a specifically shaped rigid indenter indents a flat polymer sample or a structured specimen.

Sample preparation and fixation

For standard *NanoXP* measurements, the samples are glued to an aluminium support block to be mounted in a sample tray. For thin and soft specimens, measurements are easily biased by the glue-sample interface properties. Therefore a glue-free sample fixation is desirable.
The sample surface has to be positioned within the measuring head range. For rigid samples this is ensured by pressing the sample surface against a counter plate giving the correct sample height before fixing the specimen in the sample tray. As this procedure could damage fine structures on our soft specimens, these were adjusted instead by positioning the surface within the focal plane of the indenter microscope. First a reference sample was mounted to the sample tray and the microscope was focused onto it. The focal plane therefore equaled the correct sample z-level. Afterwards the real sample, also mounted in the sample tray, was moved below the microscope. The sample holder allowed for adapting the sample surface height until it entered the microscope focus by rotating the threaded pin. The adjustment was performed without imposing external loads onto the sample. The sample support was designed to also minimize artefacts due to the sample-support interface and sample thickness effects. Errors due to insufficient interfacial stability may occur, as the material behaves apparently softer than the material itself. For poor sample support no valid measurements were obtained at all. The measured mechanical properties for thin samples were composed of the sample and the support properties. Such effects are commonly neglected for indentation depths less than 10% of the sample thickness [75]. Respective effects on adhesion were treated by Shull *et al.* [76]. In the present research work, the sample base was directly cast into the support cup, and no glue was needed for fixation, providing a stable support for the specimen on an appropriately thick layer of the sample material (Figure 3-12).

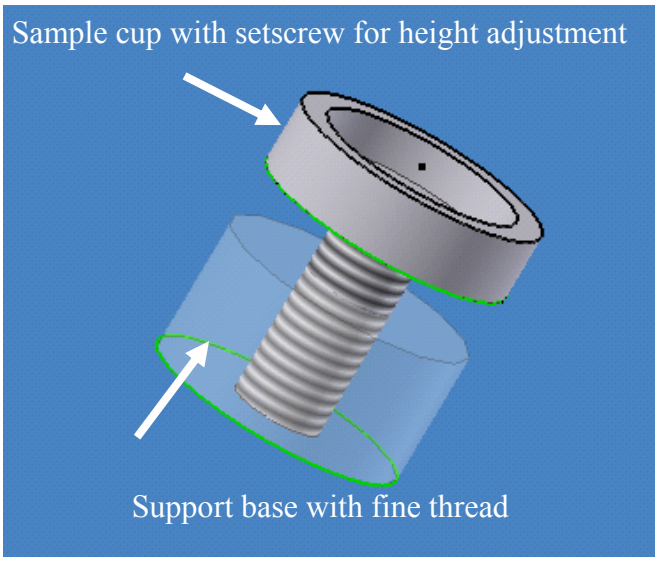

Figure 3-12: Adjustable Sample Holder with molding cup

The support base was mounted in a regular sample support. The sample cup height was increased by turning the fine thread setscrew counterclockwise and decreased by turning it clockwise by 750 nm per full-turn.

Structured surfaces were molded by using support cups with fillers (Figure 3-13). The cup was placed upside down on the molding template (Figure 3-13a) and filled with the polymer-solution via a syringe (Figure 3-13 b). After hardening the polymer in a drying cabinet, the sample was peeled off the substrate via the sample holder (Figure 3-13c).

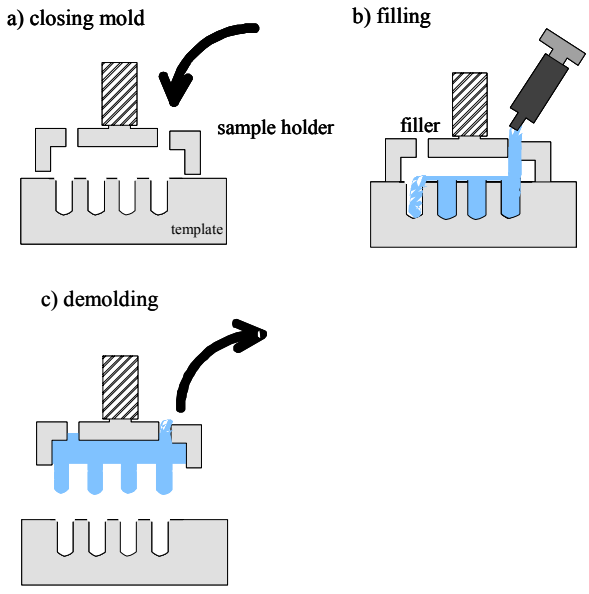

Figure 3-13: Molding of structured adhesion samples for the NanoXP: a) closed mold, b) filling process, c) opening the mold and demolding of the hardened polymer sample

A more universal 4” plate sample holder was also constructed to allow the fixation of various wafer supported samples by clamping. Height adjustment is again achieved by a threaded pin.

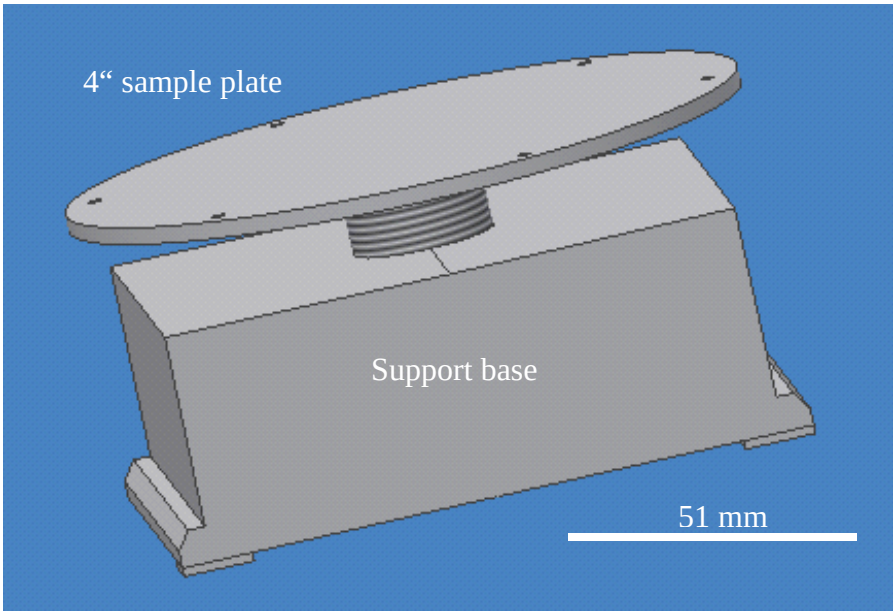

Figure 3-14: Universal sample holder for 4” samples with tap holes for sample fixation clamps

The support base of the 4” sample holder directly replaced the default NanoXP sample holder. The sample was fixed on the sample plate (e.g. with metal spring clips) and the height was adjusted by rotating the plate.

Modified Method for Adhesion Measurements

In general, nanoindenters are used for mechanical surface property measurements under compressive loads. After some modification of the test procedure, adhesion measurements were possible on the Nanoindenter XP. Compared to regular indentation experiments, the range had to be extended to the tensile force region. It was also necessary to define a surface detection criterion for soft materials (Appendix C.). The method required a condition for detecting the end of the experiment after the tip was out of contact.

New surface approach segment

The standard “surface-find” segment of the *Testworks* software was not accessible for user modification. Unfortunately it is optimized for rigid material testing. The surface of polymers is detected when the instrument already senses the sample support, thus considering the surface only after significant sample deformation. The standard method detects the surface by a peak value on the *load vs. displacement* readout. The standard surface approach is performed at high speed, inducing significant vibrations on the load vs. displacement channel. Thus it disturbs the surface detection in the beginning of the fine approach. As deactivating the standard surface detection led to software instabilities with the NanoXP with the applied Testworks 4 software, it was retained for coarse approach and supplemented by a refined surface find segment for soft materials. As a surface detection criterion the load vs. displacement readout proved sufficient for detecting the surface. The modified surface approach procedure is described in more detail in Appendix C.

Data markers

Before exporting and evaluating the data, some markers had to be set or modified manually (Figure 3-15). The z- marker was placed at the start of the pull-in segment and tagged the beginning of measurement. The T- marker assigned the end of the experiment. Drift compensation was performed between the two markers mentioned above. By setting the F-marker the zero force level was defined. This marker generally coincided with the z-marker. These markers were positioned at the end of the surface approach segment at zero force. Finally the S- marker was placed in the pull-in minimum to determine the point of zero displacement (point of contact). This marker was located at the beginning of the loading segment. After manually confirming the location of these markers, the data was automatically evaluated by a script written for Microsoft Excel™. The grossly automated data export and evaluation is described in more detail in (Appendix D).

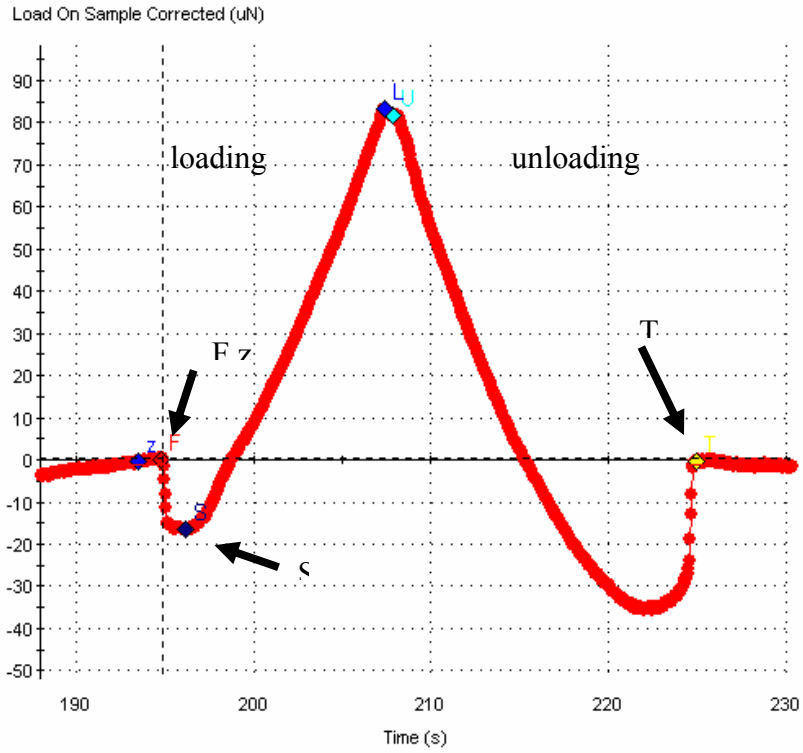

Figure 3-15: Load vs. time curve for a sapphire sphere (r=150 µm) on *PDMS* including markers for data export starting from marker z over the point of contact S to the end of the experiment T. The point of zero force is highlighted by F.

Drift Compensation

Standard *NanoXp* methods compensate the thermal drift by measuring the creep rate with the tip resting on the sample and subsequentially subtracting it from the measured data. As soft materials tend to creep at low loads, this procedure does not work for polymers. As adhesion measurements provide the exact point of contact and of exiting contact, drift was compensated between these two events by linear interpolation, namely between the start and end marker z and T.

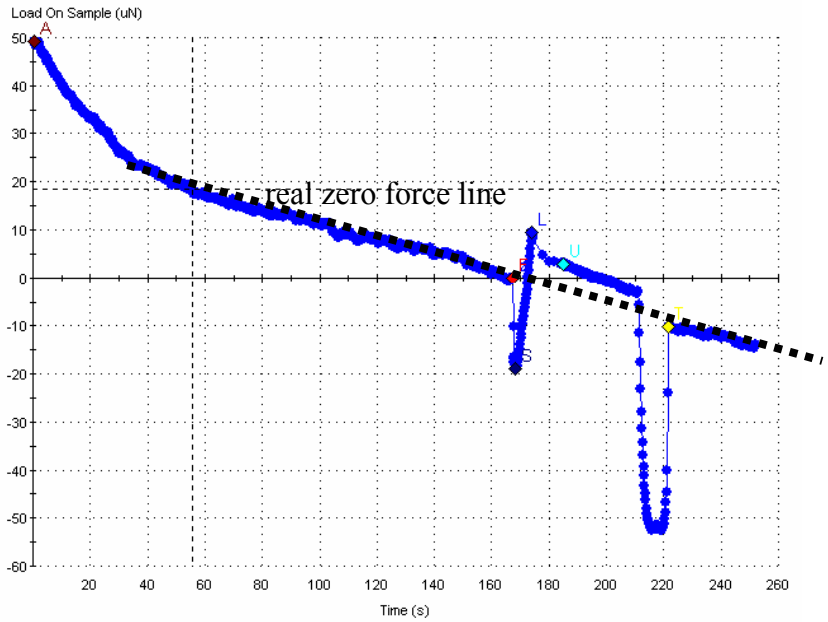

Figure 3-16: Load drift (slope of the zero force line between markers Z and T drawn as dashed line)

Finally typical adhesion load-displacement curves were obtained (Figure 3-17).

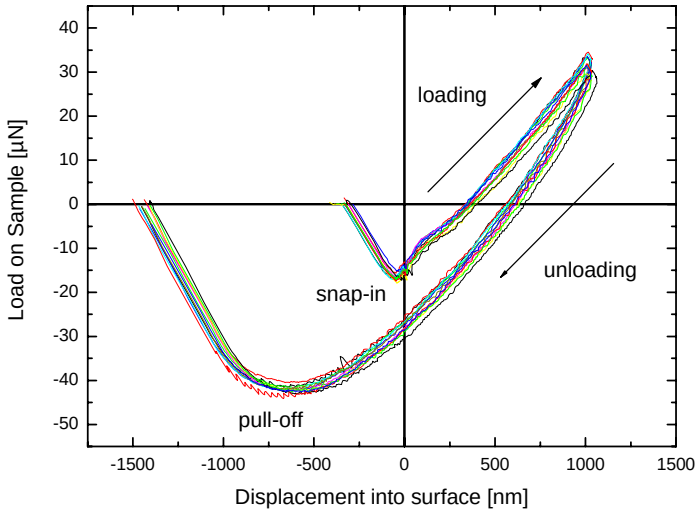

Figure 3-17: Data for 12 spot adhesion tests array on a *PDMS* sample and sapphire sphere (r=150 µm); indentation depth 1 µm

Artefacts

The measurements are sensitive to contaminations of the contacting surfaces. In our experiments we mostly had to deal with dust particles or polymer residues. A standard method

for cleaning the indenter tips is to press them into an aluminium disk several times. In our experiments, the polymer contamination persisted after this treatment. Cleaning in an ultrasonic acetone bath did not solve the problem. Good results were finally achieved by immersing the tip in cyclohexane for approximately one minute. The cleaning quality for the micron-scale tips was controlled by white light profilometry (section 2.6.2). A cyclohexane volume of 1 cm² was sufficient for cleaning the tips but the solvent had to be refreshed after two to three cleaning cycles as a reduced solving effect was observed. Figure 3-18 a) shows a 50 µm diameter sapphire punch contaminated after measurements on *PDMS*. After immersing the tip in cyclohexane, another white light profile was taken (Figure 3-18 b). The cleaning effect is obvious. Using acetone or ethanol did not produce comparable results.

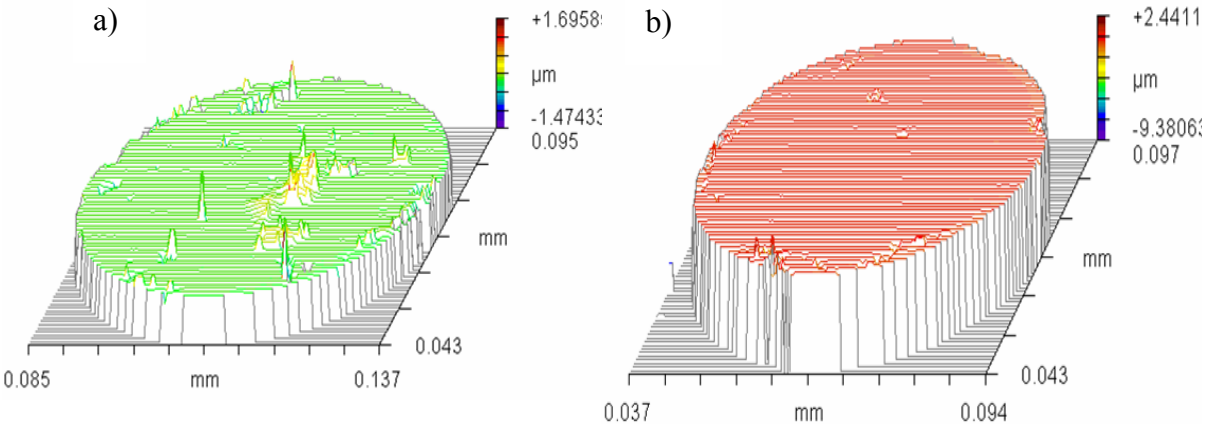

Figure 3-18: White light profile of flat punch indenter surface (50 µm diameter)
a: before cleaning with polymeric residues, b: after immersion cleaning in cyclohexane

Contamination of the substrate was not as critical as on the tips but also had to be considered. As the substrates usually are large enough to choose several locations for adhesion tests, solitary dust particles are not problematic. Wet cleaning is only recommendable for heavily polluted samples. As already well known in the micro electro mechanical systems *MEMS* community, liquids are problematic, as capillary forces tend to pull microscopic structures together and thus lead to stiction. As a classical remedy, a critical point drying process is performed. Although we did not apply this technique up to the present, it could become important for future specimens.

Flat *PDMS* samples were cleaned as proposed by de Souza [77] by rinsing the surface with Millipore water (high purity) and successively blow drying with a jet of nitrogen. This method is also sufficient for removing surface charges [51].

Force and Distance Resolution

Forces on the Nanoindenter XP are proportional to the current generating the electromagnetic field driving the indenter coil, whereas displacement is determined from capacitance measurements. The force resolution therefore depends on the accuracy for measuring currents, the displacement resolution on the precision of capacity measurements. Both properties can be determined with high accuracy. Therefore MTS specifies the displacement resolution with 0.01nm and the force resolution with 50 nN. In adhesion mode, two factors reduce the accuracy. First of all the measurements need to be dynamic to avoid material relaxation due to long constant loading. The force and displacement data are obtained at a preset sampling rate from 5 to 500 Hz. The sampling rate is to be chosen as high as necessary for sufficient accuracy but should also be kept as low as possible to ease data handling. Thus the displacement resolution for our experiments was 2.5 nm for a given sampling frequency of 40 Hz and a velocity of 100 nm/s. The precision of force measurements depended strongly on the correct detection of the point of contact as an offset reference point. For the given setup and laboratory location the noise in non-contact lay in the range of 0.5 μN. As a consequence, the precision of the measured force data was in the same range. So the Nanoindenter force resolution was adequate for measuring adhesion forces in the regime of single μN to 500 mN.

Comparing cantilever and nanoindentation methods

Cantilever instruments offer several advantages for displacement-force measurements. The point of contact is clearly determinable and in the operating range the stiffness of the cantilever is practically constant. A variation of force ranges is reached by using different cantilevers with appropriate stiffness.

On the other hand, a single cantilever measurement is always limited to relatively small displacements of the cantilever and the tip orientation relative to the investigated surface changes with the bending movement of the cantilever (Figure 3-19).

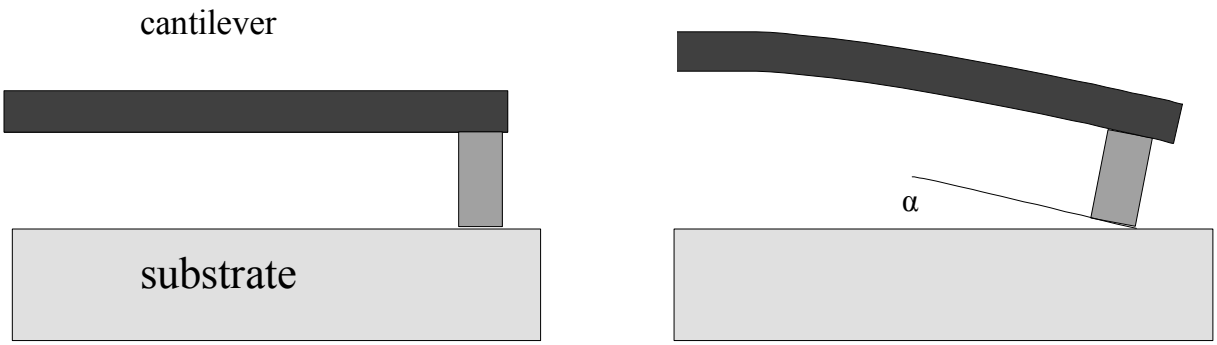

Figure 3-19: Misorientation of a punch tip due to bending of the cantilever

A standard contact mode cantilever is about 450 µm long, 3 µm high and 30 µm wide and has a spring constant *k* of approximately 0.2 N/m. It is commonly modelled as beam fixed at one end under bending load [78]. The end slope of the cantilever is calculated as for example in [79] 378 ff.:

$$\alpha = \frac{Fl^2}{2EI} \qquad (3\text{-}1)$$

With a moment of section *I* equal to

$$I = \frac{bh^3}{12} \qquad (3\text{-}2)$$

where F is the force applied at the end of the cantilever, *l*, *b*, *h* are the length, width and height of the beam and E is the Young's modulus of the cantilever material.
For a silicon *AFM* cantilever (*l* = 450, h = 3, *b* = 30 µm, *E* = 100 GPa) and an adhesive force of 1 µN the angle α is 0.8 °. As the angle is directly transferred to the cantilever-sample interface, a crack-like situation occurs at the contact.
A cantilever as applied for the Basalt tribometer has a spring constant of about 130 N/m and is several mm long. As the cantilever deflection is measured optically by a laser beam, the displacement data also includes an error due to shifting of the initial laser spot position during the test.

Alternative Instrumentation for adhesion measurements

In addition to the NanoXp, MTS offers a further Nanoindenter instrument with a better force resolution. The SA-2 nanoindenter was also evaluated for experiments. The software-modifications for adhesion measurements were easily transferred to the instrument as the control software Testworks 4 is also used with this instrument. Although the force resolution was better by a factor 50, it was not selected for experiments, for it is less flexible in the variation of the indenter tips.

For measuring adhesion of fiber arrays with in situ microscopy [3, 47], a micro-tensile tester (NanoBionix, *MTS* Systems Corporation, Oak Ridge, USA) was considered. In this instrument the upper cross head strains the tensile sample, while the force is measured by tracking the electromagnetic force necessary for keeping the lower cross head position constant. For *in-situ* adhesion tests the upper cross head was replaced by a contactor glass plate and a video microscope moving with the glass plate. The focus was set on the lower surface of the glass plate. The glass plate approached the surface until contact was registered. The video microscope image allowed determination of real contact as a function of the glass plate distance and force.

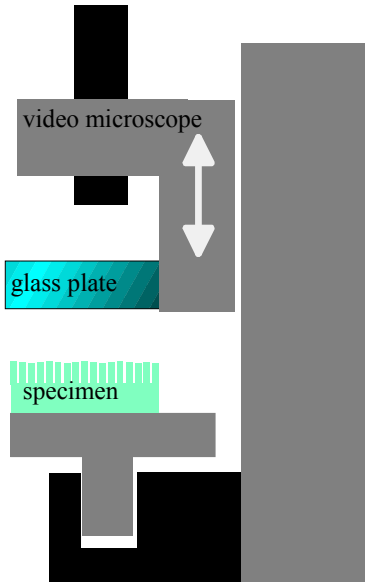

Figure 3-20: Setup for Adhesion measurements with an in-situ microscope

For this experiment only preliminary tests were performed. Some difficulties occurred in data interpretation, as the lower cross head was not absolutely stable at its position during measurements thus requiring additional compensation of the measured signal.

4 Experimental

4.1 Fabrication of Biomimetic Specimens

Two fabrication routes were followed in the present work: A part of the sample processing aimed at generating prototypes with specifically shaped and sized contact elements, whereas the second addressed the collective mechanical behavior of fibrillar attachment specimens. For the latter, the shape of the contacting fibrils was not predefined parameters like pillar width, aspect ratio and areal density were preselected.

4.1.1 Specifically Shaped Contact Elements

Specifically shaped contact elements were produced by cold imprinting (see section 2.4.4) and *FIB* micro-machining (see section 3.1).
In the present study, cold imprinting was applied to fabricate aluminium molds for spherical contact elements.
For generating an array of molds in a flat surface with the NanoXP, the positions and indentation depths or forces had to be defined individually. The maximum load was 500 mN. For a first molding template, a polished Al surface was indented with a sapphire sphere 500 µm in diameter. For the fabrication of adequate Nanoindenter specimens, one of the sample holders equipped with backside fillers was placed on the Al mold upside down (see section 3.2.2). The *PDMS* was injected with a syringe via one of the fillers. After degassing and hardening the polymer in a drying cabinet, the specimen was pulled of the mold with the sample holder.

The *FIB* technique was applied to generate micro molds in silicon and to prove the principle of generating specifically shaped indenter tips and roughness samples. As substrates rectangular pieces of a Silicon [001] wafers were chosen. Orientation on the sample was simplified by scratching a cross into the surface with two single strokes of a tweezers tip. When the structures were milled near the crossing point, they were easily retrieved in *FIB* imaging, *SEM* and light microscopy. After adjusting and positioning the sample, a reference trench was milled at the border of the field of view for the automatic drift correction. A pattern mask was computed and loaded to the *FIB* pattern generator. After focusing, the milling script was started. For long writing times the milling process ran overnight, after

configuring the *FIB* for automatic switch-off. Parameters like beam aperture, overlap and milling rate had to be determined individually for the respective structuring task.

Custom- shaped tips for *AFM* and the Nanoindenter were fabricated analogously to the micro molds, now using an inverted pattern. The tip was set free by removing the material surrounding it. In a first step, a standard *AFM* tip was truncated by a cut parallel to the cantilever. The tip was then turned by 90° to achieve a top view on the flat tip end. Now the pattern was loaded and centered on the apex. Milling the pattern yielded the designated tip (Figure 5-1 a and b).

4.1.2 Bioinspired Fibrillar Attachment Structures

Pillar array templates were produced in cooperation with Jens Ulmer (University of Heidelberg, department Spatz) by standard photo lithography in SU-8 photo resist. First the wafers were heated for H_2O desorption. Subsequently the SU-8 resist was spun on the substrate using a spin coater with vacuum chuck for fixation. Samples were produced at rotational speeds of 1500, 2000 and 3000 rotations per minute.

After a soft and prebake according to the resist distributor manual instructions, the wafer was cut into square centimeter sized specimen chips. The samples were exposed for 2.5 and 3 seconds. The post bake, chemical development and hard bake were also performed according to the resist data sheet. The molding templates were silanized with 1, 1, 2, 2, -Perfluorotrichlorsilane ($C_{10}H_4C_{l3}F_{17}Si$) to prevent stiction with the molded *PDMS*. The silane was applied in gas phase under vacuum condition and stabilized by a 60 minute thermal treatment at 90°C afterwards. A prepolymer-crosslinker solution (10:1) of Sylgard 184 (Dow Corning) was applied to the template and degassed under vacuum for 45 min and subsequently hardened overnight at 80°C. The samples were ejected by peeling.

Parameters like structure height, width, inclination angle and areal density were varied by applying X-Ray lithography (section 2.4.6). The specimens were fabricated at the *Singapore Synchrotron Light Source* (*SSLS)* using a synchrotron X-ray source for exposure of SU-8 material. The layout for circular structures, square and rectangular structures were defined. For each geometry, areal densities of 2, 5, 10 and 25% were predefined. The circular pillar radii were 200, 500, 700, 1000, 2000, 5000 and 10000 nm. The square edge lengths matched

the radii of the circular structures. These lengths were also equal for the rectangular shapes, the length being 20 times as long as the given values. The layout can be found in more detail in Appendix A.). The structures were generated in SU- 8 10 photo resist (MicroChem Corp.) and were directly used as attachment structures.

Some of the structures produced at the *SSLS* were replica molded with *PDMS* (Sylgard 184 Dow Corning), using the same polymer for the negative as for the positive. In a first step, some *PDMS* primer-crosslinker solution was poured onto the silanized SU-8 master. After degassing the material under vacuum, the *PDMS* was hardened at about 80°C overnight. The *PDMS* sheet was subsequently peeled off the SU-8 substrate and passivated by Silanization as described in section 3.1.3 in order to prevent stiction between the *PDMS* template and the specimen. The molding of the *PDMS* specimen was performed analogously to the fabrication of the negative, the master this time being the *PDMS* sheet.
After the hardening process, the sample was peeled off the template, ready for use in adhesion experiments. The peeling was achieved by carefully detaching the sample edge from the template with a scalpel and subsequent lifting the *PDMS* sheet. The sheet was not to snap back into contact, as this could have destroyed the structures.

Micromolded fibrillar specimens were also fabricated by electrochemical template etching. In a discussion about suitable techniques for template production, J. Spatz (then at University of Heidelberg) proposed to consider the work of Lehmann and Föll [80] . Guided electrochemical wet etching of parallel micro pores in silicon and nano pores in alumina provides a promising technique for the fabrication of attachment structure templates. Steinhart *et al.* [67] demonstrated the production of polymeric nano-tubes with this technique. The preliminary studies in the present work were conducted in collaboration with the group of Martin Steinhart at the MPI of Microstructure Physics, Halle, department Gösele.

In silicon, the positions of the pores were predefined by photolithography [81] . The pores were available for radii greater than 600 nm. In alumina the pores form spontaneously in a hexagonal arrangement [82].

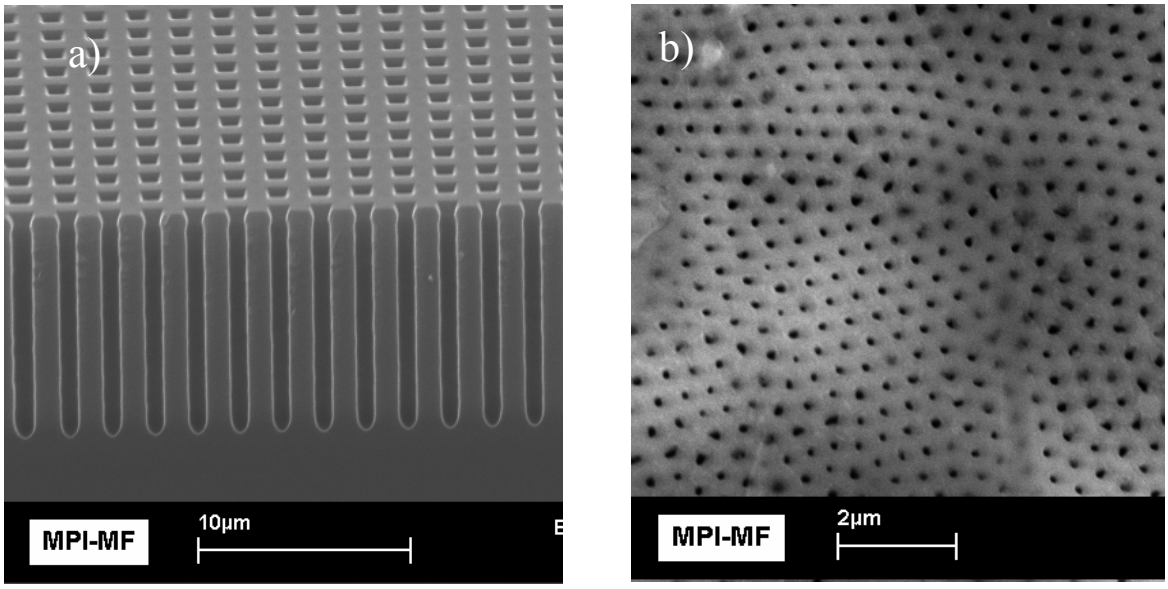

Figure 4-1: molding templates etched at the MPI of Microstructure Physics, Halle:
a) edge micrograph of a stuctured silicon wafer surface with rectangularly arranged straight walled channels 10 µm deep and 1 µm wide (fabricated by S. Matthias, MPI Halle), b) self assembled hexagonally arranged parallel pores in alumina 180 nm in diameter and 900 nm deep (fabricated by K. Schwirn, MPI Halle)

The pore sizes range within several hundred nanometers which corresponds well with the size of gecko attachment hairs [44].
For straight walled templates, the molding and demolding of *PDMS* samples was done analogously to that for photolithographycally or *FIB*- milled molds. The template was passivated by a silanization and filled with the polymer, which was peeled off after the hardening. For undercut structures this procedure was inadequate. The sample had to be set free in a sacrificial process as proposed by Steinhart *et al.* [67] for the fabrication of polymer nanotubes. A thermoplastic polymer (e.g. polystyrene) was distributed on the sample surface and heated beyond the glass transition temperature. At decreased viscosity the material was dragged into the mold by capillary forces, forming hollow tubes within the template. The flow process was additionally supported by pressing a glas slide on the polymer. The slide also simplified the fixation of the sample for the template removal. After cooling down, the silicon template was dissolved in a 30% KOH solution at 80°C. This method is appropriate for the fabrication of undercut structures and may be combined with other structuring methods.

4.1.3 Material

As material properties play an important role for adhesion (section 2.2.3), adhesion specimens were produced from compliant polymers (*PDMS*, *PVS*) with elastic moduli in the MPa range

and stiff polymers (SU-8 Photoresist, Polymetacrylate resin) in the GPa regime. The fabrication of *PDMS* samples was described in section 3.1.3. The polyvinylsiloxane exists as a commercial solution (President light body Coltène/Whaledent AG, Altstätten Switzerland) consisting of a prepolymer and a hardening agent. The components were either mixed automatically in an applicator gun or manually. SU-8 samples were produced as described in section 2.4.6. The polymetacrylate resin (Serva Electrophoresis, *Spurr* embedding kit Cat.-#210050) was mixed and thermally hardened according to the distributor's instructions.

4.2 Basalt I Adhesion Measurements on Fibrillar Structures

First measurements were conducted using the BASALT I tribometer.
The Basalt tribometer (Figure 4-2) measures force by laser beam deflection on a glass or metal cantilever mounted on a piezo actuator. Three micro-positioners control the vertical sample position and tilt. The forces are determined from the cantilever deflection as described in section 2.3.

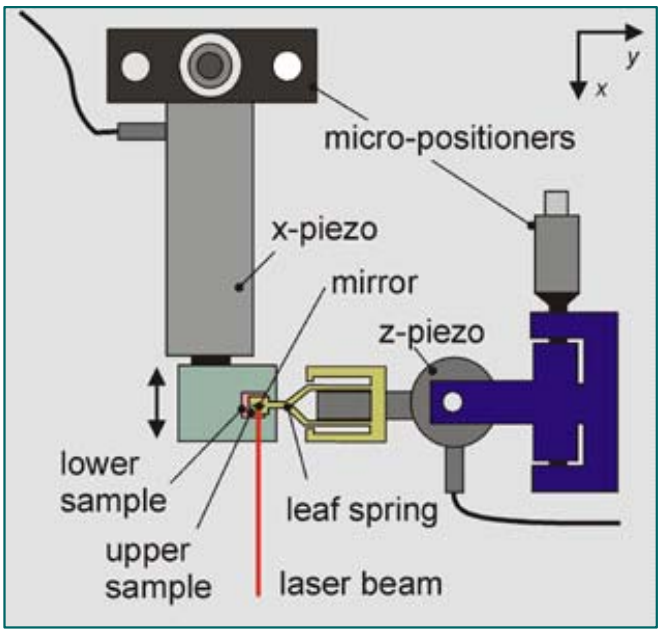

Figure 4-2: top view sketch of the cantilever tribometer BASALT (Dr. S. Gorb)

The force resolution for the applied glass spring with a spring constant of 130 N/m lies in the µN range but is limited due to noise of about 20 µN in non-contact. Neither additional damping nor excluding air flow showed any improvement. Before testing, the sample is positioned closely to the probe assembly of glass spring and a sapphire ball tip (1.5 mm diameter). The coarse approach is controlled optically by using a microscope, whereas contact

during fine approach is determined by the cantilever deflection. The tip is withdrawn until it loses surface contact. The loading-unloading is controlled by the piezo displacement and automatically approaches and retracts the tip, while acquiring the distance- force curve. Due to noise, first experiments did not yield reliable adhesion data. The indentation depth is not predefineable, but only the maximum absolute tip displacement during a loading-unloading cycle. As a consequence measurements are hard to compare and deep indentation occasionally leads to mechanical damage of the specimen.

Measurements were performed on photolithographically fabricated *PDMS* pillar arrays. The rectangularly arranged 5µm wide, 5 to 10 µm high pillars were spaced at 10 µm (center point to center point) and covered 20 % of the surface (Figure 4-3).

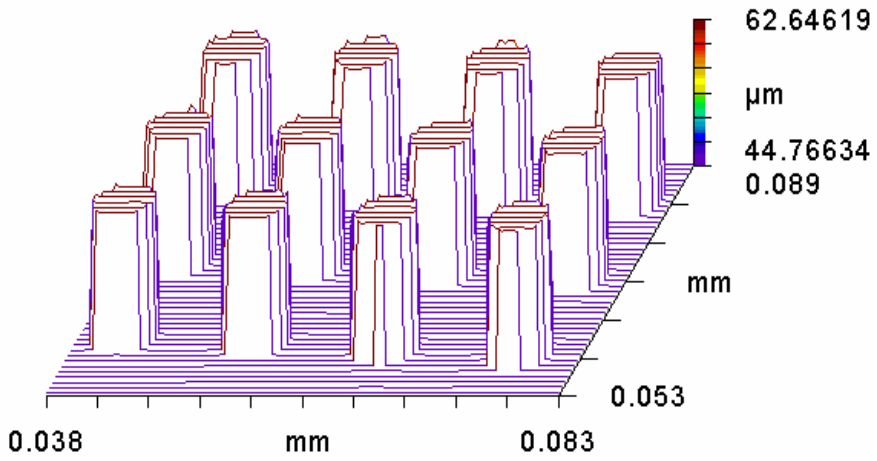

Figure 4-3: White light profile of a sector on a pillar array (diameter 5µm, spaced at 10 µm,16 µm high)

Each field was tested at different positions at least three times, varying the maximum load. The samples, glued to a glass substrate, were mounted on the Basalt stage after cleaning them with ethyl alcohol.

4.3 Nanoindenter Adhesion Measurements- General Issues

For microscopic attachment pads improved force and displacement resolution was necessary. Thus a commercial nanoindenter was modified for adhesion measurements. A refined surface approach procedure was defined and the sample support setup was altered to avoid damage of the specimens.
The nanoindenter allows for precise control of the loading and unloading procedure of the adhesion tests. Before starting specific adhesion test series, the influence of parameters like indentation depth and unloading speed were investigated. Maximum loading and retraction speed are known to significantly influence the adhesion of viscoelastic polymer materials. These preparations were necessary to determine whether variations in the testing conditions were critical for the results of the measurements and to define the conditions for the comparability of different adhesion tests.

4.3.1 Adhesion Measurements at Various Indentation Depths and Retraction Speeds

The influence of indentation depth was determined for various penetration depths on *PDMS* material, using a spherical sapphire tip (r=250 µm). Tests were run at indentation depths of 100, 500, 1000, 2000 and 3000 µm.

A series of tests was performed on a spherical sapphire tip (r=250µm) at various retraction speeds to investigate the velocity dependence due to viscoelastic losses (section 2.2.2). The flat material samples were fabricated as described in section 3.2.2. The *PDMS*-crosslinker solution (10:1) was poured into the sample holder cup and hardened overnight at 80°C. After adjusting the sample z-position, the force-distance curves were measured for each tip geometry on different spots of the sample. The indentation depth was kept constant for each series of measurements.

4.4 Single Contact Nanoindenter Adhesion Measurements

The collective attachment behavior of periodic attachment devices depends on the adhesion property of the individual contacts. The single contact geometry and size significantly influence the performance and adhesion pressure of the whole system. Thus single contacts have to be fully understood before going to more complex levels of hierarchy.

Nanoindenters are capable of accessing the adhesion of single microscopic contacts as well as that of clusters. In the following section respective experiments are described.

4.4.1 Adhesion on Modified Surfaces

The effect of surface energy is accessible by chemical modification of the sample surface by surfactant coating or plasma treatment. For a first experiment in cooperation with E. de Souza, the pull-off force on *PDMS* was measured on the NanoXP with a sapphire flat punch (r=25µm), before exposing the sample to a thorough 3 minute oxygen-plasma treatment (200 W, at a partial O_2-pressure of 1 mbar in a vacuum of 0.3 mbar) in order to modify the surface by an oxide layer. The sample was transported in Millipore water to retard contact angle recovery before the experiment. For the measurements the sample was removed from the water container and dried with a nitrogen jet. The contact angle was measured again one minute after oxidation and after six hours of recovery. In a subsequent experiment a *PDMS* surface was again treated with an oxygen-plasma (200 W, 10 s, at a partial O_2-pressure of 1 mbar in a vacuum of 0.3 mbar). The choice of these plasma parameters prevented the previously observed surface cracking.
Consecutive adhesion measurements were conducted during the recovery time of 400 min, while simultaneously measuring the contact angle on a reference sample.

As another way of modifying the surface properties of the samples, we silanized the surface with 1, 1, 2, 2, -Perfluorotrichlorsilane ($C_{10}H_4C_{l3}F_{17}Si$) as described in section 3.1.3. After performing adhesion measurements with a 50 µm sapphire flat punch on the NanoXP. The adhesion was measured again after the silanization process.

4.4.2 Diverse Contact Element Sizes

Classical contact mechanics do not distinguish between the mechanical properties of the contacting bodies but describes them as reduced properties for the contact. Hence for a first order approach it is irrelevant which of the contacting bodies is the indenter and which the substrate, as the classical contact mechanics are defined for small deformations only. Variously shaped rigid indenter tips are commercially available, and were used as contact elements against compliant polymer substrates for testing the scaling behavior of micro contact adhesion.

In a first experiment differently sized sapphire hemispheres and flat punch indenters were tested on *PDMS* flat samples. The available tip sizes and geometries are listed in Table 4-1:

Table 4-1: Applied indenter geometries, sizes, materials and measurement technique

Shape	**Radius [µm]**	**Material**	**Instrument**
Flat Punch	**5**	**Al_2O_3 (Sapphire)**	**NanoXP**
Flat Punch	**15**	**Al_2O_3 (Sapphire)**	**NanoXP**
Hemisphere	**5**	**Al_2O_3 (Sapphire)**	**NanoXP**
Hemisphere	**50**	**Al_2O_3 (Sapphire)**	**NanoXP**
Hemisphere	**150**	**Al_2O_3 (Sapphire)**	**NanoXP**
Hemisphere	**250**	**Al_2O_3 (Sapphire)**	**NanoXP**
Hemisphere	**1,5**	**SiO_2**	***AFM***

In the applied configuration, the respective indenters were brought in contact with the *PDMS* and retracted while recording the force-distance data.
For each tip, the surface approach conditions have to be determined separately. Standard parameters for finding the surface by the snap-in peak minimum, using the applied configurations on *PDMS* are summarized in Table 4-2.

Table 4-2: Exemplary surface find parameters for different tips on flat *PDMS* in pull-in mode

	Approach distance [µm]	Surface approach sensitivity [%]	Surface Lock [%]
Punch r =25 µm	**35**	**8**	**8**
Punch r =15 µm	**35**	**8**	**3**
Punch r =5 µm	**35**	**8**	**3**
Sphere r =250 µm	**35**	**9**	**9**
Sphere r =150 µm	**35**	**9**	**9**
Sphere r =50µm	**35**	**8**	**4**

The approach distance defines the range within which the surface has to be detected during a single test. The sensitivity of the internal surface approach procedure is given by the “surface approach sensitivity value” and the sensitivity of the refined surface sensing is preselected by the “surface lock” value. For more detail the reader is referred to Appendix C.

In addition to the Nanoindenter tests a 3 µm diameter *AFM* tip sphere was adhesion tested on *PDMS*.

Further experiments were performed on photolithographically structured *PDMS* samples using the Nanoindenter XP (section 3.2). The samples again consisted of rectangularly arranged *PDMS* fiber arrays with 20% areal density, the pillars being 5 µm wide. Aspect ratios of 2 and 3 were available. The *PDMS* material aside of the structured fields was taken as flat reference material.
Adhesion was determined applying a sapphire punch 50 µm in diameter and a sapphire ball 300 µm wide. The fibrillar structures were indented to a depth of 1000 nm and the pull-off forces were determined for a retraction velocity of 100 nm/s.

4.5 Nanoindenter Adhesion Measurements on Fibrillar Structures

The adhesion of structured *PDMS* samples was measured using the Nanoindenter XP (section 3.2). The samples again consisted of rectangularly arranged *PDMS* fiber arrays with 20% areal density, the pillars being 5 µm wide. Aspect ratios of 2 and 3 were available. The *PDMS* material aside of the structured fields was taken as flat reference material.
Adhesion was determined applying a sapphire punch (r = 50 µm) and a sapphire ball (r = 150 µm). The fibrillar structures were indented to a depth of 4 µm for shallow indents and 15- 30 µm for deep indentation. The pull-off forces were measured for a retraction velocity of 100 nm/s.

Tests were also performed on fibrillar SU-8 structures 2 µm high with a spherical sapphire punch (r=150µm).

5 Results

The following sections contain results of the sample fabrication and for adhesion force measurements on single contact elements and periodic fibrillar attachment arrays. The errors were calculated according to statistical error analysis equation if not explicitly defined separately in the text:

$$\Delta x = \frac{t(q)}{\sqrt{q}} s \qquad (5\text{-}1)$$

where *t(q)* is a tabulated correction factor derived from Student's distribution function [83] and s the standard deviation. For $\Delta x < s$, the standard deviation *s* was directly used as error. The factor *t* was chosen for a 99% significance of the error.

5.1 Fabricated Samples

Several methods for fabricating specifically shaped micro contacts as well as periodic arrays of fibrils without tip shape control have been tested Table 5-1. For the former the results of *FIB* milling and cold imprinting are presented. Replica molding results from optical and X-ray lithography and electrochemical etching represent the latter category.

The given errors for measured force and distance values were determined statistically from the standard deviations. Errors of length within the micrographs were estimated and taken as a constant value. For profilometry heights the standard deviations were directly taken for a set of more than 20 tests each.

Table 5-1: Overview over micro structuring methods applied in the present work

	FIB	Cold Imprinting	Photolithography	X-ray lithography	Electrochemical Template etching	
Material	Silicon, replication polymers	aluminium	SU-8 photo resist, replication polymers	SU- 8, replication polymer (*PDMS*)	aluminum	silicon
Feature diameter	>300nm	As indenter tip	> 1µm	>200 nm	180- 400 nm	>1 µm
Aspect ratios, structure depth	<3 shape control < 10 no shape control	1-2	<10	1-100 and more	full substrate depth	Full substrate depth
Tip geometry control	yes	yes	no	no	yes	yes
Fabrication sequence	sequential	sequential	parallel	parallel	parallel	parallel
comments	Superposition of beam profile, ion implantation	Elastic relaxation of imprints	Well established for low aspect ratio micron scale structures	High surface roughness with obtained structures	Sacrificial process, hollow structures	Sacrificial process, hollow structures

5.1.1 Micro Contact Elements with Predefined Shapes

Figure 5-1 c shows a toric contact element cut on a standard silicon *AFM* cantilever tip. The torus has an outer radius of 1 µm and an inner radius of 500 nm.

FIB milling was also demonstrated for fabricating molding templates for arrays of toric contact elements (Figure 5-1 c) and for pillars (Figure 5-1 d). In both cases a molding template was milled into a silicon wafer surface and subsequently molded with *PDMS*. After curing, the polymer structures were removed by peeling the backing film of the silicon substrate Figure 5-1 c and d. The 10 µm spaced pillars were 5 µm wide at the base and about 15 µm long. The pillars in Figure 5-1 d were conically shaped with decreasing diameter towards the tips at an asymmetric tip opening half-angle of approximately 20° on the left side and orthogonal sidewalls on the right. The structures were cut without drift compensation. The toric elements were 5 µm wide, the torus ring being 500 nm in diameter.

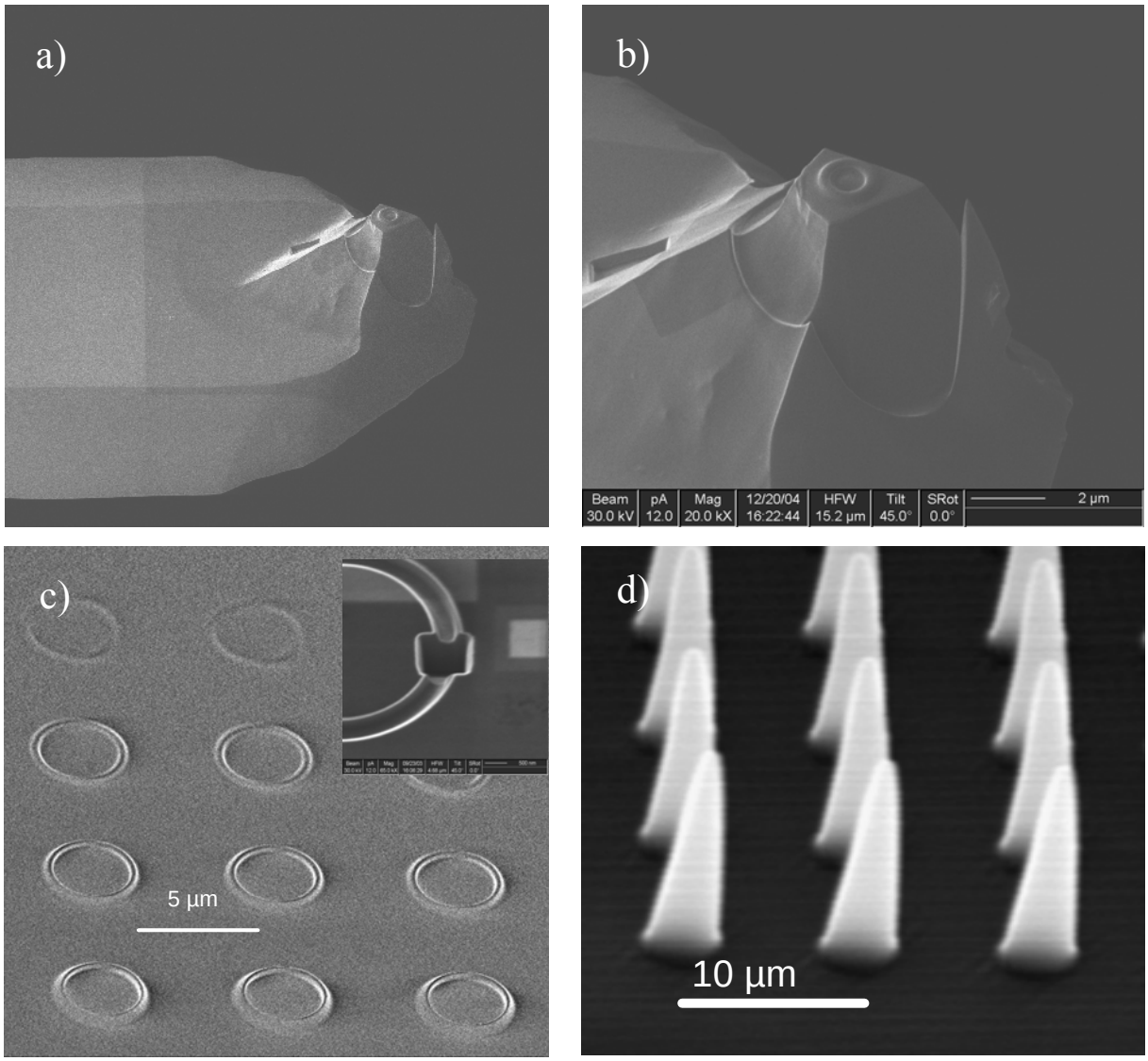

Figure 5-1: *FIB* milled shapes: a) modified *AFM* tip with a toric probe, b) closeup, c) toric *PDMS* contact elements, 1 µm outer and 500 nm inner diameter, cast from *FIB*-machined silicon; inset: cross section of the mold; d) pillar arrays in *PDMS*

The inset in Figure 5-1 c depicts a cross section of a toric mold channel to verify the round shape. The upper row was written at regular milling time, whereas in the following rows it was multiplied by a factor two, three and four.

Predefined shapes were also realized by cold micro imprinting. Indenting a coarsely polished Al surface with a sapphire sphere (r=250µm) yielded an array of spherical indents that were used as molding templates for *PDMS* (Figure 5-2).

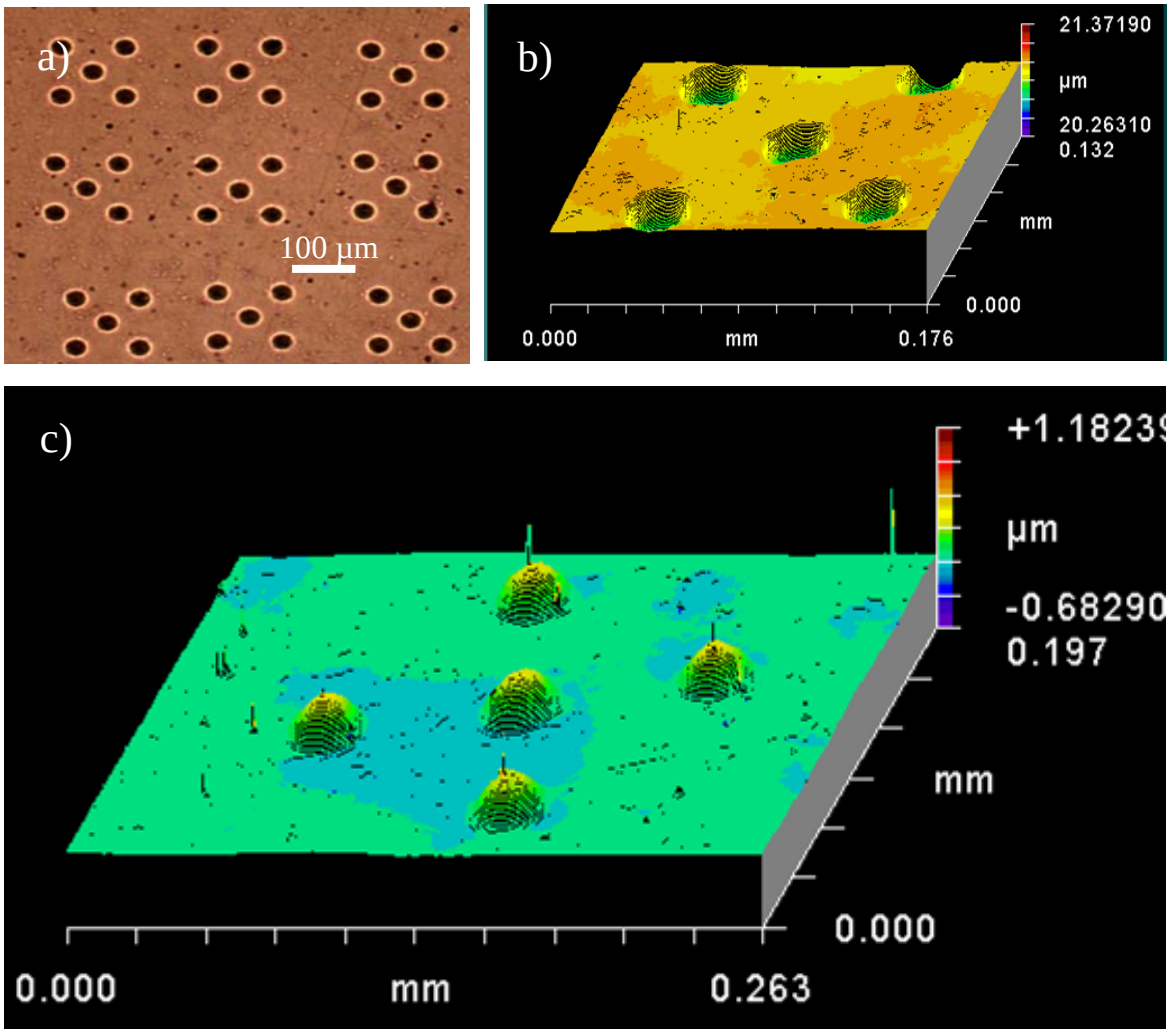

Figure 5-2: a) Imprints of a sapphire sphere (300 µm in diameter) in a coarsely polished Al surface (light microscopy), b) white light profile of the imprints, c) *PDMS*-cast of Imprints (white light profile).

The indent center points were positioned within squares 100 µm x 100 µm with four indents on the respective corners and a fifth indent in the center. Nine of these squares were fabricated on the same molding template thus generating 45 single contact elements. The single indents were spaced at sufficient distance to test a single contact element without touching the adjacent structures.

The template was micro molded with *PDMS Sylgard 184* in order to obtain polymeric contact elements (Figure 5-2 c). The templates and *PDMS* samples were characterized by white light profilometry (Figure 5-2 b and c). The indents were approximately 30 µm wide.
The molded contact elements were 337 ± 28 nm high, 34 ± 1 µm wide and had a radius of curvature of 334 ± 23 µm. The radius of curvature on a single contact feature increased to

400 µm at the base of the structure, where the spherical geometry smoothly transited into the flat base. Some of the contact elements show sharp peaks due to contaminating particles.

5.1.2 Arrays of Fibrillar Attachment Structures

Fibrillar adhesion structures were produced by photolithography, X-ray lithography and replica molding.
Several square centimeter sized adhesion samples were produced in cooperation with Jens Ulmer (University of Heidelberg, group Prof J. Spatz). The specimens consisted of 5 µm wide circular pillars, 9 and 16 µm high (Figure 5-3) spaced at 10 µm.

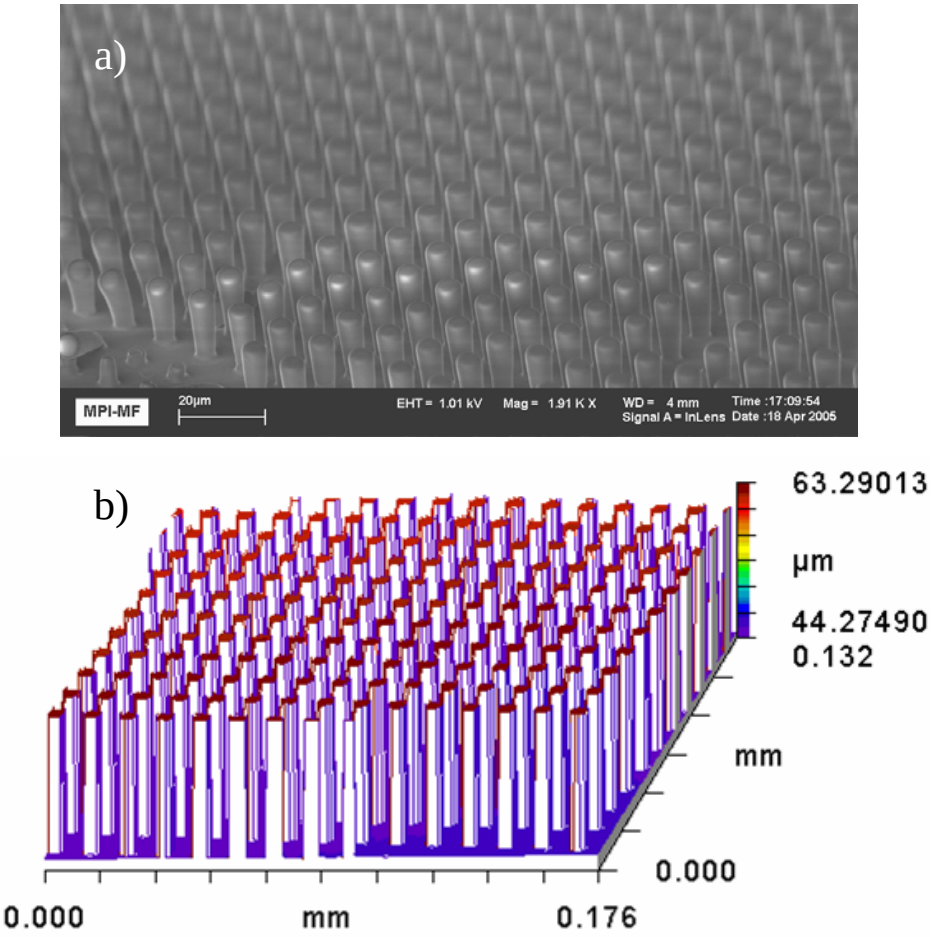

Figure 5-3: Photolithographic *PDMS* pillars 5 µm in diameter with an aspect ratio of 3 fabricated in cooperation with J.Ulmer, department Spatz, University of Heidelberg; a) *SEM* image, b) white light profile

The structure dimensions were characterized by white light profilometry (section 2.6.2). The fibers were of regular shape and uniform height (Figure 5-3 b).

The three-dimensional white light profile shows a closeup section (176 µm x 132 µm) of the fabricated *PDMS* array without any defects (e.g. missing pillars).
The pillar heights are uniform and can easily be determined from the two-dimensional profile plot (Figure 5-4).

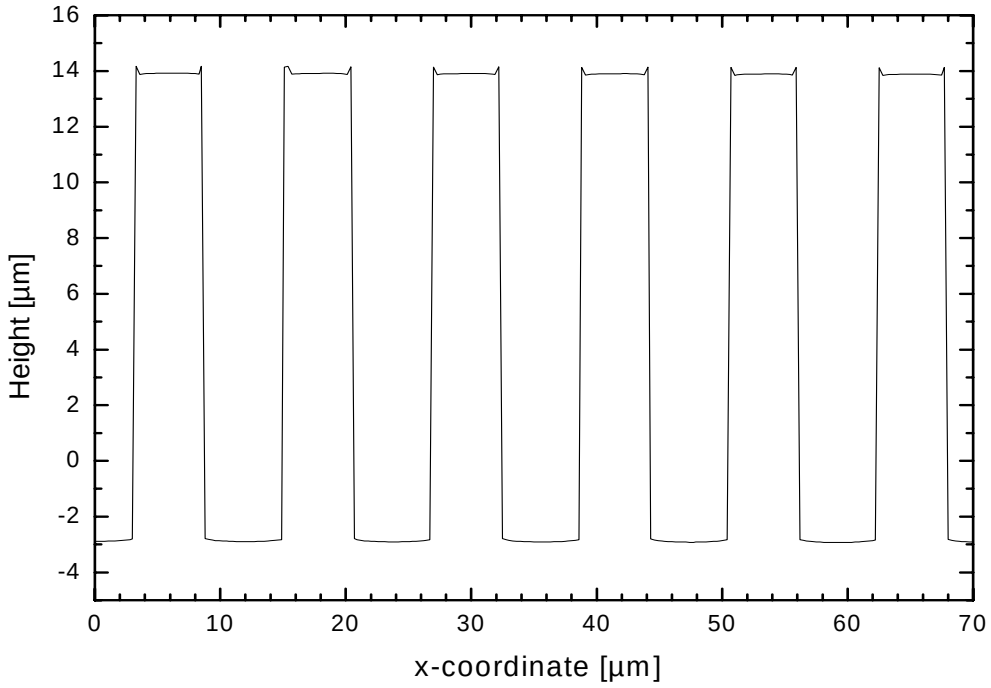

Figure 5-4: Line profile cross section of a fibrillar *PDMS* sample as in (Figure 5-3)

The mean pillar heights are listed for given spin-on radial frequencies in Table 5-2:

Table 5-2: Spin coating frequencies, estimated and measured heights for SU-8 structures

Rotation frequency	**estimated height [µm]**	**Measured height (white light profile) [µm]**
1500	**20**	**16 +/- 1**
2000	**15**	**12 +/-1**
3000	**10**	**9 +/-1**

The errors were assumed equal to the estimated observational accuracy of 1 µm.
The reference values were estimated according to distributor data.

5.1.3 X-Ray Lithography

According to the optimization guidelines by Spolenak *et al.* [7] a mask layout for cylindrical pillars was calculated. Besides, a set of square and rectangular structures were defined. The reference sizes can be found in Appendix A.). Not all the reference structures were realized and the dimensions of the fabricated SU-8 structures did not fully match the specifications. Nevertheless a set of structures with different geometries and sizes were obtained.
The respective tip surfaces were rough in the 10-100 nm regime.

5.1.4 Replica Molding

The SU-8 structures treated in section 2.4.6 and 4.1.2 were replicated in *PDMS* (Figure 5-5 a-c).

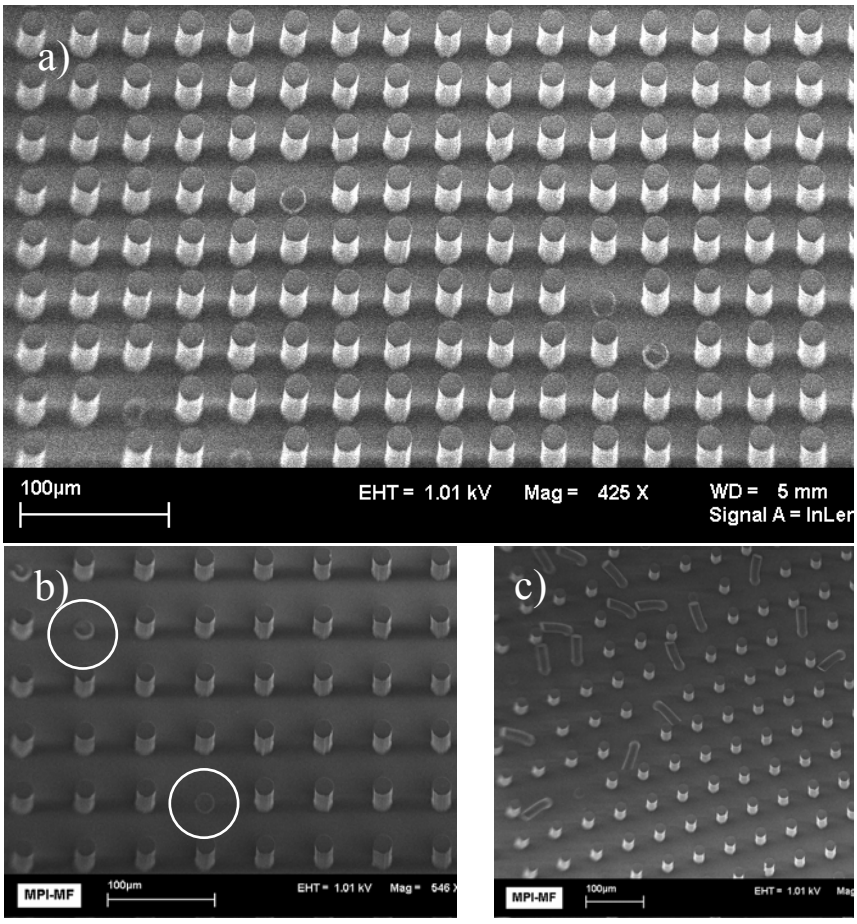

Figure 5-5: *PDMS* replica array of pillar SU-8 structures described in section 2.4.6; a) overview, b) single pillars missing, c) pillars partly bent and attached to the substrate

After relieving the *PDMS* specimens from the silanized *PDMS*-template, pillars and lamellae analog to the SU-8 origins were replicated.
Within the replicated pillar arrays the majority of structures were intact, although at some locations solitary pillars were missing (Figure 5-5 b) and others suick to the substrate (Figure 5-5 c). The white circles in Figure 5-5 b highlight two missing pillars within the array.

Lamellar structures were also replicated. Some of the lamellae were torn or distorted by bending to a neighboring structure (Figure 5-6 a).

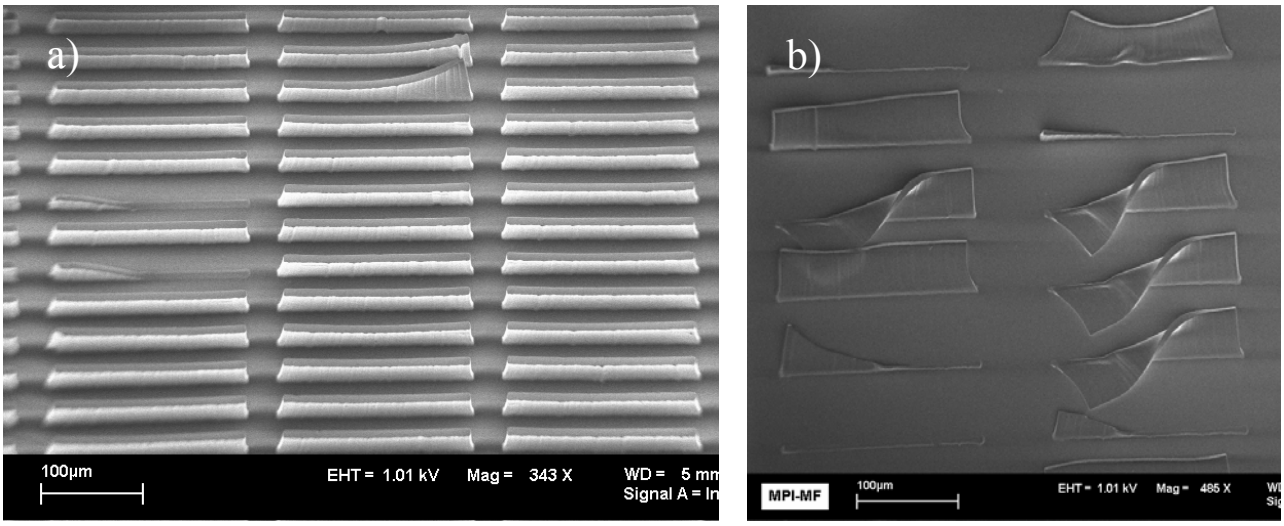

Figure 5-6: Self-supporting *PDMS* replica of a) thick SU-8 lamellae, b) distorted thin lamellae too soft for self-support

Thin lamellar structures were damaged during the replication. Some of the lamellae were torn and others either heavily distorted or buckled under their own weight (Figure 5-6 b).

The round replicated pillars were characterized by white light profilometry. The features were 43.6 ± 0.3 µm for replicas of original structures of 44 µm and 14.5 ± 0.3 µm for replicated 13 µm high SU-8 structures. The heights of the original SU-8 pillars were determined from *SEM* micrographs by the supplier (*SSLS*). The average dimensions of the masters are summarized in Appendix A.).

As an alternative processing route, pillar arrays were produced by *FIB* milling.
Several 20x20 pillar array templates were milled at different writing times (30 min, 2h, 4h and 6h) in order to study the milling rate.
The complete array was replica molded with *PDMS* for estimating the milling depth. The molded structures after 30 min milling were not quantified as the feature lengths were below

the estimated error. All the *SEM* micrographs were taken at the same magnification (Figure 5-7 a- c). The height of the pillars is 2.7 µm after 2 h of milling, 4.6 µm after 4 h (Figure 5-7 b) and 6.7 µm after 6 h (Figure 5-7 c). The inclined side walls lead to conically shaped pillars. The heights were determined by multiplying the apparent lengths in the micrographs by the factor of 1.4 because the sample was tilted by 45° for better visibility.

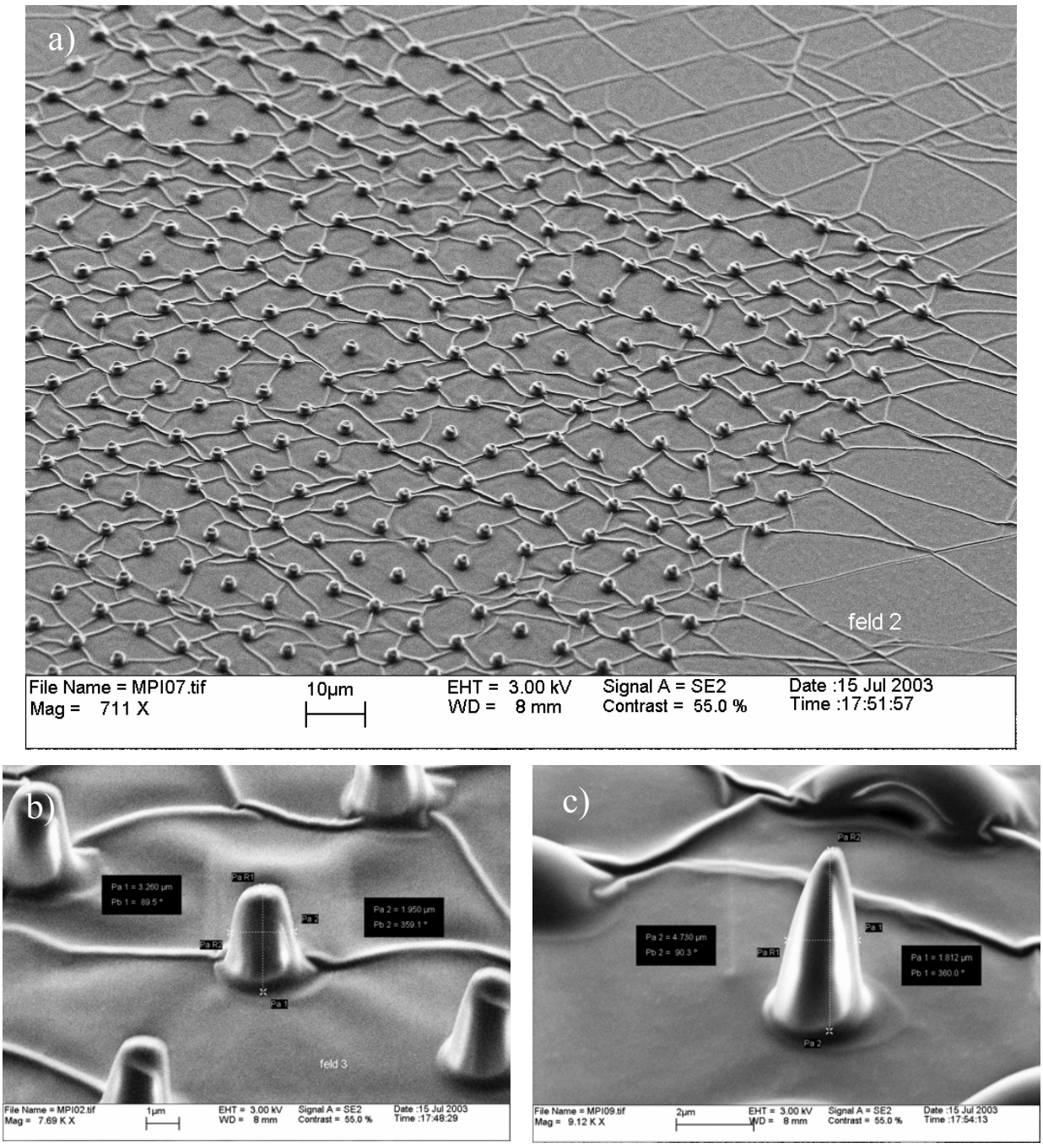

Figure 5-7: *SEM*-Micrographs of an array milled for 30 min milled for a) 30 min, b) 4h and c) 6 h [*SEM* images by J. Ulmer, dept Spatz , Heidelberg]

The depth of the milled trenches and pillar length respectively increased with the milling time (Figure 5-8) at a rate of approximately 1 µm/h for the given pattern.

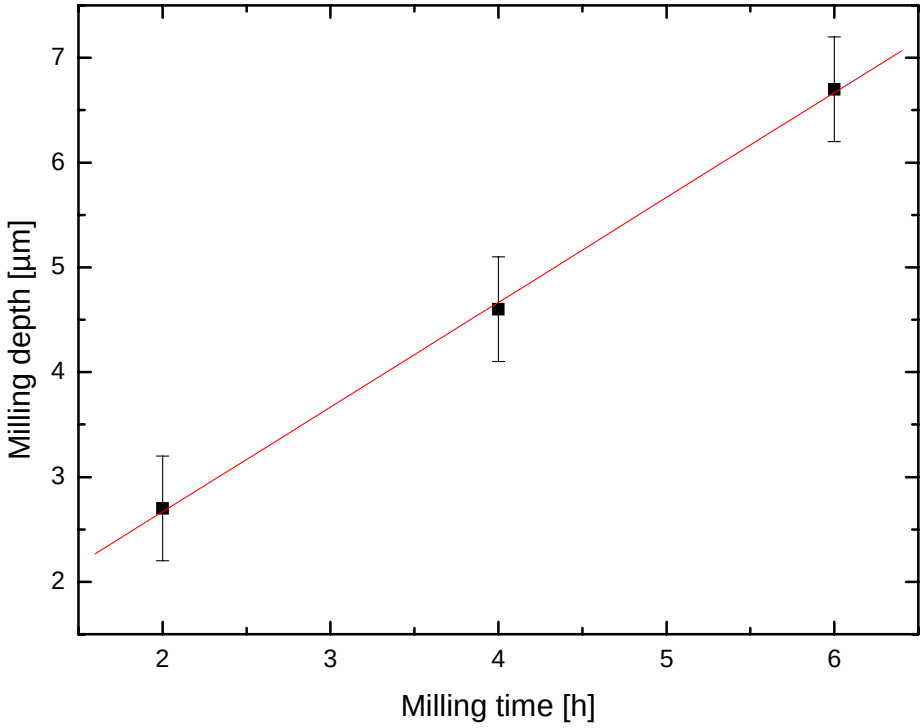

Figure 5-8: Milling depth vs. time for a 20x20 array in Silicon

The estimated observational accuracy of 0.5 µm was directly used as error for the data. The surface between the pillars bears a mesh of ridges about several hundred nanometers in diameter and spaced at several microns (Figure 5-7). The ridges appeared in samples where gold had been plasma deposited on the surface for better imaging and were not observed in non-coated specimens.

5.1.5 Molding of Electrochemically Etched Templates

Polystyrene fibrillar structures with flattened heads were obtained from a sacrificial molding process in electrochemically etched templates provided by Sven Matthias (Max Planck Institute of Microstructure Physics, Halle, department Gösele (Figure 5-9 a).

The resulting channels were 1 µm wide at a length of 10 µm. The drop-like tip ends were intentionally widened (undercut). The channel structures were replicated in Polystyrene

(PSS Mainz, lot.:ps30604, Mw= 184000) and successively relieved from the template by KOH etching.

The pillars condensed to clusters of 10-20 pillars each (Figure 5-9 b).

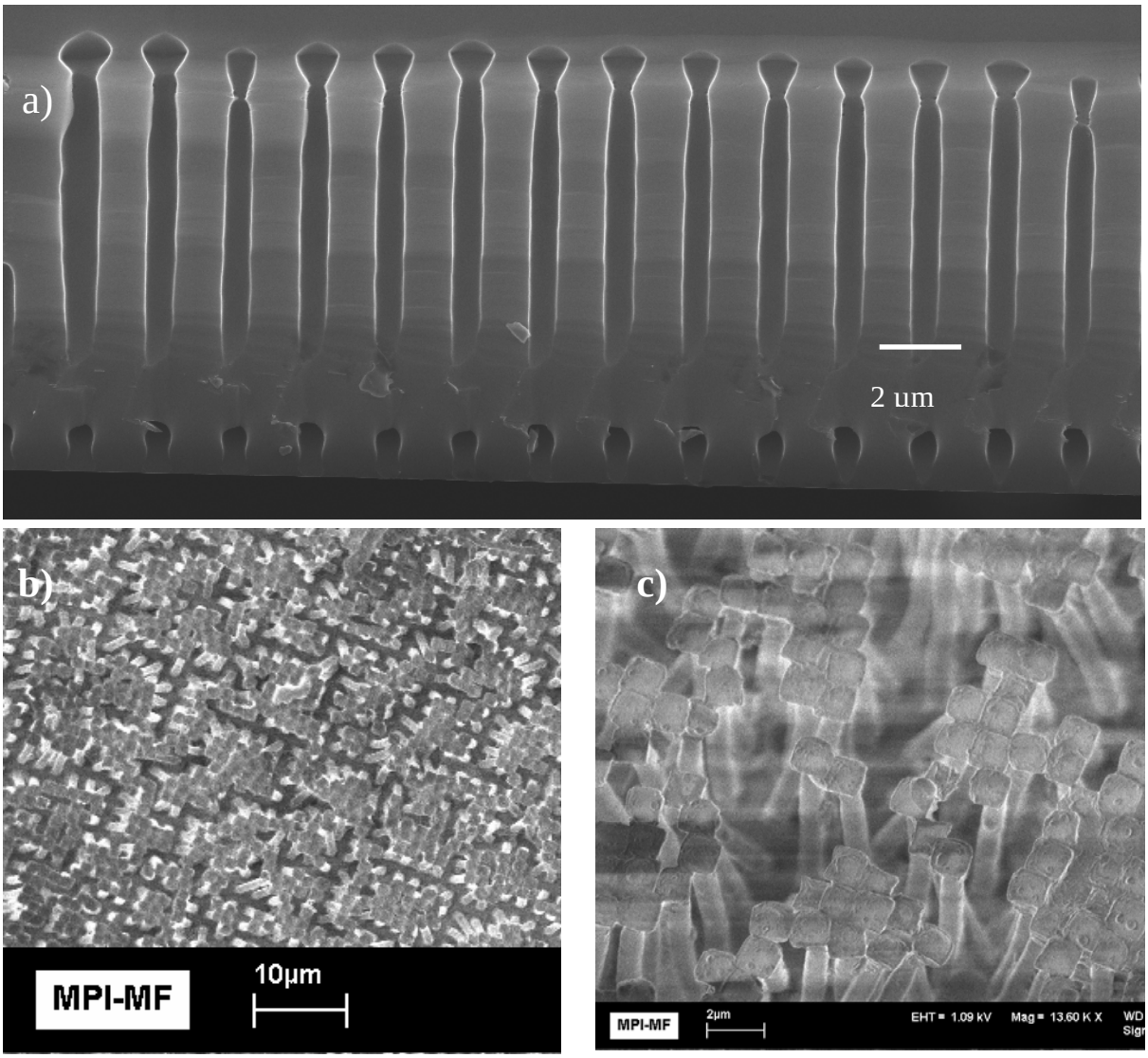

Figure 5-9: Fracture edge of an electrochemically etched silicon template wafer fabricated by Sven Matthias, Max Planck Institute of Microstructure Physics, Halle, b) Clusters of condensed undercut Polystyrene fibers, c) structures closeup: Tips sticking to each other

The contacts of the condensed pillars were formed at the flattened fibril tips (Figure 5-9 c). A straight wall electrochemically etched template was applied for molding high aspect ratio (10:1) *PDMS* fibrils. The template was silanized and not sacrificed during the process. The fibrils were set free by pulling them out of the template. The fibrils collapsed after removing them from the mold (Figure 5-10).

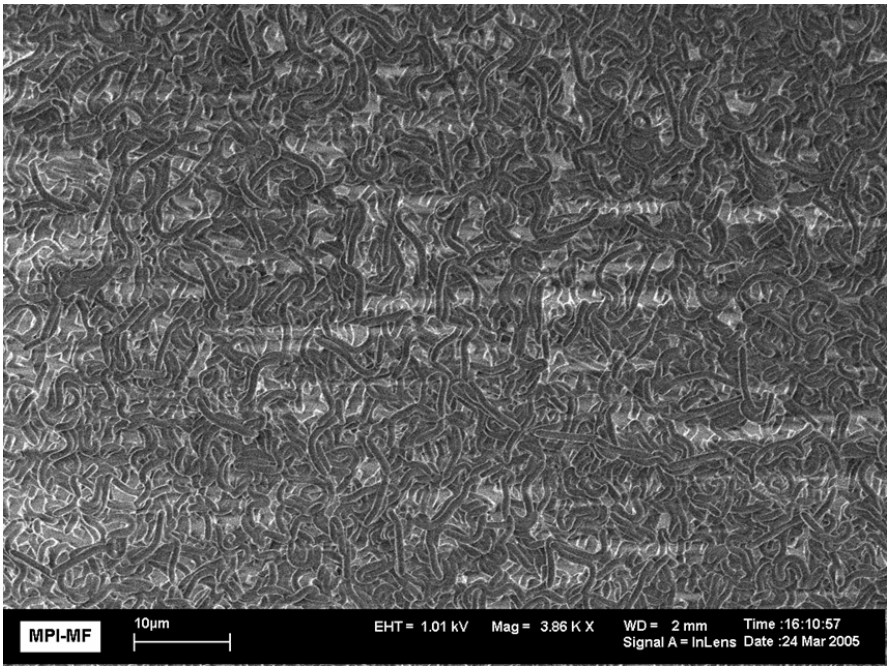

Figure 5-10: Collapsed high aspect ratio (10:1) structures in *PDMS*

5.2 Measurements on Single Contacts Nanoindenter Measurements with Rigid Contact Elements on a Polymer Substrate

In a first set of experiments, the behavior of the testing systems was characterized before conducting adhesion measurements on single contacts and on periodic fibrillar attachment arrays. The main results are summarized in the following section.

5.2.1 Adhesion Measurements at Various Retraction Velocities on Different Materials

The adhesion properties of flat *PDMS*, *PVS* and metacrylate resin specimens were measured with the Nanoindenter XP for different retraction speeds. On the polymetacrylate surface no adhesive forces were detected. The adhesion of *PDMS* and *PVS* was investigated for different retraction speeds to investigate the velocity dependence of the adhesion forces for different materials. For the adhesion tests a sapphire spherical tip (r = 250 µm) was used. Figure 5-11 plots the average pull-off forces for *PDMS* and *PVS* versus the retraction speed with statistical errors.

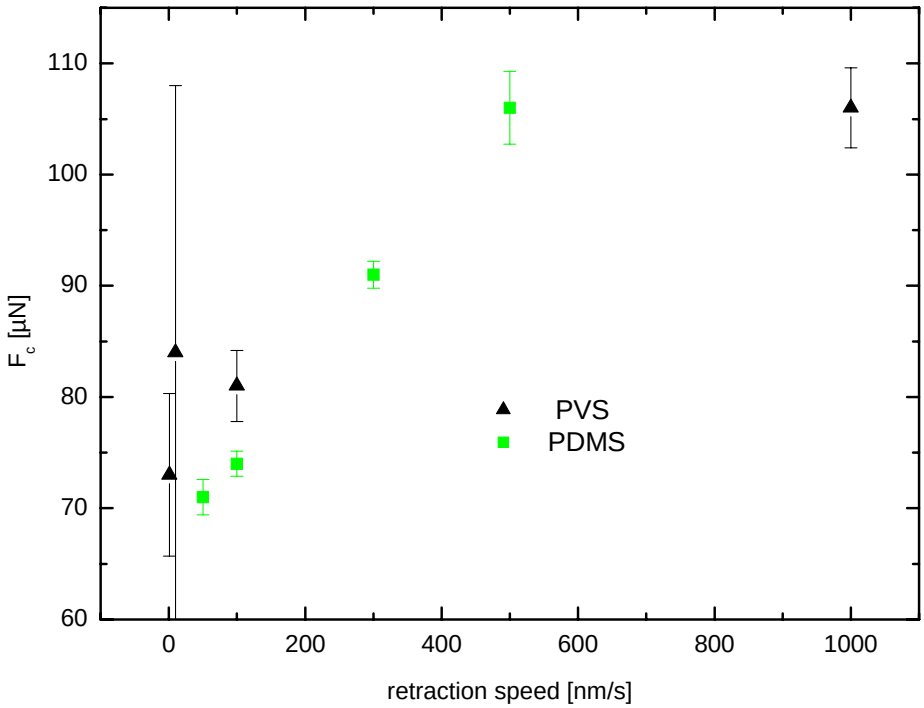

Figure 5-11: Pull-off force vs. retraction speed for a sapphire sphere (r=250µm) on flat *PDMS* and PVS

For both materials the pull-off force increases with retraction speed at different slopes.

5.2.2 Influence of the Indentation Depth on the Adhesion Force

Adhesion tests were performed with a sapphire sphere (r=150µm) on *PDMS* for different indentation depths from 100 to 3000 nm (Table 5-3).

Table 5-3: Pull-off force vs. indentation depth on *PDMS*

Indentation depth [nm]	**Mean Pull-off force [µN]**	**Error [µN]**
100	58.8	1.3
500	61.2	1.4
1000	60.9	2.0
2000	62.3	1.9
3000	61.3	2.2

5.2.3 Adhesion of Modified Contact Surfaces

Several experiments focused on determining the influence of modified surface properties on the adhesion forces.

In a first measurement the pull-off force for a sapphire sphere (r = 250 µm) on a *PDMS* surface was determined before, one minute and eight hours after the oxygen-plasma treatment. The contact angle with water was also determined. The results are plotted in Figure 5-12. Initially the *PDMS* surface generated an adhesion force of 67 µN and a 118° contact angle for water was observed. The forces decreased to 52 µN and the contact angle fell to 42° right after the plasma treatment. The contact angle reached 108° eight hours after the plasma oxidation whereas the forces did not exceed 46 µN.

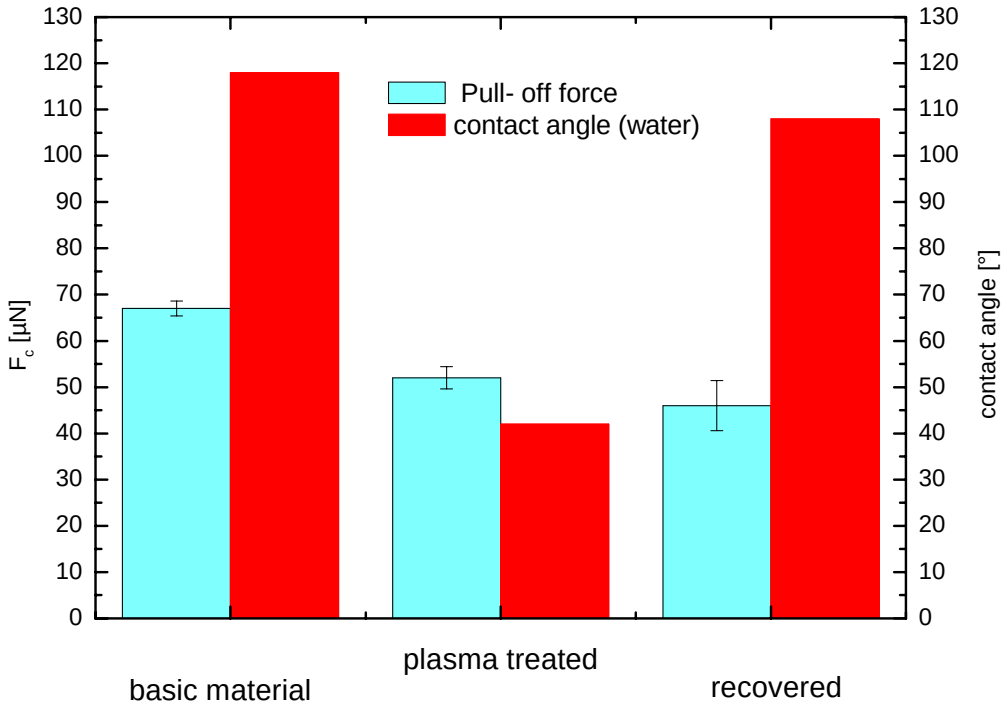

Figure 5-12: Contact angles and absolute values of the adhesion forces for a sapphire sphere (r=250µm) on a *PDMS* surface before and after oxidation in an oxygen plasma 200 W, p_{O2} = 1 mbar, p_{vac}=0.3 mbar

The sample was also characterized by light microscopy before (Figure 5-13 a) and after (Figure 5-13 b) the plasma oxidation. The applied plasma treatment generated a network of surface cracks spaced at several tens of microns.

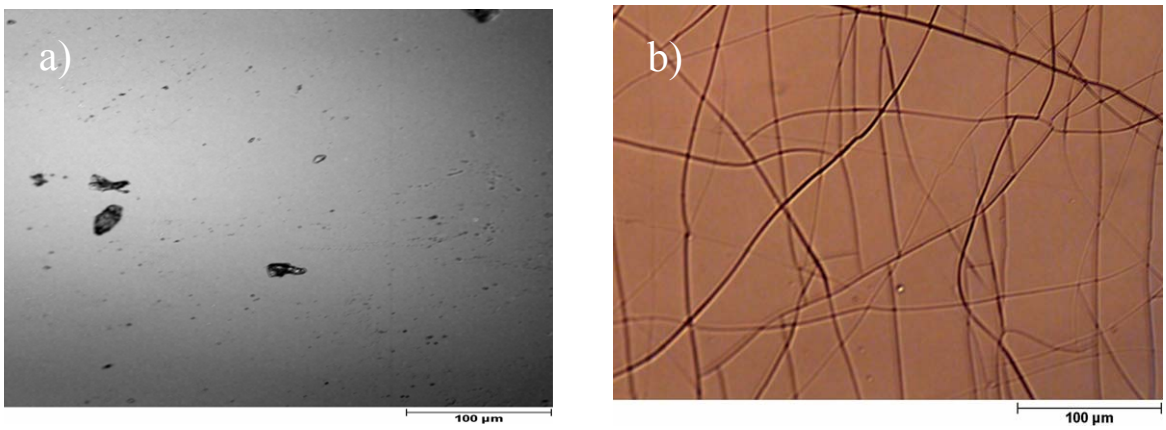

Figure 5-13: *PDMS* surface: a) before and b) after plasma treatment (200 W, p_{O2} = 1 mbar, p_{vac}=0.3 mbar, micrograph by N. Sauer)

In a second experiment with a 10 s plasma exposure, the contact angle was tracked continuously for approximately 400 min after the surface treatment (Figure 5-14). The effect of contact angle recovery on oxidized *PDMS* under ambient conditions, where the surface returns from a hydrophilic to a hydrophobic state within about 150 minutes, was observed.

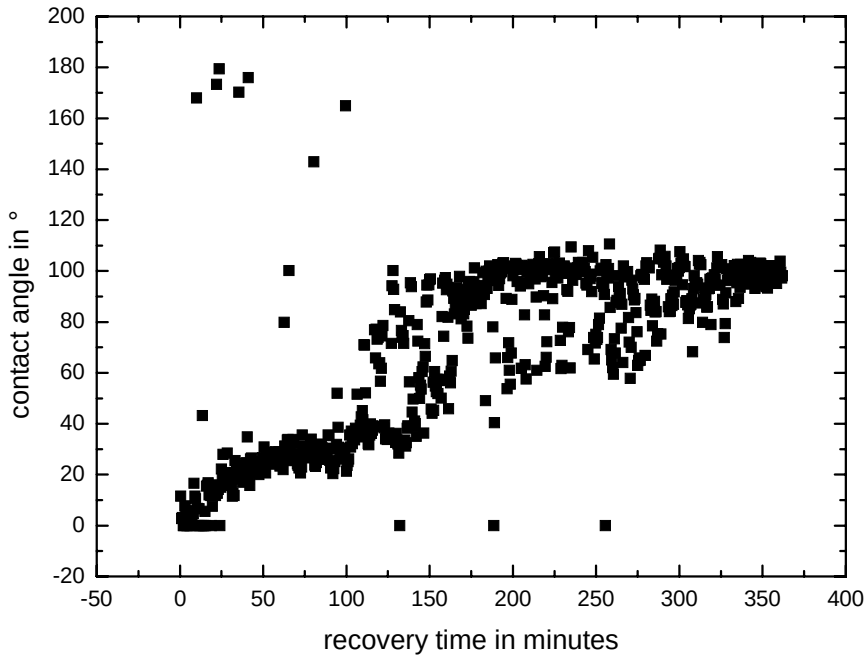

Figure 5-14: Contact angle recovery on plasma-oxidized *PDMS* under ambient conditions

The adhesion forces were measured simultaneously on a reference sample for a sapphire flat punch (r=25µm) (Figure 5-15).

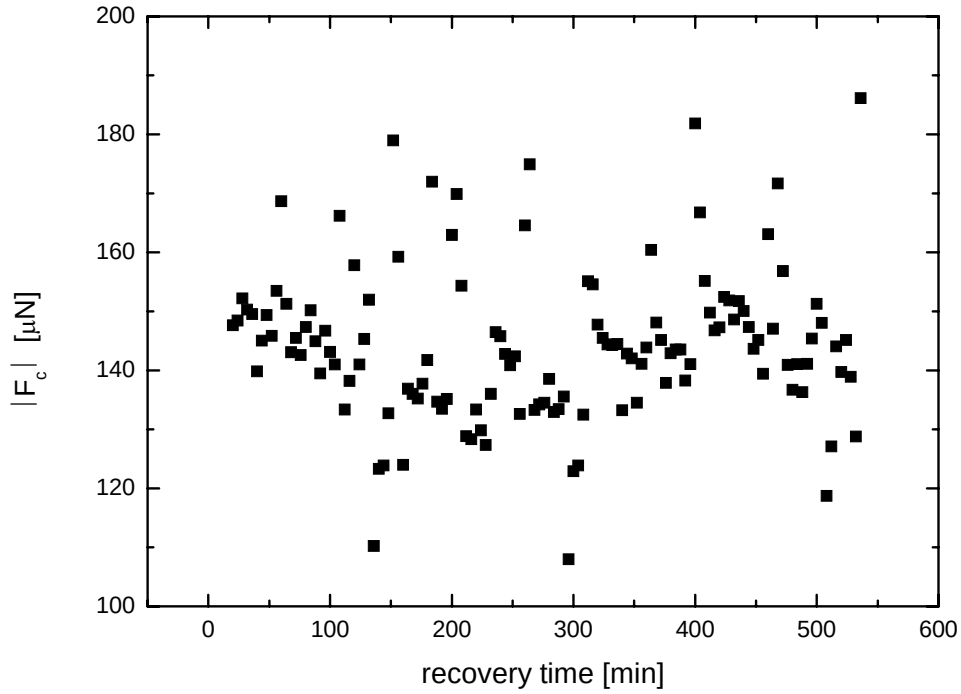

Figure 5-15: Pull-off forces during recovery on plasma-oxidized reference *PDMS* parallel to the respective contact angle measurements

The adhesion forces did not show clear changes over time during the recovery process. Another surface modification was achieved by silanizing the *PDMS* surface. The adhesion force was measured before and after depositing the fluoro-terminated polymer with a 50 µm diameter sapphire flat punch. Unexpectedly, instead of being decreased, the adhesion forces roughly doubled after the surface treatment.

Table 5-4: *PDMS* untreated and silanized

	Untreated sample	Silanized (test 1)	Silanized (test 2)
Pull-off force [µN]	90.6	216.0	140.0
Error [µN]	5.0	31.9	37.0

The material stiffness was extracted from the force distance curve. No changes were found comparing the load vs. displacement slope of the tests before and after silanization.

5.2.4 Contact Element Shape and Size

The adhesion on a *PDMS* surface was measured for variously sized sapphire flat punches and spheres. The average measured values including error bars for the statistical errors are visualized in Figure 5-16:

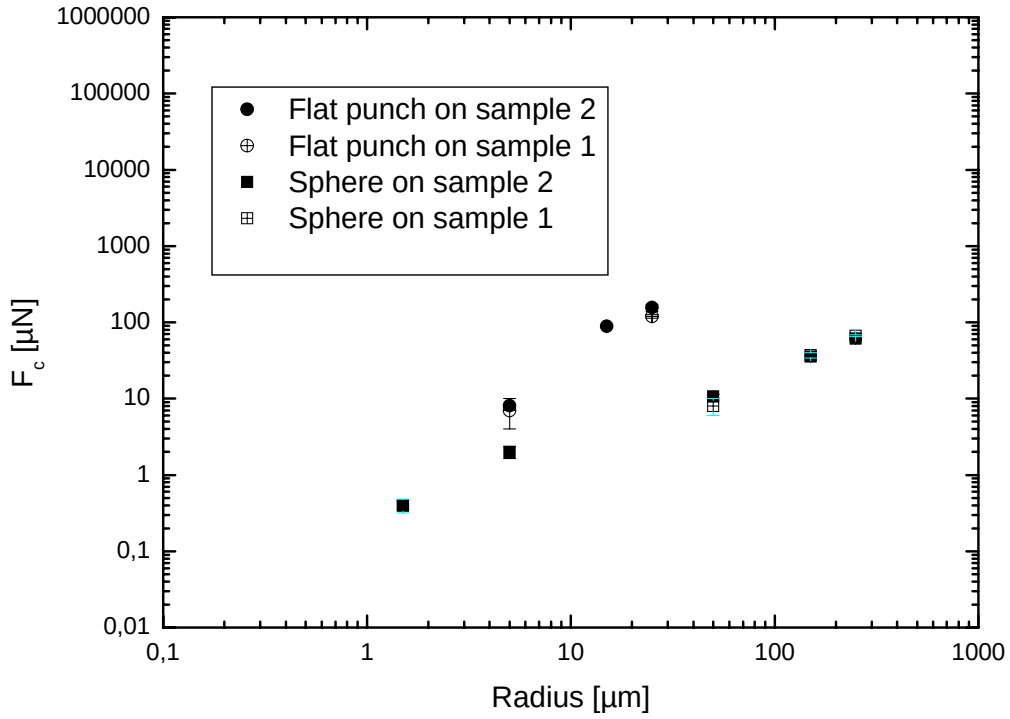

Figure 5-16: Pull-off force vs. radius for two different *PDMS* substrates 1 and 2 for flat punches and spheres

5.2.5 Measurements on Cold Imprinted Soft Contact Elements

Cold imprinted spherical *PDMS* contact elements 337 ± 28 nm high, 34 ± 1 µm wide and with a radius of curvature of 334 ± 23 µm on average were tested for adhesion with a flat punch sapphire indenter (r = 25 µm) and a sapphire sphere (r = 250µm). The adhesion forces did not differ significantly for measurements on the contact elements and on the flat reference material (Table 5-5).

Table 5-5: Pull-off force on *PDMS* contact elements and flat reference material for a sapphire spherical indenter (r = 250 µm) and a flat punch (r = 25 µm)

Mean pull-off force [µN]	**spherical tip (r = 250µm)**	**punch tip (r = 25 µm)**
Reference material	65.8 ± 6,5	149.0 ± 3,6
Spherical contact element	60.9 ± 3,6	148.3 ± 2,5

5.3 Measurements on Arrays of Biomimetic Contacts

5.3.1 Arrays of *PDMS* Pillars

Adhesion measurements on fibrillar *PDMS* structures 5 µm wide covering 20 % of the overall surface were performed with a sapphire sphere indenter 1500 µm in radius. The adhesion data are visualized in a histogram (Figure 5-17). The histogram gives a wide range of pull-off force values with a distinct maximum of about 80 µN.

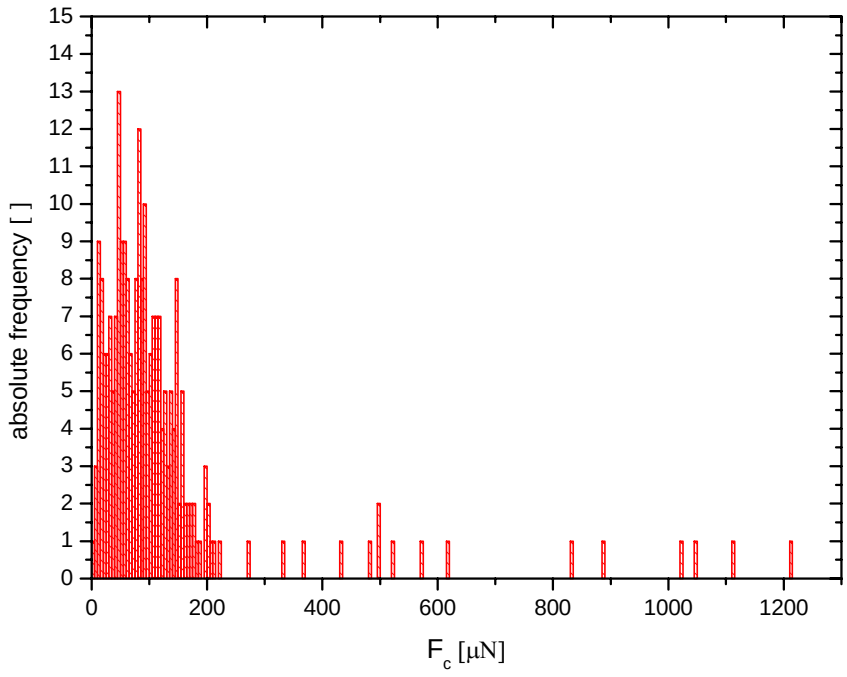

Figure 5-17: Absolute Frequency of measured pull-off values for *PDMS* pillar structures measured by the BASALT I tribometer

In some measurements pull-off forces as high as 1200 µN were observed. The latter corresponded to specimens bearing damaged pillar structures (Figure 5-20 a).

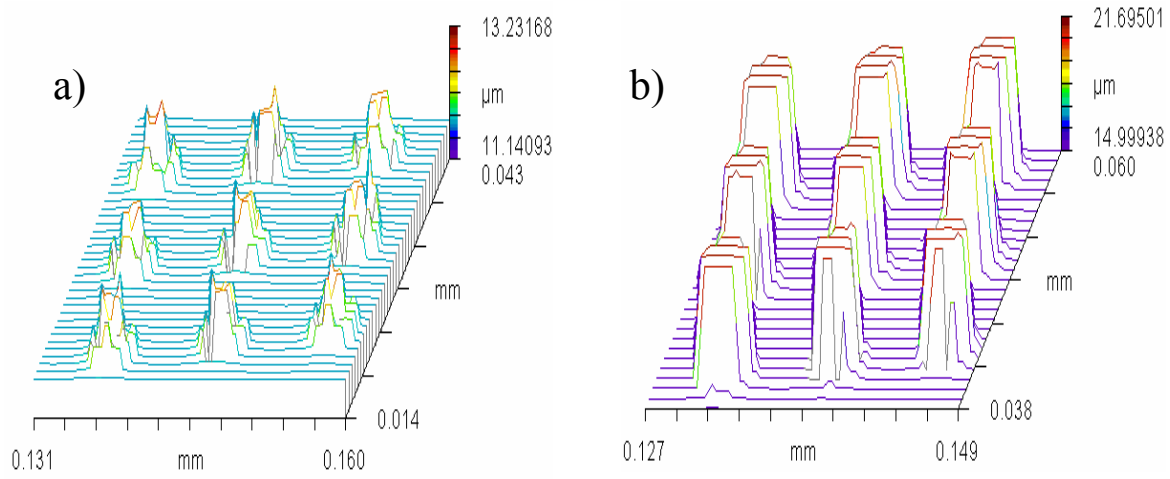

Figure 5-18: White light profiles of structures with a) high and b) low adhesion

Nanoindenter XP adhesion tests were applied for a second set of photo lithographically fabricated samples. Again, the *PDMS* pillars (Sylgard 184 Dow Corning) were 5 µm wide, spaced at 10 µm from center point to center point with an areal density of 20 %. The 16 µm high pillars were loaded to an indentation depth of about 3 µm with a flat punch 50 µm and a sphere 300 µm in diameter. As seen by light microscopy (Figure 5-19), the pillars did not suffer irreversible deformations or condensation during the measurements.

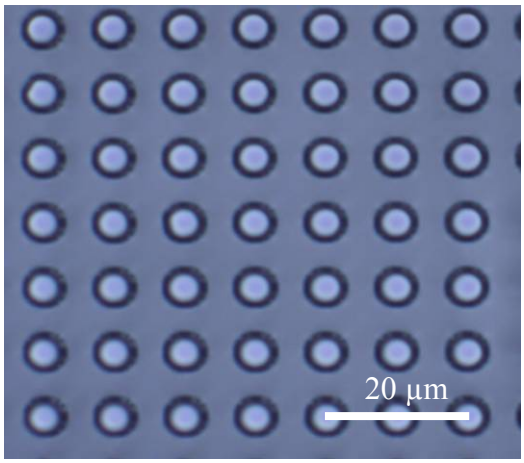

Figure 5-19: Fibrillar structure unchanged by shallow indentation

Figure 5-20 shows a typical force-displacement curve, as obtained for fibrillar *PDMS* surfaces. The curve of the loading and unloading cycle is not as smooth as for flat *PDMS* (Figure 3-17) and contains several distinct single event force jumps in the pull-off regime.
In contrast to low indentation depth tests, the pillars on the edge of the punch condensed during a parameter adjustment test (Figure 5-21) and during deep indentation experiments. The micrograph shows a 5x5 array of deep indents.
After testing a 5x5 indent array, fiber condensation was observed at the indent edge (Figure 5-21). The respective samples were indented to a depth of 20 to 30 µm.

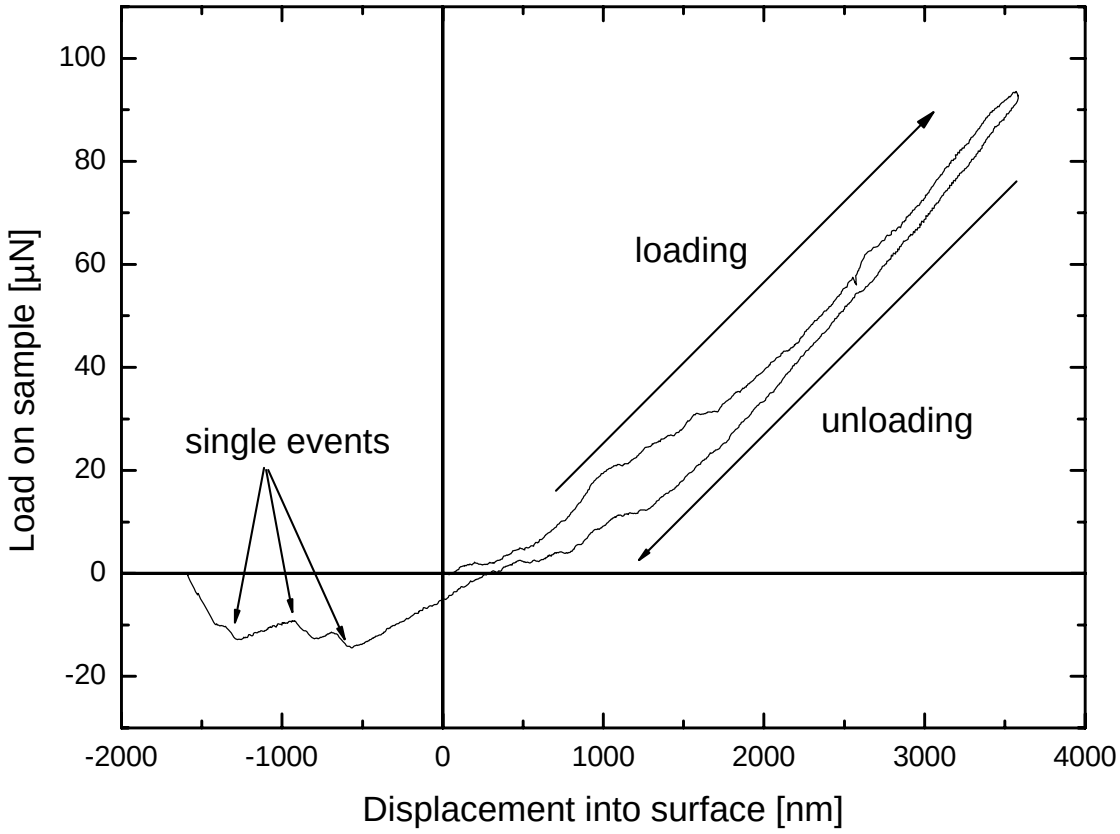

Figure 5-20: Force-displacement curve for an adhesion test on a fibrillar *PDMS* structure with single events in the pull-off peak

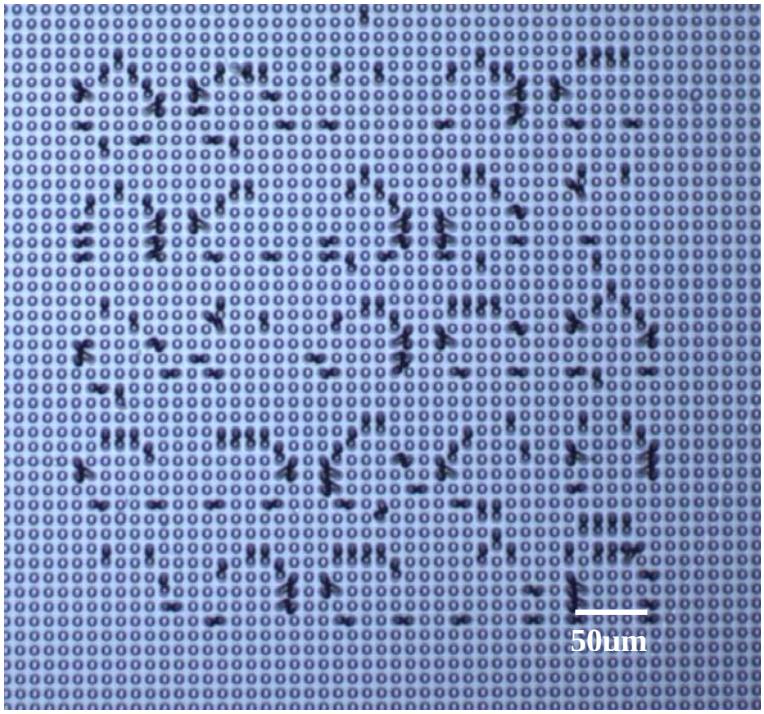

Figure 5-21: Array of 5x5 deep indents on a fibrillar *PDMS* structure; ring shaped condensation of pillars at the indenter tip edge

When indenting 16 µm long and 5µm wide *PDMS* pillars to about 15 µm depth, specific force-distance curves were obtained (Figure 5-22).

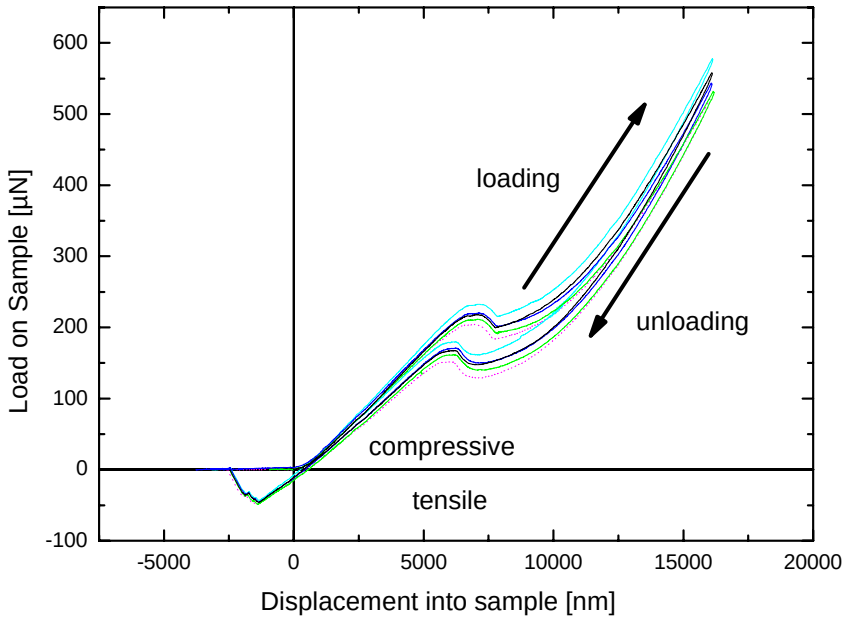

Figure 5-22: Adhesion curve for a buckling *PDMS* pillar structure

In loading the sample, a break-down in force is observed at approximately 7µm indentation depth at a corresponding force of about 200 µN. This event is very likely due to elastic buckling of the pillars. The force reaches a plateau value and successively increases again after about 1 µm. During unloading, a force peak is found at a depth of approximately 6 µm. After unloading to zero displacement, forces turn tensile and finally become zero. The force peaks correspond to peaks in the load vs. displacement curve, leading to two further signals on this channel (see Appendix C, Figure 9-5) which requires a specific testing method for such experiments.

The adhesion was also measured on a flat reference *PDMS* surface in the vicinity of the structures, thus providing the same material history for the structure and the reference.

Shallow and deep indents on flat and structured *PDMS* for a sapphire flat punch tip 50 µm wide (Table 5-6) and for a spherical spherical tip 150µm in diameter (Table 5-7) were performed on the Nanoindenter XP.

Table 5-6: Adhesion of a flat sapphire punch r= 25 µm

	Shallow Test 1	Shallow Test 2	Deep Indent	Reference flat
mean pull-off force [µN]	57.3	51.7	46.9	161.4
standard deviation [µN]	9.6	1.8	2.4	0.6
mean max. load [µN]	55.8	61.7	546.7	83.7
standard deviation [µN]	8.3	24.2	22.3	0.7
mean max. penetration [nm]	1637.7	1977.5	16091.9	1004.2
standard deviation [nm]	261.2	633.0	49.3	2.0
number of tests	6	7	7	25

Table 5-7: Adhesion of a sapphire hemisphere r= 150 µm

	Shallow Indent	Deeper Indent	Flat reference
mean pull-off force [µN]	22.0	16.2	42.3
Standard deviation	6.7	6.7	0.9
mean max. load [µN]	75.6	127.1	32.2
Standard deviation	28.9	43.1	1.6
mean max. penetration [nm]	3639.2	4855.1	1010.7
Standard deviation	728.1	781.0	9.9
Number of test	18	19	12

5.3.2 Adhesion Tests on Arrays of Synchrotron-Photolithographically Fabricated SU-8 Specimens

For investigations on stiffer structures Su-8 specimens were fabricated by synchrotron lithography. After measuring no adhesion forces for two arrays of square shaped pillars with edge lengths of 2 and 5 µm spaced at lattice parameters of 4 and 10 µm, a reference test was conducted on the flat material aside the structures. According to *SEM* micrographs, the polymer surface was very rough with ridges of several tens to a few hundred nm in diameter (Figure 5-23).

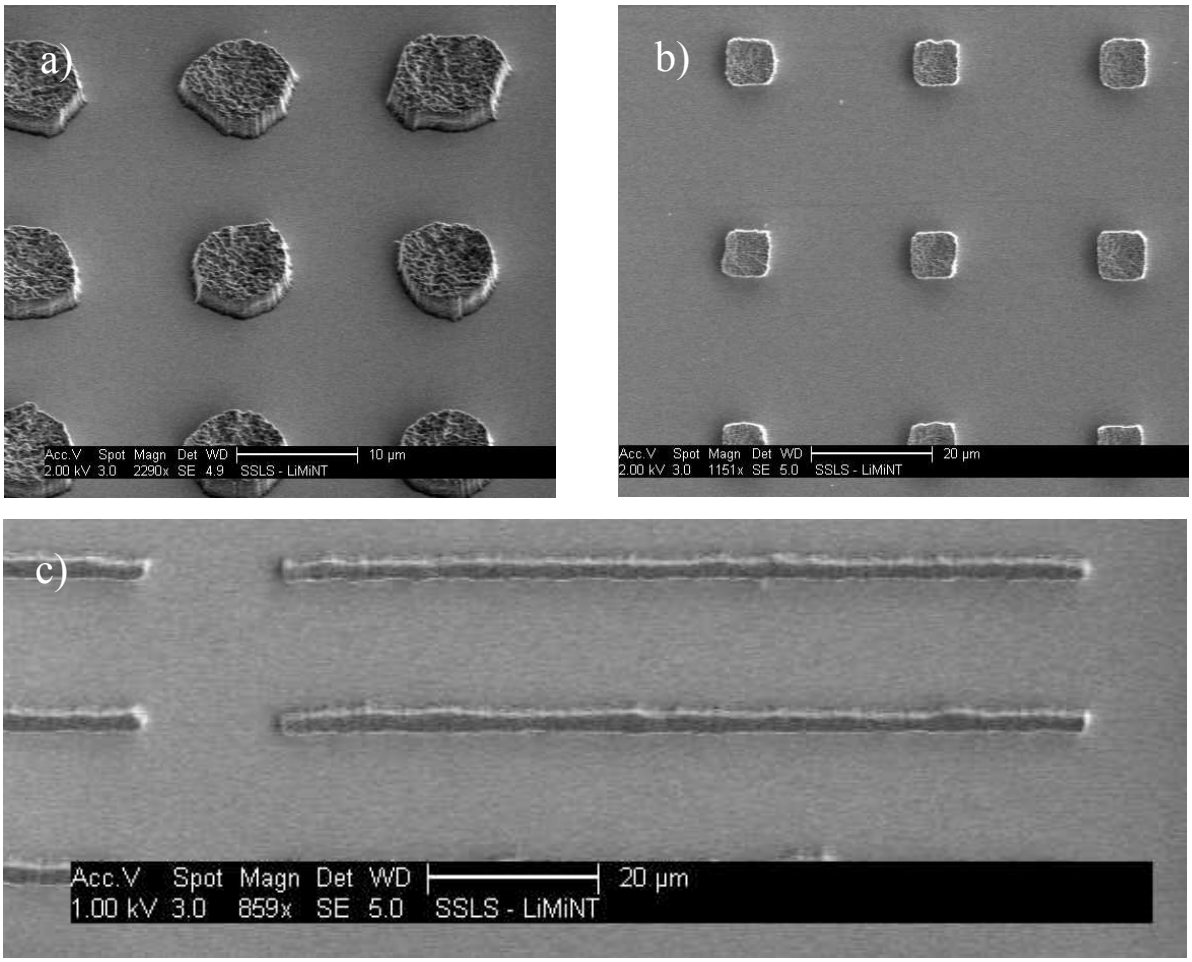

Figure 5-23: *SEM* micrographs of selected SU-8 structures: Circular a) r= 5 µm; b) square, edge length = 10 µm; c) rectangular, length l= 100 µm, width 5 µm

Measurements on the recently built successor of Basalt I (Basalt II) were performed with a sapphire tip (r = 1.5 mm) on pillars 17 µm wide and spaced 35 µm. Assuming a force error of 1 µN, the average pull-off force was 7.9 ± 1 µN corresponding to an average work of adhesion γ of 1.1 ± 0.1 mJ/m² according to *JKR* (see equation (2-11) for fixed load conditions).

6 Discussion

6.1 Fabrication of Artificial Bioinspired Contact Elements

Two classes of micro structuring processes were explored in the present work. The first aimed at single elements or clusters of micro contacts with predefined shapes, whereas the second generated fibrillar structures without specified tip geometries. More complex structures were fabricated by method combinations.

6.1.1 Predefined Contact Element Shapes

Cold imprinting has been demonstrated as a fast and straightforward processing route for contact elements with predefined shapes. As the first prototypes were imprinted into aluminium, the indentation depth and thus the resulting feature height of the polymer cast were limited to a few hundred nanometers by the instrument maximum load. For longer contact elements a softer material with lower yield strength is recommendable. Cold imprinting with a nanoindenter provides a variety of shapes and sizes of the indents. Besides, the regular indenter tips can be modified by *FIB* milling or other micro structuring techniques to obtain very specifically shaped indents. The imprinted molds are not accurately predefined, as the indenter size is not transferred to the substrate 1:1. As qualitatively described by Oliver and Pharr, [62] the indent has a slightly larger radius for spherical indenters and an increased included tip angle for conical indenters. Nevertheless the method is adequate for the production of specific micro contacts as the shapes remain and the contact elements are well characterizable by interferometry or *AFM*. Imprinting provided a fast mold production method for available tip geometries. Compared with the *AFM* indentation method proposed by Sitti *et al.* [61], shape and size can be chosen more freely at a wider size range.

Alternatively to cold imprinting diverse predefined contact element shapes were achieved by *FIB* milling. The *FIB* is suitable for milling specific micro molds as well as for cutting rigid indenters. Being a sequential method, only writing a microscopic spot of the ion beam diameter at a time, the method is limited to small sample areas in the range of several hundred micrometers in square due to time consumption. When time is not an issue, large areas are possible by shifting the stage to the adjacent position and remilling (stitching). *FIB* milling is

suitable only for structuring volumes directly accessible by the beam. Thus no undercut structures are directly obtained. The milled shape again may differ from the blueprint as the beam has a Gaussian intensity profile that is always superimposed onto the calculated shapes, being problematic for high aspect ratios. The problem could be solved by an additional milling step with a finer ion beam, but was not investigated. Also, the inclination of the surface and the aspect ratio of cut trenches are crucial to the milling and redeposition rate and thus influence the shape and size of the trenches. As these factors are not easily predicted by calculations, no effort was made to fully correct such effects by calculations. Some correction parameters have been implemented in the pattern calculation software to provide a tool for optimizing the milling results. The milled geometries generally are in good agreement with the predefined shapes. A great advantage of the method is the high degree of automation, the possibility to remill shapes at different locations and high flexibility concerning the size and shape of the structure. For writing times exceeding 30 minutes, it is recommendable to use a drift correction tool to compensate the beam drift. Otherwise the drift may result in distorted (Figure 3-6) and asymmetric (Figure 5-1d) shapes. To our knowledge, the *FIB* milling technique has been used for a first time to fabricate specifically shaped micro contact elements.

6.1.2 X-Ray Lithography

X-Ray lithography provides a flexible tool for fabricating straight walled fibrillar microstructures on centimeter scale specimens. Inclined structures are obtained by orienting the sample in an adequate angle to the synchrotron beam. The high brilliance of synchrotron radiation enables the production of aspect ratios of 50:1 and above. No tip shape control is possible in X-ray lithography in a single step process. The SU-8 photoresist structures were significantly rough in the tens to hundreds nanometer regime. As the material was relatively stiff compared to the *PDMS* polymer, substrate roughness was not easily compensated by deformation of the material thus resulting in low adhesion forces. By replica molding, the structures were successfully transferred into a softer material for improving the adhesion properties. Adhesion measurements have not been performed and are subject of future experiments.

6.1.3 Photolithography

Photolithography with subsequent micromolding is a well installed standard method for fabricating micrometer sized pillar structures. Although not providing tip shape control, the method was sufficient to investigate the collective attachment and detachment behavior of fibrillar adhesion structures. The aspect attainable aspect ratios were somehow limited to about ten, as the exposing light underwent refraction, diffraction and absorption in the photo resist material. The structure boundaries therefore were more diffuse than for X-ray lithography and the lateral resolution for the standard process was limited by the wavelength of the applied light. The method was well applicable for features in the range of several micrometers.

6.1.4 Electrochemical Etching

Electrochemical etching is well suitable for the fabrication of straight walled structures as well as for undercut shapes with well defined geometries. The specimen areas accessible are given by the photolithographic prestructuring process available for all standard wafer sizes in microelectronics. Feature diameters of several µm are fabricated in silicon whereas alumina provides a material for self-assembled parallel pores in the range of hundreds of nanometers [66, 84]. As the templates have to be dissolved to set the cast polymer structures free, the sacrificial process is a one-way- process not suitable for mass fabrication. Nevertheless it may be beneficial when highly specific small attachment devices (e.g. tips for micromanipulators) have to be produced. Melt casting leads to hollow polymer tubes instead of bulk pillars. The stability of these structures is possibly increased by generating a composite when filling the tubes with another polymer material as discussed with Dr. M. Steinhart (MPI of Microstructure Physics, Halle). This fabrication method for the molds was tested in first experiments but was not investigated in detail. Recently, respective sub-micron fibrillar attachment specimens were demonstrated by Jin *et al.* [84].
Although matching the feature size of gecko hairs, the prototypes cast in porous alumina are less suitable for precise mechanistic studies than the micrometer structures with predefined positions in silicon due to the random positions of the fibers. Still they are sufficient for testing adhesion of artificial nanometer scale bioinspired attachment devices.

6.2 Adhesion Forces in Single Contacts

6.2.1 Influence of Indentation Depth and Unloading Speed

As the exact penetration depth in adhesion measurements depends on the surface detection accuracy, the influence of indentation depth on the adhesion forces was determined. The measurements on flat material were performed for a range of indentation depths of up to 3000 nm, hence well exceeding the span of any encountered surface detection height errors. No significant change in adhesion was observed for flat specimens (Figure 6-1, data from Table 5-3). Considering the statistical errors, the adhesion force stayed constant within a penetration depth range from 100 to 3000 nm. This result was expected for experiments within the restriction of small deformations and fully elastic behavior. Nevertheless, any experiments on the material adhesion properties should be conducted at uniform indentation depth to grant the comparability of results.

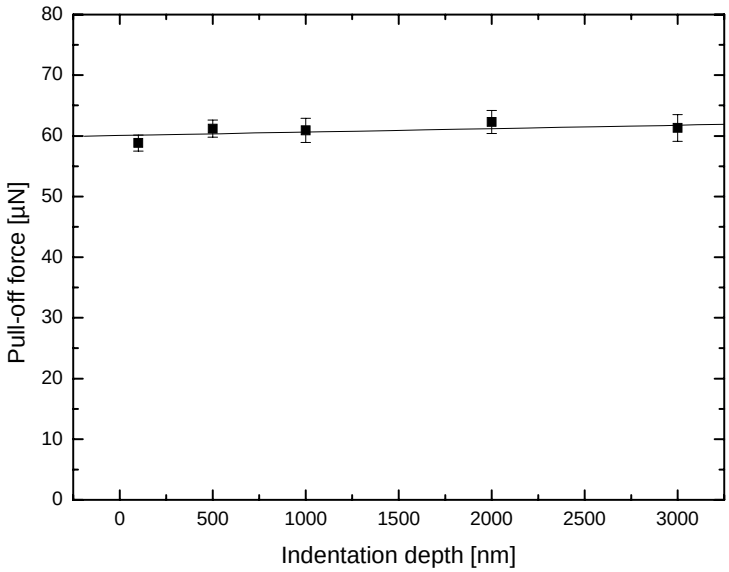

Figure 6-1: Pull-off forces for a sapphire sphere (r=250µm) against *PDMS* at various indentation depths

Adhesion forces could be changed due to energy dissipation (e.g. viscoelastic losses) and plastic deformation of the material in contact. Within the applied range, no such effects were observed.

In contrast, retraction speed plays a crucial role for adhesion. The retraction velocity dependency was measured for *PDMS* and PVS (Figure 6-2, data from Figure 5-11). As the pull-off forces increase with the retraction velocities, adhesion tests have to be performed at

identical retraction speeds for comparability. The adhesion force vs. retraction velocity curve also provides the necessary information for extrapolating the forces and work of adhesion for the quasistatic case. The data was fitted with an exponential approach by Maugis and Barquins [35]. According to equation (2-16) the velocity dependent increase of the work of adhesion is proportional to the viscoelasticity function φ.

The dissipation function $\varphi(a_t v)$ for rigid spheres on rubber like material is often proportional to $(a_t v)^{0.6}$ [35, 85], where a_t is the WLT- shift factor and v the crack velocity see section (see section 2.2.2). The exponent may range between 0.1 and 0.8 [86]. A non-linear curve fit was performed according to

$$F_c(v) = (m_1 v)^{0.6} + F_c^0 \qquad (6\text{-}1)$$

where m is a fitting parameter and F_c^0 the fitted pull-off force for zero speed (Figure 6-2). The crack velocity v is considered proportional to the driving velocity, which is a simplification [42]. The extrapolated quasistatic pull-off force value is 76.2 ± 3.4 µN for PVS and 63.29 ± 1.0 µN for *PDMS*. For increased fitting accuracy the exponent was set to 0.8 for the *PDMS* data. Hence the behavior for *PDMS* is almost linear. The fits for the *PDMS* and PVS data were compared quantitatively according to the χ^2- value as a measure for the fit quality. The regression function for the *PDMS* curve is sufficient with a χ^2 per degree of freedom value of 1.13 whereas the PVS fit is much worse at a value of 27.8. This is a consequence of the relatively large statistical errors for the PVS measurements. As the highly viscous components of the polymer cannot be mixed as homogeneously as the *PDMS* material the wider spread of data could result from material inhomogenieties.

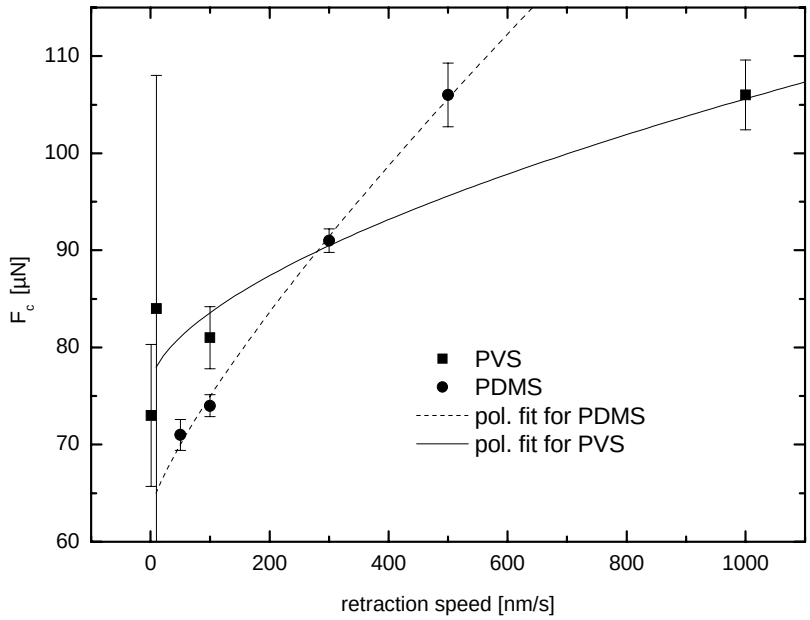

Figure 6-2: Pull-off force vs. retraction speed for a sapphire sphere (r=250µm) on *PDMS* and PVS

Therefore, knowledge of retraction speed is essential to provide comparability between different measurements. The viscoelastic properties as such were not in focus of the present work. For a deeper understanding of adhesion tests on viscoelastic materials the reader is referred to the literature [36, 37, 39]. An approximate method for fitting adhesion data of viscoelastic materials has been provided by Barthel *et al.* [41, 42].
The observed behavior of *PDMS Sylgard 184* is intriguing, as the material is commonly considered purely elastic [87]. As viscoelasticity in polymers commonly occurs due to local gliding of polymer chains, it is a property depending on the intermolecular cross-linking possibly varying in individual *PDMS* samples.

Viscoelasticity may well have significance for biological attachment systems. As the detachment during locomotion takes place within milliseconds [44], and as the material within the gecko nano contacts is accelerated and decelerated, the adhesion forces could be massively increased in certain critical situations (e.g. stop from falling). Adhesion is not increased infinitely with higher speeds [36]. As in any dissipation process, there is a maximum for energy dissipation, and for the pull-off force, which depends on the ratio between loading or unloading times and material specific relaxation times. The appropriate choice of material for a specific detachment speed may thus improve the performance of a biomimetic attachment system.

6.2.2 Surface Properties

According to contact theory, the surface energy of the contacting bodies should influence the adhesion. This influence can be accessed by surface modification without changing the sample bulk properties. By plasma oxidation the surface of *PDMS* was changed from hydrophobic to hydrophilic. As this surface modification is reversible and the hydrophobicity recovered with time, the adhesion and contact angle were tracked during the recovery. Although the contact angle increased continuously, no effect on the adhesion force was observed (Figure 5-15). This effect was also found experimentally for gecko attachment [2] measured on the macro scale. According to the authors the polarizability plays a dominant role compared to the hydrophobicity. Huber *et al.* proved that capillary effects due to ambient humidity enhance adhesion of the nanoscale gecko spatulae [14]. For the micron scale structures in the present study, ambient humidity did not show a significant effect. First of all the experiments were conducted in an isolated chamber in an air- conditioned laboratory, thus being exposed to little changes in ambient humidity of 5% at maximum. Test series on a sample were completed within a day or two to ensure similar ambient conditions. For tests running over two days, a test series of the previous day was reproduced to ensure comparability. The effects may be less critical than for the submicroscopic spatulae in the studies of Huber *et al.*, as larger micron scale menisci, necessary for a similar enhancement of adhesion, are more difficult to form.

Under more extensive plasma oxidation, a permanent reduction in adhesion force was observed. This effect is easily explained by surface roughening due to the plasma treatment [88]. Such roughness effects are well described in literature. The evolving surface ridges are about 500 nm in height, well corresponding with a critical scale for adhesion [47].

In a further experiment, the surface was modified by applying a perfluoro-polymer layer to *PDMS* (see section 3.1.3). Although the modification is commonly applied to reduce surface stiction due to a fluoro-terminated surface, similar to a Teflon ™ coating, the measured adhesion forces with a flat punch (Table 5-4) well exceeded that of the untreated reference by a factor of 2.5. A reproduction measurement three day after the first test yielded a force still exceeding the adhesion of the untreated specimen by a factor of about 1.5. Similar results were observed by Northen *et al.* [65]. The authors tried to explain the results by a diameter increase due to the silane layer and a not specified change in the surface composition.

In our experiments, the silane layer was stabilized by a thermal treatment at 90°C which could also have changed the mechanical properties of the *PDMS*. According to contact mechanics, a doubling of the adhesion force of a flat punch on the substrate could only be reached by increasing the stiffness by a factor of 4. Analyzing the force– displacement data, no change in material stiffness was observed.
Possibly the increased adhesion force may be explained by the friction properties of CF_3-terminated surfaces. Kim *et al.* [89] demonstrated that the friction for fluoro-terminated surfaces were increased by a factor three compared to the hydro-terminated reference.

The common contact mechanics models consider frictionless contacts. The influence of friction on adhesion was modeled by Yang et al [90]. Unfortunately the model only accounts for full friction without any relative movement parallel to the counter surface and the classical frictionless contact. The authors propose to extrapolate the force values for intermediate friction. This view neglects the dissipation of energy which occurs when two surfaces slide on each other. Similarly as in the viscoelastic models, where drag forces slow down the contact edge during detachment, thus leading to increased pull-off forces, friction forces could generate a similar effect. They should be accounted for in an additive force term. The result nevertheless is puzzling and more detailed experiments and modeling are necessary. A better understanding could possibly also be achieved by investigating changes in surface morphology by *AFM* or *SEM*.

6.2.3 Scaling

The theoretical scaling behavior of diversely shaped contacts was modelled by Spolenak *et al.* [5]. The scaling properties were visualized by plotting the pull-off forces vs. the contact element radius in a double-logarithmic scale (Figure 6-3).

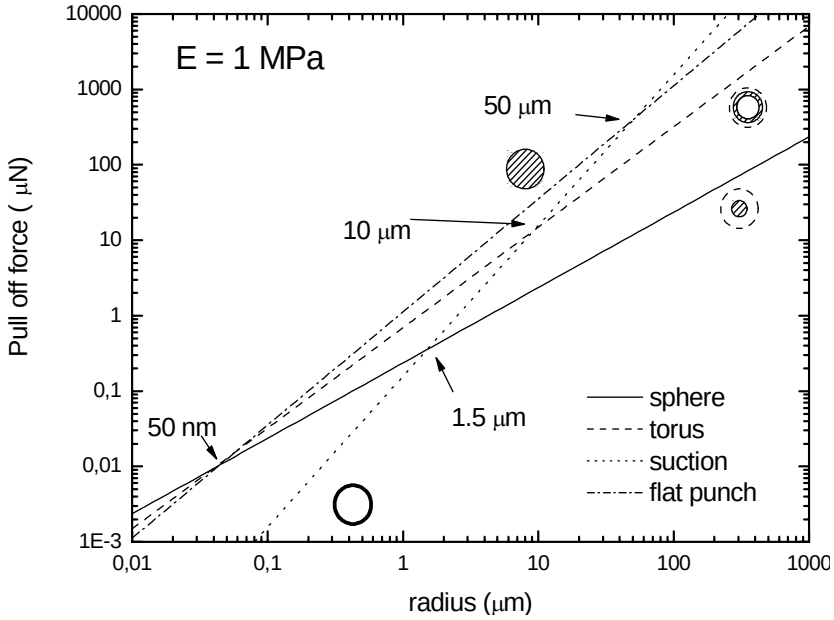

Figure 6-3: Theoretical scaling curve for pull-off forces in single contacts vs. contact radius (Spolenak *et al.* [5]), for E^* = 1 MPa, γ = 50 mJm^{-2}, $r = R/10$, p = 50 kPa.

In the present study, the scaling behavior was investigated experimentally by using rigid punch and spherical indenters of different sizes to test the adhesion of a flat *PDMS* surface (Figure 6-4, data from Figure 5-16).

The predicted slopes for the scaling curves match the experimental data well. The work of adhesion γ=77 µN was calculated according to *JKR* from the test with a sapphire hemisphere (r=250µm). The work of adhesion was used as fitting parameter for the scaling curves. The stiffness for the flat punch curve was determined by fitting the force-distance curves of the measurements with a spherical tip r = 150µm with a *JKR* fitting model for the loading segment of the curves. A reduced modulus *E** of 3.5 MPa was obtained. Using Poisson's ratio of 0.5 for the quasi incompressible *PDMS*, a Young's modulus of 360 GPa and a Poisson ratio of about 0.25 for the Sapphire indenter, a stiffness of about 2.5 MPa is obtained for the *PDMS*, which is consistent with tensile measurements on fully cured *PDMS* giving a value of 2.4 MPa [91]. The fitted curve is easily shifted to match the experimental data by reducing the effective stiffness of the *PDMS* to 1 MPa (dotted line). As the measured stiffness is considered reliable, alternatively the experimental results would be matched by changing the work of adhesion to a value of 35 mJ/m².

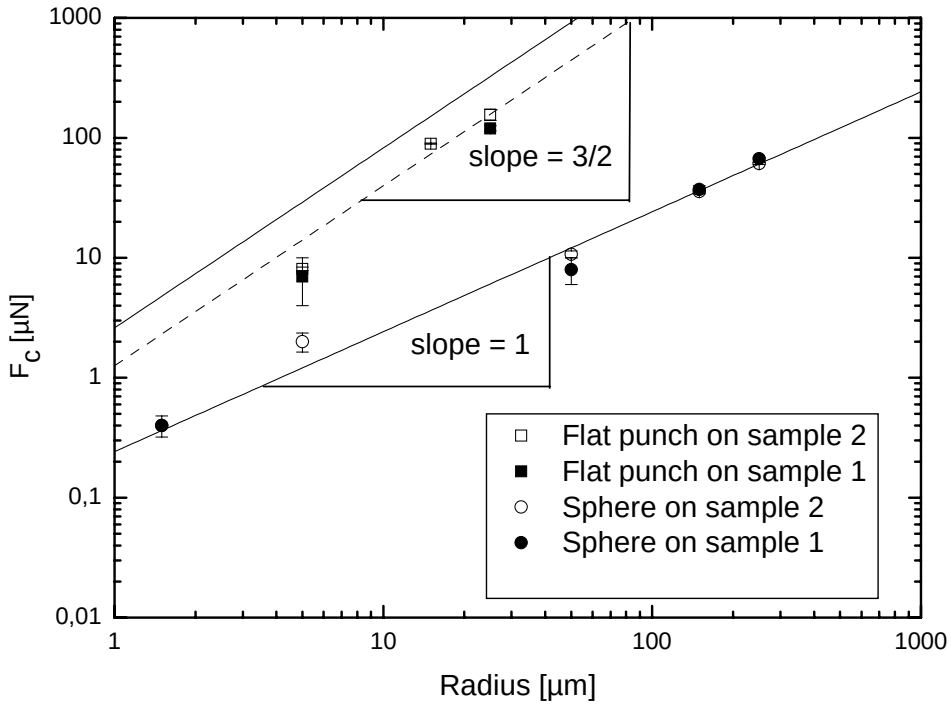

Figure 6-4: Scaling behavior for the pull-off forces of sapphire indenters (sphere, punch) vs. contact element radius on *PDMS*; fitted curves as in [5] with γ=77 mJ m^{-2}

The force value for the 10 µm diameter punch does not match the fitted curve. As adhesion depends more strongly on contamination and punch misalignment, the adhesion forces of the larger punches can be considered more reliable. For a more detailed analysis more measurements with further flat punch tip are necessary. The results show nevertheless, that the scaling model is sufficient to predict the adhesive properties of single microscopic contact elements.

Measurements were also performed on spherical *PDMS* contacts with a radius of curvature of approximately 300 µm and a height of about 450 nm (see section 5.2.5). Comparing the respective adhesion forces with those for tests against a flat reference (see Table 5-5), no difference was found in the case of a flat sapphire punch (r=25 µm) and slightly decreased adhesion was obtained with a sapphire sphere (r=250 µm) This may be explained by the fact that the structure heights of the soft contact elements were low enough to heal out by the surface displacement due to adhesive interactions and form a homogeneous interface [92]. Simply estimating a contact radius at zero pressure from *JKR* according to

$$a_0 = \left(\frac{6\pi R^2 \gamma}{K} \right)^{\frac{1}{3}} \qquad (6\text{-}2)$$

for a *PDMS* sphere against a flat sapphire punch, with a radius of curvature of 300 µm, a work of adhesion of 0.05 J/m² and a reduced stiffness E^* for the sapphire/ *PDMS* system, one obtains a theoretical contact radius of approximately 27 µm, thus exceeding the radius of the contact element. Thus a smooth contact is formed between the indenter tip and the structured surface. If that was not the case, one would expect lower adhesion forces according to *JKR*, due to a decreased reduced radius of curvature of 136 µm instead of 300 µm.

6.3 Collective Adhesion Phenomena on Arrays of Single Contacts

Although the present experimental setup does not allow for direct imaging of the events in the contact zone during an attachment-detachment cycle, the force-displacement data not only provides a kind of fingerprint for every contact system but contains information about the material and the adhesion mechanisms. With the established method, experiments on microscopic fibrillar specimens are possible with precisely controlled loading and unloading speeds, force limits and indentation depths. Data from the cantilever instrument BASALT I was not analyzed, as the measurements were disturbed by noise in the range of the measured forces. An unexpected effect was observed by comparing measurements on intact and disrupted *PDMS* structures (Figure 5-18). Unexpectedly, higher adhesion forces were measured for the damaged pillars. This could be explained by a reduction of stiffness, leading to an easily conforming surface and a healing of the asperities (defect pillars) as described by Hui *et al.*[92]. The effect was not investigated any further in the present study. BASALT I was excluded for the measurements, which were then performed on the NanoXP nanoindenter.

6.3.1 Shallow and Deep Indents

Shallow indents were performed on fibrillar *PDMS* structures (Figure 5-3) to an indentation depth of about 4000 nm (see section 5.3.1). The force-distance curves resemble those of adhesion measurements on the flat reference material, but in contrast the pull-off curve contains several finer peaks suggesting single pull-off events like the detachment of a solitary fibril or of a cluster of fibrils. For a more detailed interpretation it is necessary to estimate the pull-off force for a single fiber. There are two straight forward approaches to this problem.

If a homogeneous stress state is considered for all fibers in contact with a flat punch, the measured pull-off force (Table 5-6). is easily divided by the number of fibers that should be found below the indenter tip. One pillar is found per 100 µm². For a circular flat punch 50 µm wide, the contact zone includes approximately 20 pillars. Assuming a pull-off force of 60 µN under equal load distribution, a single pillar adheres at about 3 µN.
Alternatively the adhesion of a single pillar is calculated by contact mechanics for the respective contact geometry. The radius of curvature is about 100 µm for the examined 5 µm wide pillars. Thus the contact geometry resembles more that of a flat contact than of a true sphere. The force could be estimated using a *JKR* model for a sphere with the radius of curvature of the pillar tips. This approach was rejected due to the limit of optimal contact strength (see section 2.2.6) or the *JKR-DMT* transition. The properties of the contact lie right in the transition regime (Figure 2-14). The adhesion force could alternatively be computed using an ideal contact model by:

$$F = \frac{A\gamma}{\varepsilon} \qquad (6\text{-}3)$$

where A is the area of contact, ε the interatomic equilibrium distance and γ the work of adhesion [7]. As ε has to be estimated, the method is not very reliable. Thus the pull-off force is better calculated by assuming flat punch geometry. In the respective geometry the measured adhesion force for the 50 µm wide circular flat punch against a flat *PDMS* substrate directly enters the calculation. For a single *PDMS* pillar against the flat punch, the configuration is simply reversed, now taking the pillar as the flat punch against a rigid substrate. This step is not fully accurate because the contact area only equals the radius of the punch when the punch is stiffer than the substrate material [5]. As a first order approximation, however, the model is sufficient. The stiffness and work of adhesion for the contacting system are known. The ratio of the pull-off forces for both punch contacts result from.

$$\frac{F_{c1}}{F_{c2}} = \left(\frac{r_1}{r_2}\right)^{\frac{3}{2}} \qquad (6\text{-}4)$$

Where F_{ci} is the pull-off force for punch i and r_i the radius of punch i.
The adhesion force for a single pillar is:

$$F_{c1} = \left(\frac{r_1}{r_2}\right)^{\frac{3}{2}} F_{c2} \qquad (6\text{-}5)$$

With r_2= 25 µm, F_{c2}= 50 µN and r_1=2.5 µm, the force of a single fiber is about 5 µN (exact value 4, 74 µN). Some of the single events observed in the adhesion tests match this computed value quite well. The calculations for a single fiber also yield a value for the theoretical pull-off force for a flat punch against the fibrillar structure if homogeneous loading is assumed for all pillars and if they all are in consequence pulled off simultaneously. The pull-off force then totals 100 µN overestimating the experimental results by less than a factor 2.

The force-displacement curves for adhesion tests with spheres and flat punches on flat and structured polymer specimens differ not only in absolute values but also phenomenologically. As smooth curves are obtained for tests on flat polymer samples, the adhesion peaks for structured surfaces bear a set of finer peaks indicating single pull-off events either for single pillars or for clusters of fibrils (Figure 6-5).

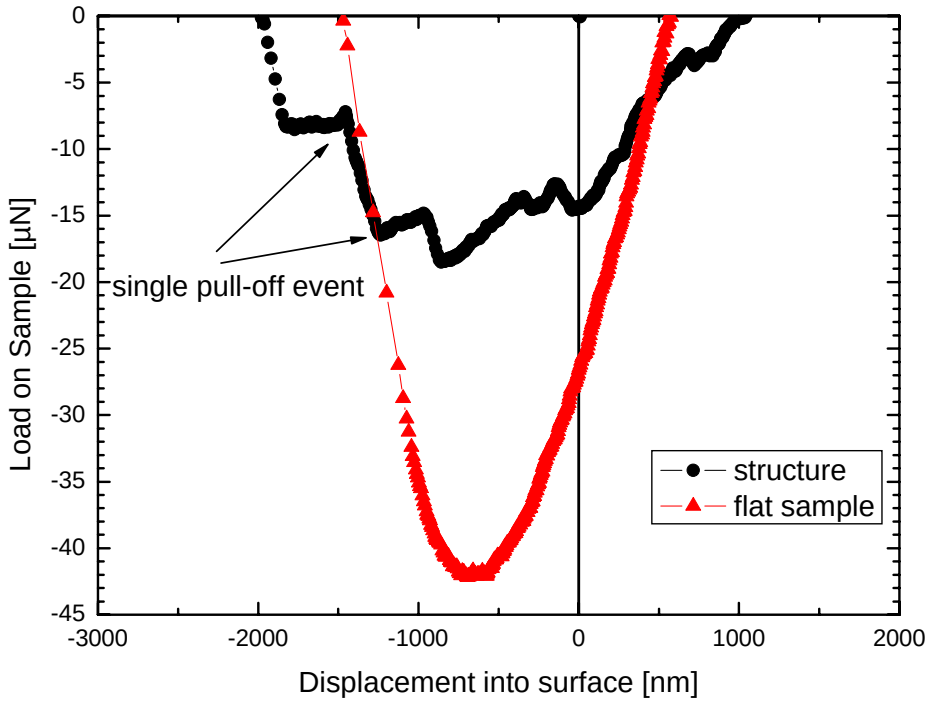

Figure 6-5: Load vs. displacement curves for a flat (smooth curve) and a fibrillar *PDMS* structure measured against a sphere (r=150 µm)

The contact between a fibrillar mat and a sphere is easily modelled using a Winkler elastic foundation approach ([93] as found in [94]) common in engineering mechanics, where the fiber mat is represented by a set of parallel springs and the local pressure is decoupled from the deformations in the surrounding.

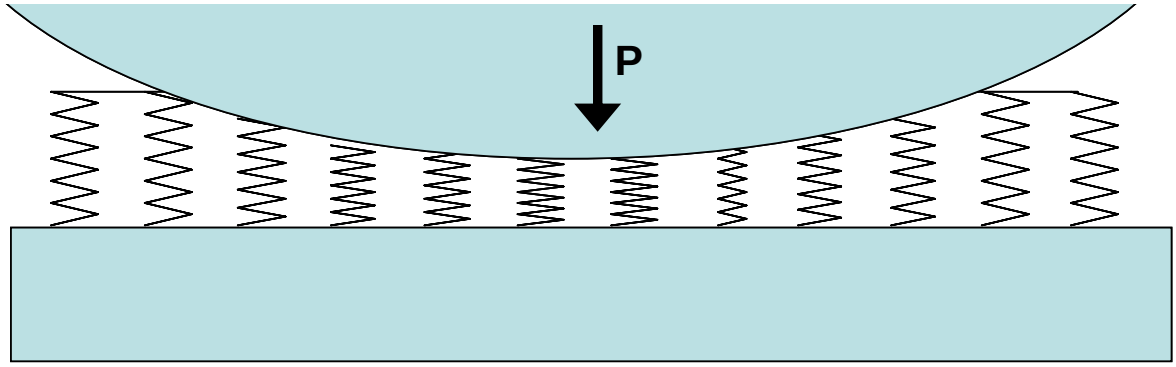

Figure 6-6: Winkler elastic foundation model: The indented surface is represented by a set of decoupled springs adapted from [95]

The local forces are calculated by the deformations of the single springs and a summation over all spring forces provides the total force value. The displacement of a single fiber at distance from the central loading point r_i, indented by a rigid sphere of radius R is calculated as:

$$\delta(r_i) = \delta(0) - R - \sqrt{R^2 - r_i} \qquad (6\text{-}6)$$

The resulting external force on the pillar of length l hence is:

$$F_i = \delta(r_i)\frac{E}{l} \qquad (6\text{-}7)$$

where E is the Young's modulus of the pillar material. The force is set to zero when the applied contact stress exceeds the contact strength or in other words, if the tensile force on the pillar exceeds the pull-off force of the single pillar. From the flat punch experiments the single pillar pull-off force for the given experiments was about 5 µN.
Instead of calculating individual forces for each pillar, the model is simplified by considering simultaneous pillar deformation within annulars of constant width and an inner radius r_i.

The number $n(r_i)$ of pillars within the respective annulus is estimated for a given areal pillar density f:

$$n(r_i) = n(r_{i+1} - r_i)^2 \pi f \qquad (6\text{-}8)$$

The force $F(r_i)$ exerted by such an annulus i is given by the number of pillars within its area times the single force F_i.

$$F(r_i) = n(r_i) F_i \qquad (6\text{-}9)$$

Attractive forces before contact are not considered in the simple model and at the point of initial contact, only one central pillar is in contact with the spherical indenter. The total force is obtained by summing up over all considered annular regions:

$$P = F(0) + \sum_{1}^{i} n(r_i) F(r_i), \qquad (6\text{-}10)$$

Where F(0) accounts for the force of a single central pillar when the calculated number of pillars is zero for the area in the center.
For a precise model all pillars in contact at any point of the experiment have to be accounted for. A cut-off radius is defined for pillars without any contribution to the force within the range of applied indenter displacements. A calculation scheme by A. Wanner [96] was adapted to model a pull-off sequence between a fibrillar structure such as in the present experiment and a sapphire sphere with a radius of 150 µm. The 5 µm wide and 16 µm long pillars are spaced at a lattice parameter of 10 µm in square configuration. Instead of calculating the stiffness from the measured Young's modulus only valid for pure compression, the stiffness of single pillars enters the calculations as a fit parameter. In our case a fit parameter of 1.88 N/m was chosen for the effective spring constant. The detachment force for a single fiber was fitted to match the pull-off forces of the experiment as 2.1 µN. The value expectedly is lower than for the flat punch experiment, as the counter surface (hemisphere r=150µm) is strongly curved. An approximation by *JKR* or *DMT* is not beneficial, as the resulting contact radius of about 10 µm is much bigger than the radius of the pillar tip.

In the given calculation only the unloading sequence is simulated. The data points were calculated for discrete displacement steps of 50 nm. The results were plotted as square data points in Figure 6-7a. The measured data was plotted as a continuous line.

The simulation was redone after refining the model by calculating the exact positions of the pillars that contribute to the measured net force (44 pillars in the present adhesion test). From the positions, the displacements of each individual pillar are obtained according to equation (6-6). The results of the refined calculation are displayed as triangle symbols in Figure 6-7 a.

The force zero value is reached at -1.5 µm displacement for the modelled curves whereas the measured forces turn zero -2 µm (Figure 6-7 b). The model only accounts for the deformation of the pillars, not that of the base. Hence the final pull-off is detected at a greater distance to the origin of displacement than accounted for in the model. The effect is not easily included by reducing the stiffness of the fiber system, as the load transfer of the pillars is not reversible. In the compressive regime the pillars mainly deform in a bending mode only transferring small loads to the base. When the pillars are stretched under tensile load, their stiffness is no longer that of bending but of tensile loading. Thus higher loads are transferred to the base via the pillars leading to a displacement of the base surface. The applied model did not account for the stiffness asymmetry.

Discrete tear- off events are observed in the model as well as in the experimental curve. The coarse model matches the detachment sequence better than the more detailed model. As the position of the spherical tip in the model for individual fixed pillars probably not matches that of the real experiment, the force-displacement data depends strongly on the positioning and a segmental model more adequately describes the experiment. The individual pillar model may be well adapted by iteratively shifting the sphere coordinates relatively to the pillar array.
In the present model the pillars behave linearly. A more complex mechanical behavior, including bending and buckling may easily be implemented for a more detailed simulation of the adhesion tests.

a)

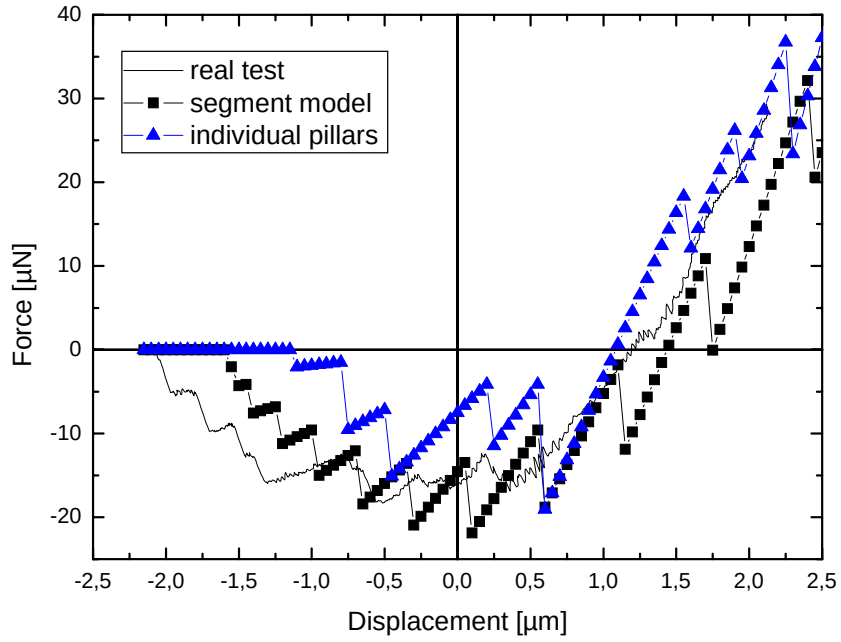

b)

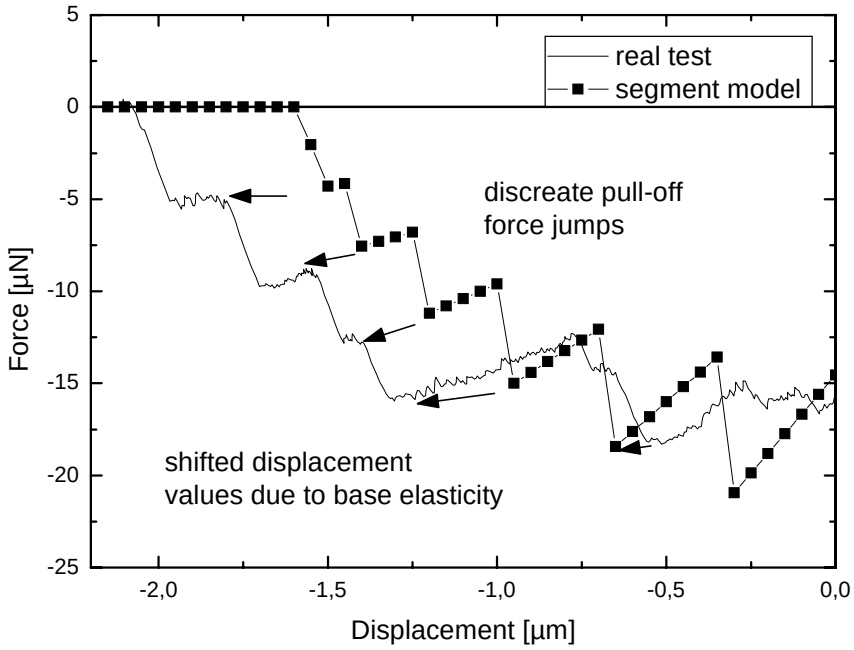

Figure 6-7: a) experimental and model force- displacement curves for an adhesion test on a fibrillar *PDMS* structure (5 µm wide, 16 µm high, 1 pillar/100 µm² measured against a sphere (r=150 µm)): Measured data (continuous curve), segment model (rectangles) and individual pillar model (triangles); b) displacement shift between measured data and segment model

For deep flat punch indents a circle of condensed fibrils marks the indent location (Figure 6-8 a). The condensed fibrils form clusters as the non-condensation design criterion (section 2.2.6) is not fulfilled. As a consequence, the pillars condense when the pillar tips are brought into contact.

For the flat punch, the pillars at the contact edge are pushed outward by the inclined indenter sidewalls. The conical punch base has an apex angle of 60° (Figure 6-8 b). In the present case the distance between two pillar walls is 5µm. A first condensation ring forms when the pillars at the indenter edge are pushed by this distance. By simple trigonometry, the critical penetration depth δ can be calculated by:

$$\delta = d \cos \alpha \qquad (6\text{-}11)$$

where α is the pillar inclination angle and d the distance between two pillar walls.

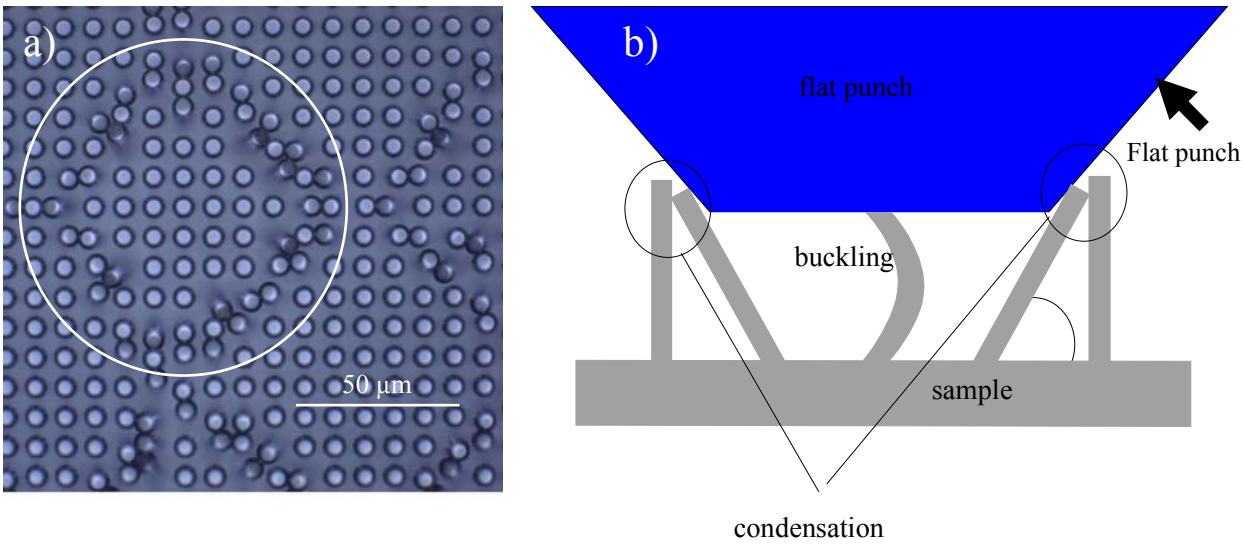

Figure 6-8: a) condensed 5 µm wide fibers of a *PDMS* pillar array on the edge of a 50 µm wide flat punch indent, b) condensation of fibers outside the flat contact area of a conical flat punch (schematic)

Condensation of a first ring of pillars should consequently occur at an indentation depth of roughly 13 µm. The ring was observed experimentally in indentation experiments, performed to an indentation depth of 16 µm (Figure 5-22). In contrast, pillars in the flat contact zone did not condense as can be seen from the micrograph in Figure 6-8 a. Consequently the pillar tips were not moving laterally in contrast to predictions that buckling of the fibrillar structure necessarily results in loss of contact. Two arguments strongly suggest that the contact interfaces are locally fixed. As seen from the contact edge region, the examined pillars tend to condense when the tips are brought into contact. If the tips really were free to move, at least a statistical number of pillar clusters should be found in the contact region. Such clusters were not observed. Stronger evidence is obtained by Euler buckling theory. A pillar with circular cross section buckles under a critical load of:

$$F_{crit} = \frac{n^2 \pi^3 E r^4}{4l^2}, \qquad (6\text{-}12)$$

where n is a factor describing the boundary conditions for the fixation constraints, ranging from 0.5 to 2. As further variables, the radius of the beam r, Young's modulus E and the beam length l enter the equation for the critical load. The fibrils were modelled as beams under compressive load. One end is definitely fixed, as the fibrils are tightly bound to the substrate. The force at the buckling onset is about 200 µN. Assuming that the load is equally distributed on approximately 20 pillars in contact with the flat punch (r=25µm), the buckling force is about 10 µN for each pillar. The pillars are 16 µm long at a radius of 2.5 µN. The material stiffness of the *PDMS* is extracted from a *JKR* fit of the loading segment of the force-distance curves. Solving equation (6-12) for n yields:

$$n = \frac{2l}{r^2}\sqrt{\frac{F_{crit}}{\pi^3 E}} \qquad (6\text{-}13)$$

For an elastic modulus of 2.4 GPa, a pillar length of 16 µm, a pillar radius of 2.5 µm and a critical force of 10 µN, the factor n is 1.9. It thus exceeds the theoretical limit of 1.5, indicating a laterally constrained tip with no translational degree of freedom parallel to the surface (Figure 6-9). According Euler buckling theory, the pillar tips hence are locally fixed.

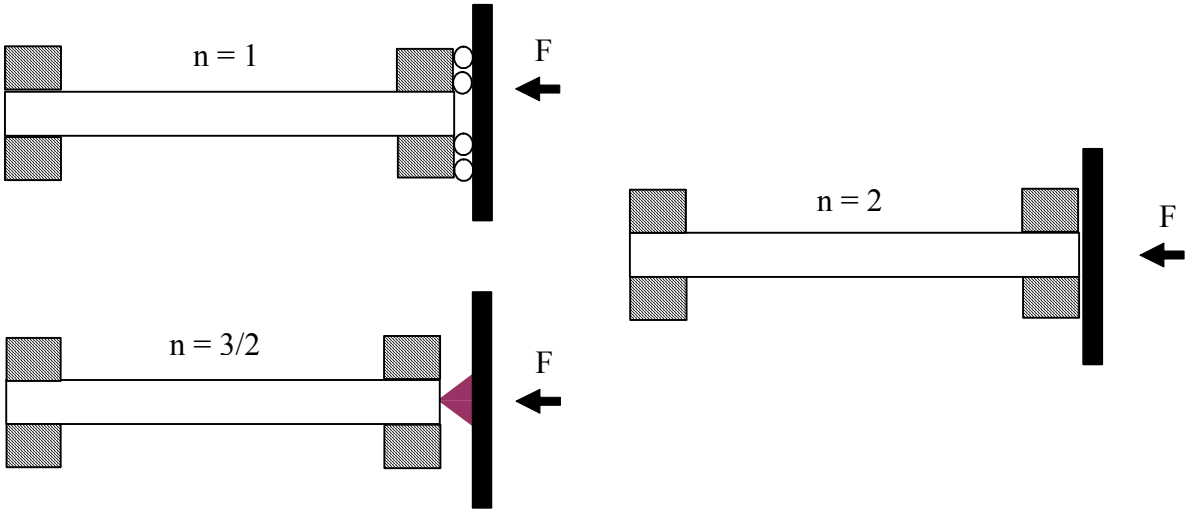

Figure 6-9: Different end constraint factors n for a beam loaded in compression
(adapted from [79] page 385)

The pillars beneath the indenter buckle at an indentation depth of approximately 6 µm. Going to deeper indentation depth, no force plateau as common for the buckling of a single bar is observed, but the load continuously increases. This may be explained by steric constraints of neighboring pillars. In contrast to results by Glassmaker *et al.* [3], the measured adhesion forces at pull-off are practically as high as for shallow indentations without buckling Table 5-6). Hence, buckling effects may not be as threatening to attachment as recently considered. They obviously depend on the respective design of the structures and on the loading conditions. In order to investigate the loading state of the pillars in the experiments, the average maximum contact load for a range of maximum penetration depths was determined Table 5-6). The load values were normalized by the areal density of 20 % and plotted vs. the respective average maximum penetration depths (Figure 6-10).

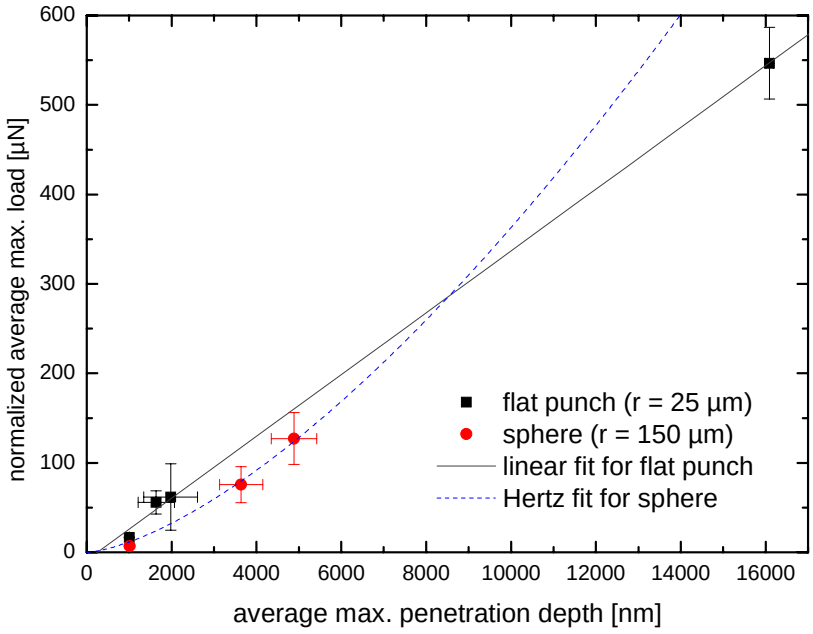

Figure 6-10: average max. load vs. average max. normalized penetration depth by areal coverage of 20 %; fit: lines of equal contact sriffness

For a flat sample the force value is divided by 5. The data was fitted for perpendicular compression. For the punch the force is linearly proportional to the displacement ($\delta \sim P$), whereas an exponential relation is obtained for a hemisphere ($\delta \sim P^{2/3}$) by combining equations (2-1) and (2-4). The data is fit well by these proportionalities. Hence the structures are assumed to be loaded in compression and not in bending. The reason for the reduced stiffness of the structured surface compared to the flat substrates lies in the reduced density and not in the bending of the fibrils. One data point of the flat punch measurements has to be

discussed separately. At about 16 µm displacement the pillars have buckled and should lead to a reduced contact stiffness. In this post-buckled state, however, the contact stiffness matches that of the unbuckled structures, proposing a steric locking of the pillars by neighboring structures. This locking could also contribute to the localization of the contact zones.

6.3.2 Measurements on SU-8 Structures

The effective work of adhesion on structured SU-8 was determined by a Basalt II measurement as 1 mJ/m² (see section 5.3.2) compared to values exceeding 70 mJ/m² in *PDMS* (see section 6.2.3). The obtainable adhesion forces are below the Nanoindenter XP range for the available indenter tip sizes. The strongly reduced work of adhesion may well be a result of the surface roughness observed on the contact element tips (Figure 6-11).

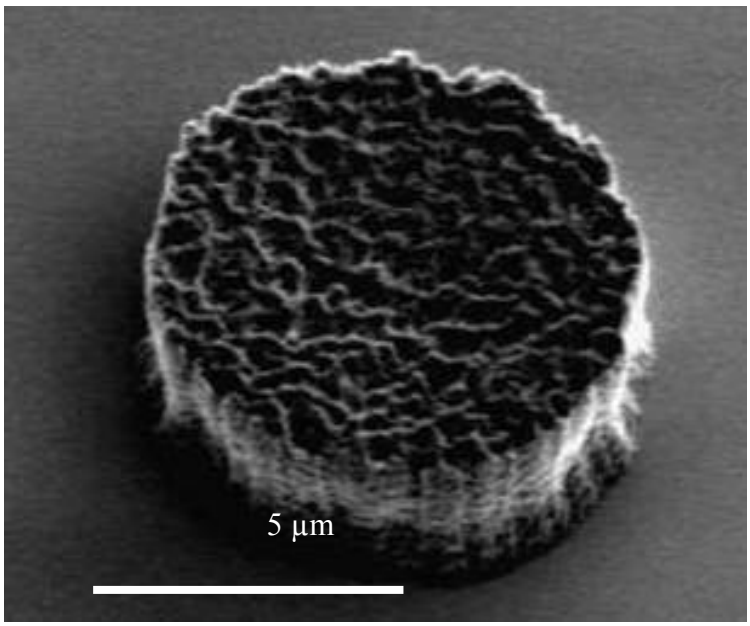

Figure 6-11: Surface roughness on synchrotron lithographic structure

This effect is well established in contact mechanics [18, 49, 92]. If the material is too stiff to adapt to the counter surface roughness by deformation, only localized contacts are obtained. In consequence the effective pull-off force is decreased with respect to a conformal contact and may even result in zero adhesion [18].

7 Summary

By the introduced methods for the production of sophisticated micro contact elements and a technique for precise adhesion measurement with sub-µN and nm resolution in force and displacement, the present work provides tools for a better understanding of the mechanisms in bioinspired adhesion devices.

A *FIB* based fabrication method for micro- and submicrometer-sized contact elements with predefined shape and size has been successfully introduced. For soft contact elements, the respective micro molds were milled by the ion beam followed by replica molding, whereas rigid contact elements were directly cut from commercial nanoindenter or *AFM* or nanoindenter tips. Thus the influence of shape and size on the adhesion of microscopic contact elements was experimentally accessible. The *FIB* method also provided a tool for generating substrates with periodic topology for investigating the effect of roughness on the adhesion of micro contacts. *FIB*- prototyping has proven a universal and efficient tool for the fabrication of specific micro contact prototypes.

Alternatively molds for specifically shaped micro contact elements were achieved by cold micro imprinting on a commercial nanoindenter. Besides, a set of fabrication methods, in particular X-ray photolithography and electrochemically etching, were applied for the fabrication of fibrillar attachment devices without specific tip shapes. An overview is given in Table 5-1 .The adhesion properties of single contacts as well as arrays of such contacts were investigated by performing measurements on a modified commercial MTS NanoXP ™ nanoindenter. A method was established for testing microscopic biomimetic attachment prototypes. By modifying the measuring procedure and the sample support, adhesion data for structured specimens of a several hundreds of µm² were obtained with lateral positioning in the µm range and force resolution in the sub µN regime. Hence the gap between coarse microscopic measurements and localized nanoscopic *AFM* measurements is bridged by the nanoindenter technique.

Adhesion properties for complex prototypes only available in small quantities (e.g. due to high sequential fabrication effort) were accessible with the proposed method. High surface sensitivity and precise force and displacement control enable measurements on fragile

prototypes prone to mechanical damage. The nanoindenter based measurements supplement adhesion testing on the cantilever based testing device Basalt II operating in a comparable force regime but not as accurate in positioning and approaching microscopic sample areas. In contrast to cantilever based devices, the approach is conducted uniaxially and perpendicularly to the sample support. Hence misalignment due to cantilever deflection is excluded.

Scaling effects on the adhesion force of single contacts were experimentally addressed in the present thesis. A variety of rigid spheres and flat punch indenters were tested against smooth polymer surfaces. The experiments on micro sphere and flat punch indenter tips verified theoretical scaling relationships as predicted based on a contact mechanics approach by Spolenak *et al.* [5]. Hence the adhesion pressure of artificial fibrillar attachment devices may be controlled by selecting adequate tip shapes and sizes for the respective application.

The influence of surface properties was addressed by modifying the adhesion forces on a *PDMS* surface before and after different surface treatments. The adhesion forces of oxidized *PDMS* surfaces remained unchanged for different contact angles indicating different degrees of oxidation. Fluorosilanization of a *PDMS* surface led to an unexpected increase in adhesion forces recently also reported by Northen *et al.* [65]. In the present case the adhesion forces doubled by the surface modification. A material stiffness increase to explain the effect was not observed, but it may be explained by increased interfacial friction as suggested by Kim *et al.* [89].

Measurements on fibrillar adhesion devices contributed to a better understanding of the attachment and detachment mechanisms without direct optical observation. The results inspired a first coarse detachment model for a sapphire sphere on a fibrillar polymer device. The observed detachment behavior was in good agreement with a numerical model based on a Winkler elastic foundation approach. The calculated forces match the experimental data well, whereas the displacement values are shifted to lower values in the model, as the model does not account for displacements in the flat backing of the fibrils.

Deep indentations to more than a third of the fibril length were performed for a conical flat punch indenting the fibrillar *PDMS* structure. A persistent ring of condensed fibril was observed around the indent contact area. The pillars at the edge seemed to be pushed outwards by the inclined indenter walls until they touched the next neighbors and stuck to them.

Strikingly such events were never observed within the contact area, giving strong evidence for laterally fixed pillar contacts during the loading-unloading cycle even when the pillars are loaded beyond the buckling force.

In contrast to recently published data [3], buckling of fibrillar attachment devices has proven not to be generally critical to adhesion in fibrillar adhesives. Buckling did not drastically reduce the contact strength of the investigated system. For the given sample, the single contact elements can be considered in static contact with the counter substrate throughout the whole loading-unloading cycle. Buckling presumably only threatens adhesion when the contact elements move out of position. Thus bioinspired adhesives may be adequately designed to exclude the buckling issue.

8 Acknowledgements

First and foremost I would like to express my gratitude to Prof. Dr. Eduard Arzt for the offer of participating in the research one of the most exciting fields at the frontier between physics and biology as a doctoral student. I deeply appreciated the confidence, patience and instructive comments throughout my time at the MPI. I am also very thankful for the constructive suggestions concerning my written thesis and for chairing my thesis committee. I am also sincerely indebted to my advisor Prof. Dr. Ralph Spolenak for his encouragement, his guidance and for his persistent support in Stuttgart and unchanged after responding to his call to the ETH Zürich. I also acknowledge his participation in my thesis committee.

A big thanks goes to Dr. Stanislav Gorb who patiently provided me a glance into the fascinating world of functional morphology. I tremendously appreciated the interesting discussions and inspirations.

I acknowledge all my colleagues in department Arzt for the exceptional warm and convenient atmosphere. This thesis was never possible without the supporting hands and heads surrounding me. I am very grateful for the numerous inspiring discussions. For this opportunity I would like to thank in particular my colleagues Dr. Camilla Mohrdieck, Dr. Andrei Peressadko, Christian Greiner and Alexander Udyansky. I am also very grateful for the persistent and caring support of Dr. Susan Enders in any problems related with nanoindentation.

I feel deeply indebted to the following people, who significantly contributed to the completion of the present study: Birgit Heiland, Steffen Orso and Dr. Ulrike Wegst, guided my first steps in using the *FIB* and *SEM* and always had an open ear for questions, problems and new ideas. Gerrit Huber conducted the *AFM* measurements for this study. Emerson de Souza performed the contact angle measurements and the plasma-oxidations. I also received helpful technical advice from Natascha Sauer, Frank Thiele and Karl-Heinz Berckhemer. Hans Eckstein and his team strongly impressed me by the rapid and straight-forward realisation of my specimen holders. Jens Ulmer from department Spatz at the University of Heidelberg patiently introduced me into the field of photolithography and helped me with the fabrication templates.

I sincerely appreciated the hospitality and inspiring atmosphere at department Gösele (Max-Planck-Institute for Microstructure Physics). In particular I acknowledge the interesting discussion with Dr. Martin Steinhart, Sven Matthias, Danilo Zschech. I am especially indebted to Sven Matthias and Kathrin Schwirn for the fabrication of electrochemically etched templates. A big thanks goes to the Singapore Synchrotron Ligh Source (*SSLS)* for the prompt fabrication of the X-ray-lithography samples.

Furthermore I would like to express my deep gratitude to my fiancée Karin for her patience and confidence in me and my work. At this point I would also like to thank my student fellows Petra Sonnweber-Ribic, Patric Gruber and again Steffen Orso for their encouragement and friendship over many years.
Last but not least, I acknowledge the manifold support by my family and friends.

9 Appendix

A.) Layout for Synchrotron Lithography

Mask Layout for round structures (Figure 9-1 a)

Mask Lattice Parameters *X* [nm]

	Areal Density [ ]			
R [nm]	0.02	0.05	0.1	0.25
1000.00	12533	7927	5605	3545
2000.00	25066	15853	11210	7090
5000.00	62666	39633	28025	17725

Mask Layout for square structures (Figure 9-1 b)

Distance between structures d [nm]

	Areal Density [ ]			
l [nm]	0.02	0.05	0.1	0.25
2000.00	12142	6944	4325	2000
5000.00	30355	17361	10811	5000
10000.00	60711	34721	21623	10000

Mask layout for rectangular structures (Figure 9-1 c)

Distance between structures d [nm]

	Areal Density [ ]				
l [nm]	b[nm]	0.02	0.05	0.1	0.25
2000.00	40000	45038	23283	13073	5096
5000.00	100000	112595	58208	32684	12740
10000.00	200000	225189	116416	65367	25480

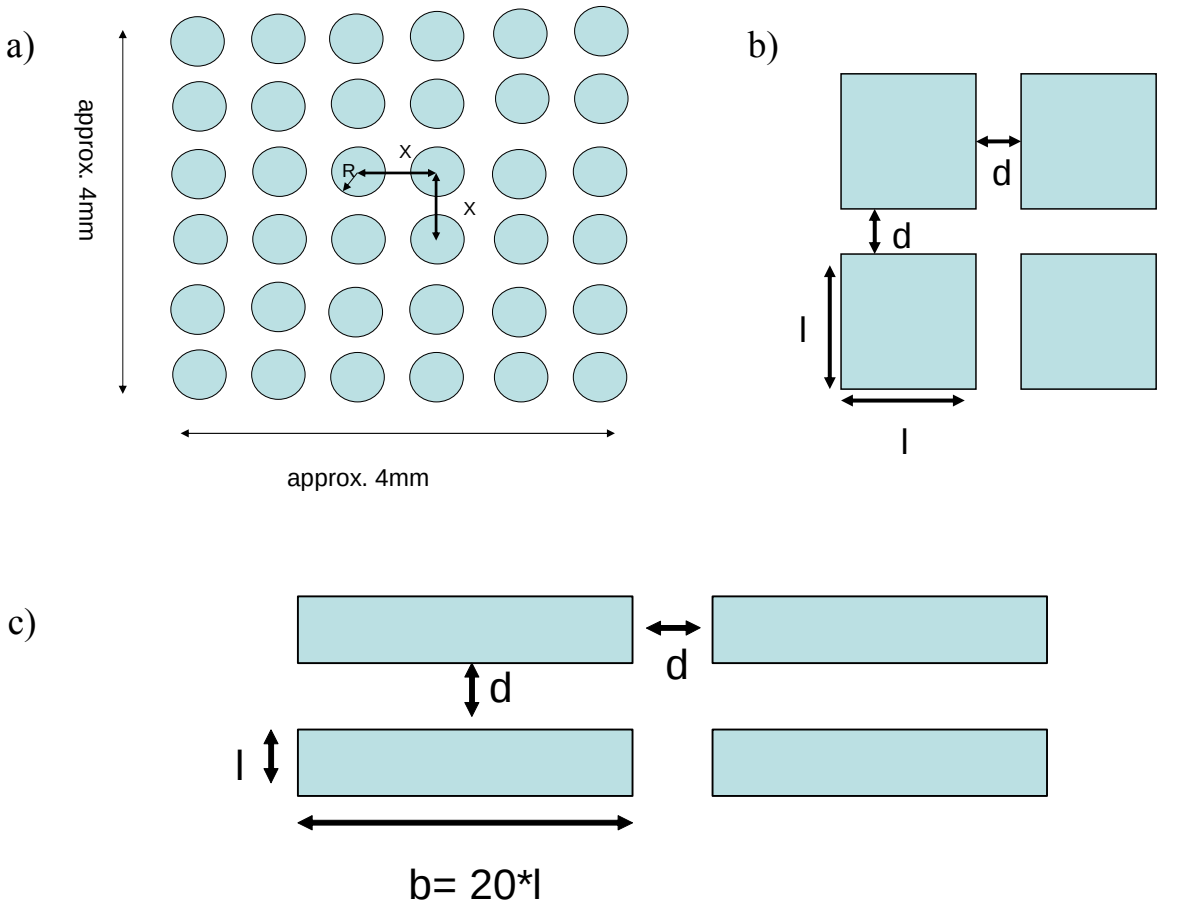

Figure 9-1: Mask layout for X-ray lithography: a) round, b) squares, c) rectangular

A.) FIB-pattern software

The following source code generates the FIB- milling pattern data for a single axisymmetric shape according to the input parameters. The code is given in a early version for reduced complexity. Further codes for more complex tasks like arrays, rectangular shapes etc. are all based on the present program.

```
package indenter;

import java.util.*;
import java.io.File;
import java.util.LinkedList;
import java.io.*;
import java.lang.Math.*;
import java.awt.*;
import java.awt.event.*;

class Item{
    double dwelldef;
    double xdef;
    double ydef;
    Item( double u,double v,double w){dwelldef=u;
xdef=v;
ydef=w;}

}

public class MaskCreator {
static long FilePosition;

  static int Pix = 0; // number of Pixels
  static double fi; // angle pointer
  static double pi = Math.PI; // constant pi
  static double dwell; // calculated dwell time
  static double spot; // Spot size
  static double ra;   // Position pointer radius
static double rlimg; //  local outer limit radius of ring under calculation
  static double ringe; // local inner limit of ring under calculation
  static int mag;      // magnification
  static int sp;       // aperture input
  static double ol;    // overlap
  static double xt;    // x- position
  static double yt;    // y- position
  static double jump; // angle per distance between two adjacent pixels on present
ring
static int func;      // mathematic intensity function
static double r;      // border radius
  static int j;       // dwell time input
  static int m;       // slope factor input
  static int rep;     // number of repetitions
  static double xo;   // initial x
  static double yo;   // initial y
  static double ri;   // inner radius input
  static double ro;   // border radius input
  static double rt;   // half width of ring
  static double ring;  // distance between two adjacent pixels
```

```
   static double fact;
static double seg;    // input for segment
   static double x;
   static double y;
   static double xper;
   static double yper;
   static double pos;
   static double ppm; // Pixel per Micron
   static double i;  // counter variable
   static double z;  // counter variable
static double zero;
   static double pri;
   static double pr;
   static double pro;
   static double pol;
   static double psp;
   static double volumeratio;
   static double rr;
   static double rate=0.15; // sputter rate [µm²/nanoCoulob*s]
   static double depth; // depth input for rectangular shapes
   static double depthcorrection=1; // manual depth correction divisor
   static double xrep;
   static double yrep;
   static double distx;
   static double disty;
static String FileName ="Bufferfile.txt"; // name of mask file
static BufferedReader in = new BufferedReader(new InputStreamReader(System.in));
 static BufferedWriter f;
static FileDialog file;
static ArrayList defaults= new ArrayList();
 static String datastring;
static String addx(double a, double b, double c ) {
    int dwellsav  = (int)a; // value to save as dwellvalue
    if(dwellsav<=0){dwellsav=1;}
    int xsav = (int) b; // value to save as x- coordinate
    int ysav = (int)c; // value to save as y- coordinate
String test =
String.valueOf(dwellsav)+"\t"+String.valueOf(xsav)+"\t"+String.valueOf(ysav);
 return test;
  }
static void writer( double rin, double rlim, boolean dip, int writeswitcher) {
         try {
           f = new BufferedWriter(
              new FileWriter(FileName,true));
                                if (writeswitcher == 1)
                                   {CalculatePosition(rin,rlim,dip);} //setting
dwell time (intensity)
                                 if (writeswitcher == 2)
{f.write("s"+"\n"+MaskCreator.rep+"\n");}
if (writeswitcher == 3) {f.write("          "+"\n");}

if (writeswitcher == 4) {f.write(MaskCreator.datastring+"\n");}

                                f.close();
  } catch (Exception e) {
                                       System.out.println("Error while
calculating Pixel");
                                    }}
   static void Parawriter() {

         try {
           f = new BufferedWriter(
              new FileWriter(FileName+"par",true));
```

```
 f.write("Number of Pixel "+MaskCreator.Pix+"\n");
f.write("Magnification "+MaskCreator.mag+"\n");
  f.write("Aperture "+MaskCreator.psp+"\n");
   f.write("Overlap "+MaskCreator.pol+"\n");
f.write("Inner Radius "+MaskCreator.pri+"\n");
f.write("Outer Radius "+MaskCreator.pr+"\n");
 f.write("Border Radius "+MaskCreator.pro+"\n");
 f.write("Number of Repetitions "+MaskCreator.rep+"\n");
 f.close();
  } catch (Exception e) {
                                        System.out.println("Error while
calculating");
                                      }
         }

static void Spiral() {
// "1 linear function 2 torus 3 sphere indenter 4 constant 5 negative 6 torus
indenter 7 sphere");
                   switch (MaskCreator.func) {
                             case 1:
                               {MaskCreator.dwell =
(java.lang.Math.ceil(MaskCreator.j * MaskCreator.m * (1 - (MaskCreator.ra-
MaskCreator.ringe )/( MaskCreator.rlimg-
MaskCreator.ringe))))/MaskCreator.depthcorrection;break;} //setting dwell time
(intensity)
                                case 2:{
                                                                MaskCreator.dwell =
((java.lang.Math.ceil(MaskCreator.j/rt*

java.lang.Math.sqrt((java.lang.

Math.pow(MaskCreator.rt, 2) - java.lang.Math.pow(MaskCreator.rr,
2))))))/MaskCreator.depthcorrection; break;} //setting dwell time torus
indenter(intensity)
                         case 3:
                               { MaskCreator.dwell = (MaskCreator.j -
                                    java.lang.Math.ceil(1/(MaskCreator.rlimg-
MaskCreator.ringe)*MaskCreator.j*((

java.lang.Math.sqrt(java.lang.
                                    Math.pow((MaskCreator.rlimg-MaskCreator.ringe),
2) - java.lang.Math.pow((MaskCreator.ra-MaskCreator.ringe),
2))))))/MaskCreator.depthcorrection;;break;} //setting dwell time  (intensity)
                               case 4:
                                 {MaskCreator.dwell =
(MaskCreator.j)/MaskCreator.depthcorrection ;break;} //setting dwell time
(intensity)
                                case 5:
                                {MaskCreator.dwell =
(java.lang.Math.ceil(MaskCreator.j * MaskCreator.m * ((ra-
MaskCreator.ringe )/( MaskCreator.rlimg-
MaskCreator.ringe))))/MaskCreator.depthcorrection; break;} //setting dwell time
(intensity)
                               case 6:{
                                 MaskCreator.dwell = (MaskCreator.j-
                                    (java.lang.Math.ceil(MaskCreator.j/rt*

java.lang.Math.sqrt((java.lang.
                                    Math.pow(MaskCreator.rt, 2) -
java.lang.Math.pow(MaskCreator.rr, 2))))))/MaskCreator.depthcorrection; ;break;}
//setting dwell time torus indenter(intensity)
                               case 7:
                                                                { MaskCreator.dwell =
(java.lang.Math.ceil(1/(MaskCreator.rlimg-MaskCreator.ringe)*MaskCreator.j*((
```

```
java.lang.Math.sqrt(java.lang.

Math.pow((MaskCreator.rlimg-MaskCreator.ringe), 2) -
java.lang.Math.pow((MaskCreator.ra-MaskCreator.ringe),
2))))))/MaskCreator.depthcorrection;break;} //setting dwell time  (intensity)
                                                                    case 8:
                                  {MaskCreator.dwell =
(MaskCreator.j)/MaskCreator.depthcorrection ;break;} //setting dwell time
(intensity)
};
              }

              static void DwellCalculator() {

                if (MaskCreator.func == 2) { MaskCreator.depth = (MaskCreator.pr-
MaskCreator.pri)/2;}
               if (MaskCreator.func == 6) { MaskCreator.depth = (MaskCreator.pr-
MaskCreator.pri)/2;}
               if (MaskCreator.func == 3) { MaskCreator.depth = (MaskCreator.pr);}
               if (MaskCreator.func == 7) { MaskCreator.depth = (MaskCreator.pr);}

                                                          double
dwellreference=(1000*(MaskCreator.depth)/(MaskCreator.rate*MaskCreator.psp));

MaskCreator.rep=(int)(java.lang.Math.ceil(dwellreference/(0.0000001*MaskCreator.j*2
.0/(java.lang.Math.sqrt(3.0)*java.lang.Math.pow(MaskCreator.spot*MaskCreator.ol,2))
)));
}
     static void CalculatePosition( double rin, double rlim, boolean dip)throws
Exception {
       // loop for radius
       MaskCreator.rt = (rlim - rin) / 2;
       MaskCreator.rlimg=rlim;
       MaskCreator.ringe=rin;
       MaskCreator.ra=MaskCreator.ringe;
       String test;
           for (i = 1; i <= 2+((MaskCreator.rlimg-
MaskCreator.ringe)/MaskCreator.ring); i++) {

             MaskCreator.jump = (360 / (2 * MaskCreator.ra * Math.PI));
//determines angle/pixel of present circle
MaskCreator.rr = java.lang.Math.abs(MaskCreator.ra-MaskCreator.ringe-
MaskCreator.rt);
             for (z = 0; z<=java.lang.Math.ceil( (MaskCreator.seg)/
(MaskCreator.jump * MaskCreator.ring)); z++) { //loop for the angle position around
present circle
               MaskCreator.y = java.lang.Math.ceil(MaskCreator.ra *
java.lang.Math.sin(MaskCreator.fi * pi / 180)); // sets y- coordinate of present
pixel
               MaskCreator.x = java.lang.Math.ceil(MaskCreator.ra *
java.lang.Math.cos(MaskCreator.fi * pi / 180)); // sets x- coordinate of present
pixel
               MaskCreator.xt = java.lang.Math.ceil(MaskCreator.xo + MaskCreator.x);
               MaskCreator.yt = java.lang.Math.ceil(MaskCreator.yo + MaskCreator.y);
// calculating dwell time and writing to file
               if (dip == true) {
                  Spiral();}//setting dwell
               else {
                  MaskCreator.dwell = (MaskCreator.fact *
MaskCreator.j)/MaskCreator.depthcorrection;} //setting setting constant dwell
Item now = new Item(MaskCreator.dwell,MaskCreator.xt,MaskCreator.yt);
//System.out.println(now);
MaskCreator.defaults.add(now);
```

```
//int len = defaults.size();
                MaskCreator.Pix = MaskCreator.Pix + 1;

//f.write(addx((MaskCreator.dwell),MaskCreator.xt,MaskCreator.yt)+"\n");
//addx((MaskCreator.dwell),MaskCreator.xt,MaskCreator.yt);
// parameters for next pixel on radius
               MaskCreator.fi = MaskCreator.fi + (MaskCreator.jump *
MaskCreator.ring);
             } // end of angle loop and reset of running parameters
MaskCreator.ra=MaskCreator.ra+MaskCreator.ring;
             MaskCreator.fi = 0;
             z = 0;
           } // end of radius loop
          }
static void InputData() throws Exception {

try{
  System.out.println("Please enter FileName ");
      MaskCreator.FileName = (MaskCreator.in.readLine());
  System.out.println("please enter magnification ");
      MaskCreator.mag = Integer.parseInt(MaskCreator.in.readLine());
      System.out.println("please enter aperture ");
      MaskCreator.sp = Integer.parseInt(MaskCreator.in.readLine());
      MaskCreator.psp = sp;
      if (sp == 1) {
        MaskCreator.spot = 0.008; //setting spot diameter
      }
      if (sp == 4) {
        MaskCreator.spot = 0.012; //setting spot diameter
      }
      if (sp == 11) {
        MaskCreator.spot = 0.015; //setting spot diameter
      }
      if (sp == 70) {
        MaskCreator.spot = 0.025; //setting spot diameter
      }
      if (sp == 150) {
        MaskCreator.spot = 0.035; //setting spot diameter
      }
      if (sp == 350) {
        MaskCreator.spot = 0.055; //setting spot diameter
      }
      if (sp == 1000) {
        MaskCreator.spot = 0.08; //setting spot diameter
      }
      if (sp == 2700) {
        MaskCreator.spot = 0.12; //setting spot diameter
      }
      if (sp == 6600) {
        MaskCreator.spot = 0.027; //setting spot diameter
      }
      if (sp == 11500) {
        MaskCreator.spot = 0.5; //setting spot diameter
      }
      System.out.println("please enter overlap in per cent 50.0 ");
      MaskCreator.ol = Double.parseDouble(MaskCreator.in.readLine());
      MaskCreator.pol = MaskCreator.ol;
      MaskCreator.ol = (1 - (MaskCreator.ol * 0.01)); //   calculation overlap
      MaskCreator.ppm = MaskCreator.mag* 0.013473684; //   Pixel Per Micron
calculation
      System.out.println(
          "1 linear function 2 torus 3 sphere indenter 4 constant 5 negative 6
torus indenter 7 sphere 8 amphi pit");
      MaskCreator.func = Integer.parseInt(MaskCreator.in.readLine());
```

```
      System.out.println("please enter inner radius [micron] ");
      MaskCreator.ri = Double.parseDouble(MaskCreator.in.readLine());
      pri = MaskCreator.ri;
      MaskCreator.ri = (MaskCreator.ri * MaskCreator.ppm);

      System.out.println("outer radius [micron] ");
      r = Double.parseDouble(MaskCreator.in.readLine());
      MaskCreator.pr = MaskCreator.r;
      MaskCreator.r = (MaskCreator.r * MaskCreator.ppm);
System.out.println("please enter border radius [micron] ");
      MaskCreator.ro = Double.parseDouble(MaskCreator.in.readLine());
      pro = MaskCreator.ro;
      MaskCreator.ro = (MaskCreator.ro * MaskCreator.ppm);

      System.out.println(
          "please enter Position offset [Pixel] recommended min 400 ");
      MaskCreator.pos = Double.parseDouble(MaskCreator.in.readLine());
      MaskCreator.pos = MaskCreator.pos + MaskCreator.r;

      System.out.println("please enter dwell time [0.1 microsec] ");
      MaskCreator.j = Integer.parseInt(MaskCreator.in.readLine());
      System.out.println("please enter gradient of intensity ");
      MaskCreator.m = Integer.parseInt(MaskCreator.in.readLine());
      System.out.println("please enter intensity factor for plateau");
      MaskCreator.fact = Double.parseDouble(MaskCreator.in.readLine());
      System.out.println("please enter Depth of structure ");
      MaskCreator.depthcorrection = Double.parseDouble(MaskCreator.in.readLine());
      System.out.println("please enter Depth correction divisor");
      MaskCreator.depth = Integer.parseInt(MaskCreator.in.readLine());
      System.out.println("please enter segment [degree] ");
      MaskCreator.seg = Double.parseDouble(MaskCreator.in.readLine());
      MaskCreator.ra = 0.000000000001;
      MaskCreator.rt = (MaskCreator.r - MaskCreator.ri) / 2;

      System.out.println("please enter Number of structures in x ");
      MaskCreator.xrep = Double.parseDouble(MaskCreator.in.readLine());
      System.out.println("please enter Number of structures in y ");
      MaskCreator.yrep = Double.parseDouble(MaskCreator.in.readLine());
      System.out.println("please enter shift distance in x [µm] ");
      MaskCreator.distx = Double.parseDouble(MaskCreator.in.readLine());
      System.out.println("please enter shift distance in y [µm] ");
      MaskCreator.disty = Double.parseDouble(MaskCreator.in.readLine());
      MaskCreator.distx = (MaskCreator.distx * MaskCreator.ppm);
MaskCreator.disty = (MaskCreator.disty * MaskCreator.ppm);

      MaskCreator.ring = (MaskCreator.ol * MaskCreator.spot * MaskCreator.ppm); //
calculation of overlap distance

// starting point

      MaskCreator.xo = MaskCreator.pos;
      MaskCreator.yo = MaskCreator.pos;
      MaskCreator.xper = MaskCreator.xo;
      MaskCreator.yper = MaskCreator.yo;

      MaskCreator.x = 0; // horizontal line starting position
      MaskCreator.y = 0; // reset of y- values for each structure

    }
catch(Exception e){System.out.println("Fehler bei der Parametereingabe");}
}
  static void DefaultData() throws Exception {
```

```
    try{

          MaskCreator.FileName = "Tester.str";
          MaskCreator.mag = 1000;
    MaskCreator.spot = 0.035; //setting spot diameter
MaskCreator.psp=150;

          MaskCreator.ol = 50;
          MaskCreator.pol = MaskCreator.ol;
          MaskCreator.ol = (1 - (MaskCreator.ol * 0.01)); //     calculation
overlap
          MaskCreator.ppm = MaskCreator.mag * 0.013473684; //    Pixel Per Micron
calculation

          MaskCreator.func = 8;
          MaskCreator.ri =0.5;
          pri = MaskCreator.ri;
          MaskCreator.ri = (MaskCreator.ri * MaskCreator.ppm);
          r = 2;
          MaskCreator.pr = MaskCreator.r;
          MaskCreator.r = (MaskCreator.r * MaskCreator.ppm);

          MaskCreator.ro = 2;
          pro = MaskCreator.ro;
          MaskCreator.ro = (MaskCreator.ro * MaskCreator.ppm);
          MaskCreator.pos = 0;
          MaskCreator.pos = MaskCreator.pos + MaskCreator.r;
          MaskCreator.xrep=3;
           MaskCreator.yrep=3;
           MaskCreator.distx=10;
            MaskCreator.disty=10;

MaskCreator.distx = (MaskCreator.distx * MaskCreator.ppm);
MaskCreator.disty = (MaskCreator.disty * MaskCreator.ppm);
          MaskCreator.j = 1000;

          MaskCreator.m = 1;

          MaskCreator.fact = 1;

          MaskCreator.rep = 1;

          MaskCreator.seg = 360;
          MaskCreator.ra = 0.000000000001;
          MaskCreator.depth =29.0/(MaskCreator.pr-MaskCreator.pri)/2;
          MaskCreator.rt = (MaskCreator.r - MaskCreator.ri) / 2;
          MaskCreator.ring = (MaskCreator.ol * MaskCreator.spot * MaskCreator.ppm);
// calculation of overlap distance

// starting point

          MaskCreator.xo = MaskCreator.pos;
          MaskCreator.yo = MaskCreator.pos;
          MaskCreator.xper = MaskCreator.xo;
          MaskCreator.yper = MaskCreator.yo;

          MaskCreator.x = 0; // horizontal line starting position
          MaskCreator.y = 0; // reset of y- values for each structure
        }
    catch(Exception e){System.out.println("Error in Input");}
    }

 static void ArrayMaker(int k,int l){
```

```
for (int h = 0; h< defaults.size();h++){
   Item show = new Item(0,0,0);
                show= (Item) defaults.get(h);
    double xs=(k*MaskCreator.distx+show.xdef);

    double ys=(l*MaskCreator.disty+show.ydef);

    MaskCreator.datastring = addx(show.dwelldef,xs,ys);

MaskCreator.writer(0.0,0.0,true,4);
}
    }

    static void xshift(int l){
      for (int h = 0; h< (int)MaskCreator.xrep;h++){

ArrayMaker(h,l);
   }
}
   static void yshift(){
     for (int l = 0; l< (int)MaskCreator.yrep;l++){

 xshift(l);
    }
    }
  static void WriteHeader(){
  try {
  RandomAccessFile meineDB = new
  RandomAccessFile(FileName,"rw");
// positionieren : Zeichen ab Dateianfang

  meineDB.seek(MaskCreator.FilePosition);
    MaskCreator.Pix = (int)(defaults.size()*MaskCreator.xrep*MaskCreator.yrep);
  String dummy = String.valueOf(MaskCreator.Pix);
meineDB.writeBytes(dummy);

meineDB.close();
  } catch(IOException ioe) {
  System.err.println("Read Error");
  }
  }

  public static void main(String args[]) throws Exception {

    try {
//DefaultData();    //default values for testing
      InputData();  // starts data input
DwellCalculator(); // sets dwell time for each Pixel
writer(0.0,0.0,true,2); //writes Data to file

                  try {
  RandomAccessFile meineDB = new
  RandomAccessFile(FileName,"rw");
// positionieren : Zeichen ab Dateianfang
  MaskCreator.FilePosition=meineDB.length();
  meineDB.close();
   } catch(IOException ioe) {
   System.err.println("Read Error of Random Access file");
   }
writer(0.0,0.0,true,3);
          }catch (Exception e) {
                       System.out.println("Error in Calculating Pixel");
                     }
//--------------------------------------------------------------------------------
```

```
//vertical rows
//---------extension for inner plateau-----------------------------------------------
-----------------------------------------------------

if (MaskCreator.func == 6 || MaskCreator.func == 8 ){
    writer(MaskCreator.zero,MaskCreator.ri,false,1); }


   //   System.out.println("erstes segment");
//-----------------------------------calculation of main structure-----------------
------------------
   writer(MaskCreator.ri,MaskCreator.r,true,1);
   //   System.out.println("zweites segment");
//---------extension for outer plateau-------------------------------------------
-----------------------------------------------------
if (MaskCreator.func ==6 ){
   writer(MaskCreator.r,MaskCreator.ro,false,1);}
  //          System.out.println("drittes segment");
//-------------------------------------------------------------------------------
-------------------------
yshift();
WriteHeader();
  Parawriter(); //writes Parameter File
    }

}
```

C.) Nanoindenter XP Surface Approach for compliant Materials

Modern Nanoindenters are capable of measuring the current contact stiffness by superimposing an oscillation on the linear movement [62]. The indenter is considered in contact when a selected measured property increases abruptly during approach. In practice one defines a limit value, which signals the contact when exceeded. As the standard MTS surface find was not suitable for detecting soft polymer surfaces, a modified surface find segment had to be inserted. First the appropriate channel for surface detection was determined. MTS [97] proposed to use the change in Phase angle of the vibrating measuring head. This value describes the shift between the excitation signal and the sample mechanical response and is detected by a lock-in amplifier. The phase angle changes sensitively with mechanical property variations in the tip surrounding. For the soft polymers no change was detected when going into contact (Figure 9-2).

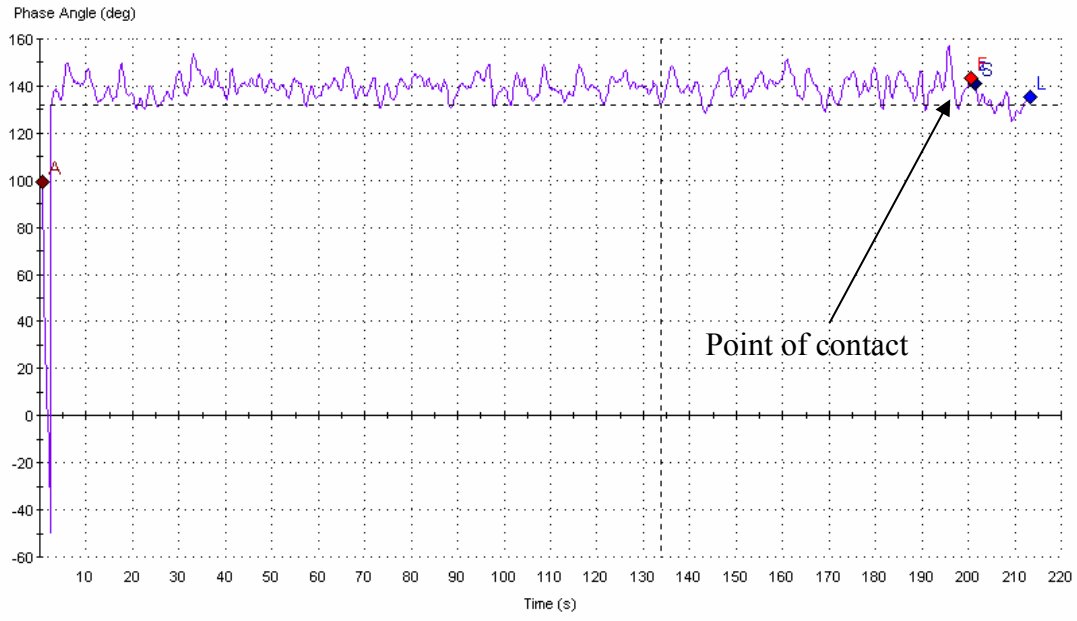

Figure 9-2: Phase Angle as surface Detection criterion (point of contact at approx. 200 s)

Another way of detecting the point of contact is to track a change in the *Harmonic contact stiffness*. The measuring head superimposes a nanometer vibration over the regular movement

of the indenter and registers the stiffness of the contact by reading out the force-displacement gradient of the oscillation. This criterion also was not sufficient for detecting the soft surface (Figure 9-3) using the NanoXP system. It has been successfully applied for detecting soft surfaces as soft as 1 MPa with a Berkovich indenter tip within the high-force resolution SA-2 system [98].

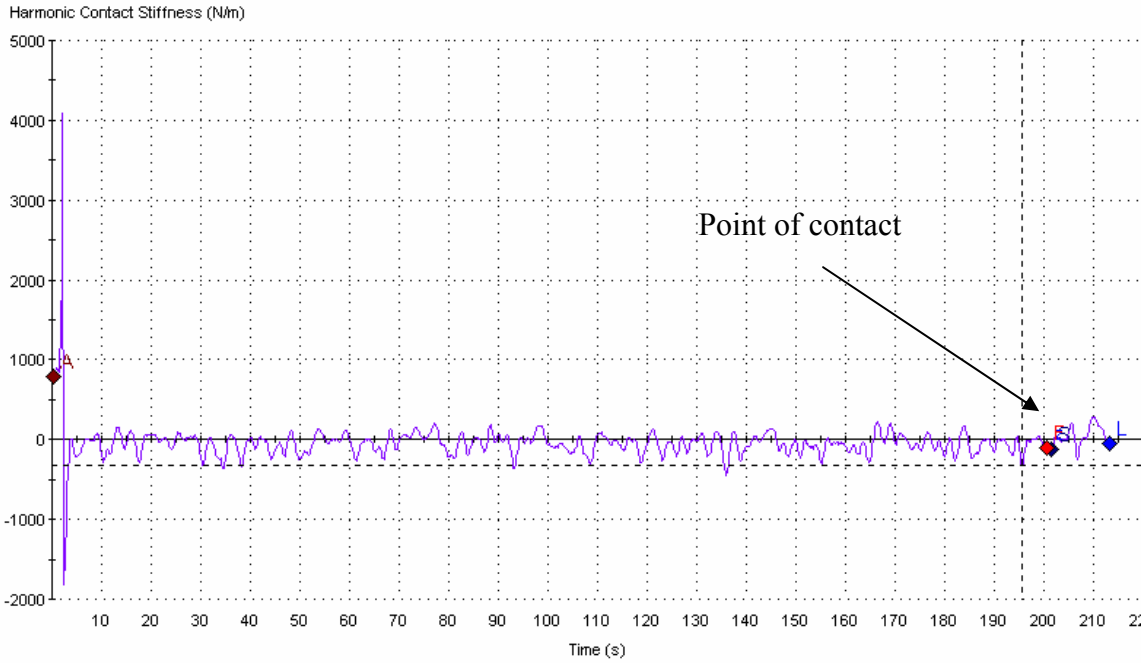

Figure 9-3 Harmonic Contact Stiffness as a surface Detection criterion (point of contact at approx. 200 s)

The data shows no significant change during the whole experiment.
As a consequence, the *Load vs. displacement slope*, a channel tracking the ratio between raw load and raw displacement (Figure 9-4) was used as with the regular methods. After modifying the approach procedure that originally generated too much noise for surface detection, the load vs. displacement sufficiently marks the point of contact (Figure 9-4).

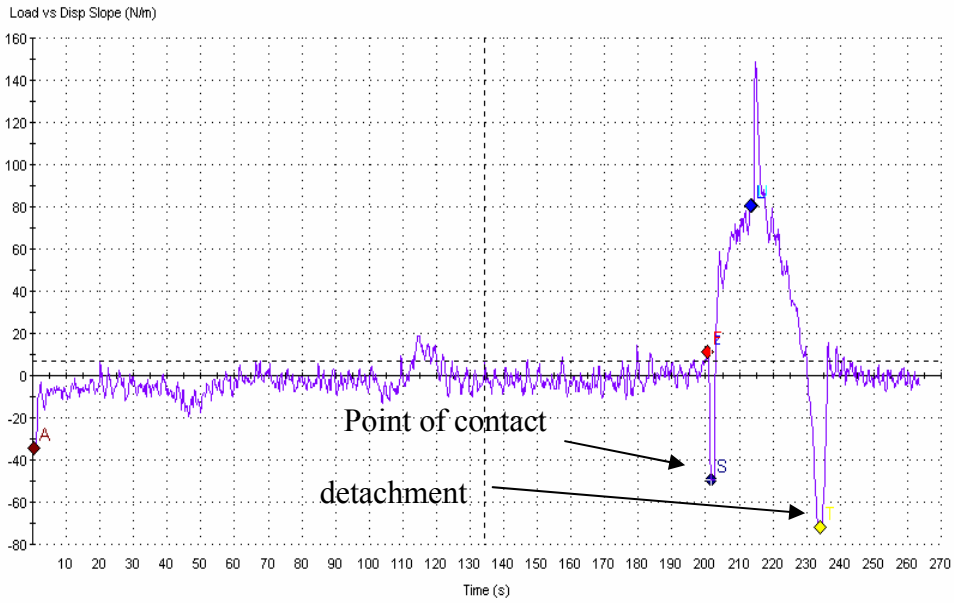

Figure 9-4: Surface Detection for Adhesion Experiments on the load vs. displacement channel

Surface detection for soft materials

As a detection criterion the readout of the load vs. displacement channel was chosen. After the regular surface find and approach, the indenter is retracted again for the distance defined by the *Drawback* input variable and stabilized for a given stabilization time. Then the tip approaches the surface at the velocity given by the *Surface approach speed* input variable. The surface detection is deactivated during a stabilization time and the tip then smoothly continues the approach scanning the load vs. displacement channel for the surface contact peak. When the load vs. displacement slope exceeds the preset *Surface Lock* input value, given as a percentage of 500 N/m, the sample is loaded to a given indentation depth and consequently unloaded. At pull-off the load vs. displacement value drops below zero. The machine determines this point by the detach lock input value, again given in percent of 500 N/m. When loss of contact is detected, the unloading is continued for a preset time before stopping the test and calculating the data. The surface detection parameters have to be determined separately for a specific sample-tip configuration. For coarse surface detection the software requires the input of the surface approach sensitivity. For typical polymer samples (e.g. *PDMS*) the value lies in the range of 10%. After detecting the noise and peak amplitude of external disruption (e.g. shocks) the detection limit is set sufficiently high to exceed noise but as low as possible for most precise surface detection.

In a valid approach, the load vs. displacement is zero and increases continuously with the indentation of the surface. An increase from the very beginning of the approach segment indicates that the tip is already in contact. This problem is solved by increasing the approach distance by changing the Draw Back input value. Typical values for this approach distance range between 30 and 50 µm.

Measuring samples with non-linear behavior

When adhesion measurements are conducted on pillar arrays at high indentation depths, the structures behave linearly, as the pillars buckle [3]. These non-linearities also lead to peaks on the load vs. displacement channel of the nanoindenter (Figure 9-5, see Appendix C). If the method is not altered to correctly interpret these peaks, the end of experiment will be detected incorrectly. A simple way to circumvent this problem is to replace the end of experiment detection by a termination process at a predefined cut-off distance.

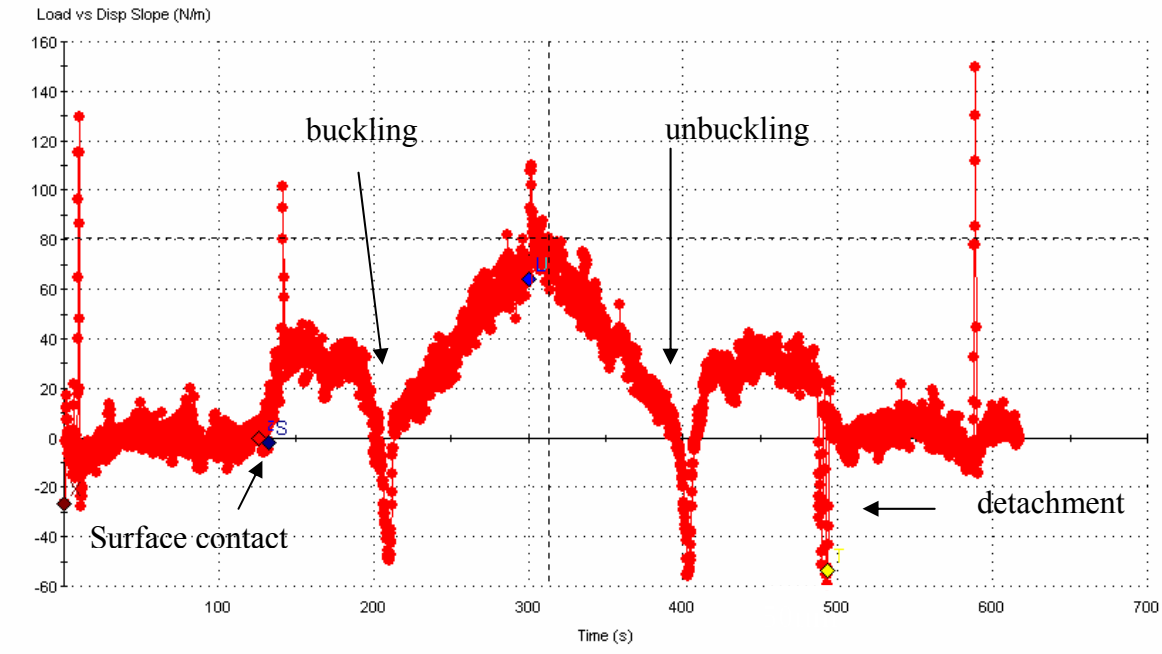

Figure 9-5: Load vs. displacement curve for a test on buckling structures; peaks for surface contact, buckling, unbuckling and detachment during an adhesion test on a fibrillar *PDMS* structure

D.) Data Export and Extraction of Relevant Information

Testworks offers a data export interface for Microsoft excel. There the measurement data is processed and displayed. A software macro was created for automated data extraction. When activated, the macro clips the data to seven columns containing the displacement into surface, the load on sample, the drift compensated load, the raw displacement, the raw load, the time and the load vs. displacement slope. The data of each test is saved in a separate text file import compatible to a fitting tool programmed by A. Peressadko. The macro also extracts important adhesion characteristics and saves them to a collective chart. The Pull-off force is found as the minimum of the total force data, and the local force minimum in the loading segment yields the Pull-in force. The values are listed for the single tests as well as a mean value and the standard deviation. The program also determins the distance, over which the indenter encounters attractive forces before contact (pull-in distance). The chart lists the pull-in force, the adhesion force, the ratio between adhesion and pull-in force, the maximum load and indentation depth and the pull-in distance. It also contains the tip geometry.

Test	Pull-in force [µN]	ratio Pc/Pi [µN]	Pull-off force [µN]	Max. load [µN]	max. penetration depth [nm]	pull-in distance[nm]	
Test 025	-18.1	8.9	-161.4	84.0	1001.5	-279.5	
Test 024	-18.9	8.6	-161.8	83.2	1005.0	-311.5	mean pull-off force[µN]
Test 023	-18.9	8.5	-161.0	84.9	1005.7	-285.9	-161.4
Test 022	-19.1	8.4	-160.8	84.0	1002.0	-290.3	Standard deviation
Test 021	-18.9	8.5	-161.0	84.3	1005.6	-289.0	0.6
Test 020	-19.0	8.5	-161.6	83.3	1003.9	-285.3	mean pull-in force[µN]
Test 019	-19.0	8.5	-160.5	83.5	1004.6	-292.2	-18.7
Test 018	-17.8	9.1	-161.2	85.2	1007.2	-270.4	Standard deviation
Test 017	-18.7	8.6	-161.7	83.3	1005.1	-289.2	0.4
Test 016	-18.3	8.8	-160.7	82.6	1002.8	-280.6	Mean Pc/Pi[µN]
Test 015	-19.0	8.5	-161.8	83.8	1009.3	-288.8	8.6
Test 014	-18.1	8.9	-161.7	83.5	1000.7	-328.1	Standard deviation Pc/Pi
Test 013	-18.7	8.6	-161.4	83.7	1005.9	-284.7	0.2
Test 012	-18.8	8.6	-162.0	84.0	1002.0	-285.0	mean max. load[µN]
Test 011	-18.5	8.7	-161.0	83.9	1002.9	-275.1	83.7
Test 010	-19.1	8.5	-161.3	82.7	1004.7	-296.6	Standard deviation
Test 009	-18.6	8.6	-160.8	84.8	1004.4	-286.0	0.7
Test 008	-19.6	8.3	-162.8	83.0	1003.6	-312.5	mean max. penetration [nm]
Test 007	-18.9	8.5	-160.7	84.0	1003.2	-293.6	1004.2
Test 006	-18.8	8.6	-162.1	83.9	1003.0	-295.8	Standard deviation
Test 005	-18.4	8.8	-161.7	83.9	1005.8	-279.0	2.0
Test 004	-18.9	8.6	-161.5	83.1	1007.2	-314.9	mean Pull-in distance [nm]
Test 003	-19.2	8.4	-161.3	82.5	1005.2	-328.4	-292.7
Test 002	-18.5	8.7	-161.2	83.1	1002.5	-288.8	Standard deviation
Test 001	-18.3	8.9	-162.6	84.8	1002.0	-285.6	15.1
							Tip punch 50

Figure 9-6: Automatically generated result report for 25 tests with a sapphire punch (r=25µm) on a flat *PDMS* substrate

The test data reports as in Figure 9-6 is automatically generated from the exported TestWorks measurements by the following visual basic script:

```
Sub Evaluation()

' clip Makro
' hot key: Strg+e
'
 Sheets("Results").Select
 tip = Cells(3, 8).Value
 Sheets(Array("Required Inputs", "Inputs Editable Post Test", "Results", "Tabelle1")).Select
 ActiveWindow.SelectedSheets.Delete

' deletes not needed data sheets

scount = Sheets.Count
 fileSaveName = Application.GetSaveAsFilename(ActiveSheet.Name & ".xp")
If fileSaveName <> False Then
 MsgBox "Save as " & fileSaveName
End If

' determins path for saving data

Worksheets.Add after:=Sheets(scount)
sdata = scount + 1

For i = 1 To scount
 Worksheets(i).Activate
Columns("A:A").Select
 Selection.Delete Shift:=xlToLeft
 Columns("E:E").Select
 Selection.Delete Shift:=xlToLeft
 Rows("1:2").Select
 Selection.Delete Shift:=xlUp
 Range("G10").Select
 Set myRange = Worksheets(i).Range("C:C")
 answer = Application.WorksheetFunction.Min(myRange)
 limitanswer = Application.WorksheetFunction.Max(myRange)
 ' finds the datapoint for max indentation load
 addrow = Cells.Find(What:=limitanswer).Row
 addcol = Cells.Find(What:=limitanswer).Column
 ' markers for max. indentation load
 maxforce = Cells(addrow, addcol).Value
 maxpenetration = Cells(addrow, (addcol - 2)).Value
 pulldist = Cells(1, 1).Value
 Set localRange = Worksheets(i).Range(Cells(1, 3), Cells(addrow, addcol))
 localanswer = Application.WorksheetFunction.Min(localRange)
```

```
 Worksheets(sdata).Cells(i + 1, 1).FormulaR1C1 = ActiveSheet.Name
 Worksheets(sdata).Cells(i + 1, 4).Value = answer ' pull-off
 Worksheets(sdata).Cells(i + 1, 2).Value = localanswer 'pull-in
 Worksheets(sdata).Cells(i + 1, 3).Value = answer / localanswer
Worksheets(sdata).Cells(i + 1, 5).Value = maxforce
Worksheets(sdata).Cells(i + 1, 6).Value = maxpenetration
Worksheets(sdata).Cells(i + 1, 7).Value = pulldist

fileSaveName = (ActiveSheet.Name & ".xp")
 ActiveWorkbook.SaveAs Filename:=fileSaveName, FileFormat _
 :=xlText, CreateBackup:=True
 Next I          'clips each data sheet extracts raw data and saves it to text file format .xp
Worksheets(sdata).Cells(1, 1).FormulaR1C1 = "Test"
Worksheets(sdata).Cells(1, 4).FormulaR1C1 = "Pull-off force [µN]"
Worksheets(sdata).Cells(1, 2).FormulaR1C1 = "Pull-in force[µN]"
Worksheets(sdata).Cells(1, 3).FormulaR1C1 = "ratio Pc/Pi[µN]"
Worksheets(sdata).Cells(1, 7).FormulaR1C1 = "pull-in distance[nm]"
Worksheets(sdata).Cells(3, 8).FormulaR1C1 = "mean pull-off force[µN]"
Worksheets(sdata).Cells(4, 8).FormulaR1C1 = "=AVERAGE(C[-4])"
Worksheets(sdata).Cells(5, 8).FormulaR1C1 = "Standard deviation"
Worksheets(sdata).Cells(6, 8).FormulaR1C1 = "=STDEV(C[-4])"
Worksheets(sdata).Cells(7, 8).FormulaR1C1 = "mean pull-in force[µN]"
Worksheets(sdata).Cells(8, 8).FormulaR1C1 = "=AVERAGE(C[-6])"
Worksheets(sdata).Cells(9, 8).FormulaR1C1 = "Standard deviation"
Worksheets(sdata).Cells(10, 8).FormulaR1C1 = "=STDEV(C[-6])"
Worksheets(sdata).Cells(11, 8).FormulaR1C1 = "Mean Pc/Pi[µN]"
Worksheets(sdata).Cells(12, 8).FormulaR1C1 = "=AVERAGE(C[-5])"
Worksheets(sdata).Cells(13, 8).FormulaR1C1 = "Standard deviation Pc/Pi"
Worksheets(sdata).Cells(14, 8).FormulaR1C1 = "=STDEV(C[-5])"
 Worksheets(sdata).Cells(1, 5).FormulaR1C1 = "Max. load [µN]"
 Worksheets(sdata).Cells(1, 6).FormulaR1C1 = "max. penetration depth [nm]"
Worksheets(sdata).Cells(15, 8).FormulaR1C1 = "mean max. load[µN]"
Worksheets(sdata).Cells(16, 8).FormulaR1C1 = "=AVERAGE(C[-3])"
Worksheets(sdata).Cells(17, 8).FormulaR1C1 = "Standard deviation"
Worksheets(sdata).Cells(18, 8).FormulaR1C1 = "=STDEV(C[-3])"
Worksheets(sdata).Cells(19, 8).FormulaR1C1 = " mean max. penetration [nm]"
Worksheets(sdata).Cells(20, 8).FormulaR1C1 = "=AVERAGE(C[-2])"
Worksheets(sdata).Cells(21, 8).FormulaR1C1 = "Standard deviation"
Worksheets(sdata).Cells(22, 8).FormulaR1C1 = "=STDEV(C[-2])"
Worksheets(sdata).Cells(23, 8).FormulaR1C1 = "mean Pull-in distance [nm]"
Worksheets(sdata).Cells(24, 8).FormulaR1C1 = "=AVERAGE(C[-1])"
Worksheets(sdata).Cells(25, 8).FormulaR1C1 = "Standard deviation"
Worksheets(sdata).Cells(26, 8).FormulaR1C1 = "=STDEV(C[-1])"
Worksheets(sdata).Cells(27, 8).FormulaR1C1 = "Tip"
Worksheets(sdata).Cells(28, 8).FormulaR1C1 = tip
 Worksheets(sdata).Activate
 Columns("B:H").Select
 Selection.NumberFormat = "0.0"

Columns("A:G").Select
 Selection.Columns.AutoFit
```

```
 Worksheets(sdata).Activate
 fileSaveName = ("adhesion forces.xp")
 ActiveWorkbook.SaveAs Filename:=fileSaveName, FileFormat _
 :=xlText, CreateBackup:=True
' generates result sheet
End sub
```

10 References

[1] Arzt E, Enders S, Gorb S. Towards a micromechanical understanding of biological surface devices. Zeitschrift fur Metallkunde 2002;93:345.

[2] Autumn K, Sitti M, Liang YCA, Peattie AM, Hansen WR, Sponberg S, Kenny TW, Fearing R, Israelachvili JN, Full RJ. Evidence for van der Waals adhesion in gecko setae. Proc. Natl. Acad. Sci. U. S. A 2002;99:12252.

[3] Glassmaker NJ, Jagota A, Hui CY, Kim J. Design of biomimetic fibrillar interfaces: 1. Making contact. J. R. Soc. Lond. Interface 2004;1:23.

[4] Hui C-Y, Glassmaker NJ, T. T, Jagota A. Design of biomimetic fibrillar interfaces: 2. Mechanics of enhanced adhesion. J. R. Soc. Lond. Interface 2004;1:23.

[5] Spolenak R, Gorb S, Gao HJ, Arzt E. Effects of contact shape on the scaling of biological attachments. Proceedings of the Royal Society of London Series A-Mathematical Physical & Engineering Sciences 2005;461:305.

[6] Hansen WR, Autumn K. Evidence for self-cleaning in gecko setae. Proc. Natl. Acad. Sci. U. S. A 2005;102:385.

[7] Spolenak R, Gorb S, Arzt E. Adhesion design maps for bio-inspired attachment systems. Acta Biomaterialia 2005;1:5.

[8] Tornier G. Ein Eidechsenschwanz mit Saugscheibe. Biol. Cbl. 1899;19:549.

[9] Hiller U. Untersuchungen zum Feinbau und zur Funktion der Haftborsten von Reptilien. Z.Morph.Tiere 1968;62:307.

[10] Haase A. Untersuchung über den Bau und die Entwicklung der Haftlappen bei den Geckotiden, thesis. Berlin, 1900.

[11] Homann H. Haften Spinnen an einer Wasserhaut? Naturwissenschaften 1957; 44.:318–319.

[12] Stork NE. Experimental analysis of adhesion of Chrysolina polita (Chrysomelidae, Coleoptera) on a variety of surfaces. J. Exp. Biol. 1980;88.

[13] Bauchhenss E. Die Pulvillen von Calliphora erythrocephala Meig. (Diptera, Brachycera) als Adhaesionsorgane. Zoomorphologie 1979;93:99.

[14] Huber G, Mantz H, Spolenak R, Mecke K, Jacobs K, Gorb SN, Arzt E. Evidence for capillarity contributions to gecko adhesion from single spatula nanomechanical measurements. PNAS 2005;102:16293.

[15] Tian X, Bhushan B. The micro-meniscus effect of a thin liquid film on the static friction of rough surface contact. J. Phys. D: Applied Physics 1996;29:163.

[16] Gorb S. personal communication. Max-Planck-Institute for Metals Research, 2005.

[17] Rollot Y, Regnier S, Guinot JC. Dynamic model of micro-manipulation using adhesion. Comptes Rendus de l Academie des Sciences Serie II Fascicule B-Mecanique Physique Chimie Astronomie 1998;326:469.

[18] Fuller KNG, Tabor D. The effect of surface roughness on the adhesion of elastic solids. Proc. R. Soc. London 1975;345:327.

[19] Hertz H. Über die Berührung fester elastischer Körper. Journal für die reine und angewandte Mathematik 1882;92:156–171.

[20] Maugis D. Adhesion of Spheres: The JKR-DMT Transition Using a Dugdale Model. Journal of Colloid and Interface Science 1992;150:243.

[21] Sneddon IN. The relation between load and penetration in the axisymmetric Boussinesq problem for a punch of arbitrary profile. Int. J. Engng Sci. 1965;3:47.

[22] Boussinesq J. Application des potentiels à l'étude de l'équilibre et du mouvement des solides élastiques. Gauthier Villars, Paris, 1885. p.208.

[23] Johnson KL, Kendall K, Roberts AD. Surface Energy and the Contact of Elastic Solids. Proc.R.Soc. 1971;324:301.
[24] Derjaguin BV, Muller VM, Toporov YP. Effect of Contact Deformation on the Adhesion of Particles. Journal of Colloid & Interface Science 1975;53:314.
[25] Tabor D. Surface forces and surface interactions. J. Coll. Interf. Sci. 1977;58:2.
[26] Dugdale DS. Yielding of steel sheets containing slits. J. Mech. Phys. Solids 1960;8:100.
[27] Barenblatt GI. The mathematical theory of equilibrium cracks in brittle fracture. Adv. Appl. Mech. 1962;7.
[28] Greenwood JA. Adhesion of elastic spheres. Proceedings of the Royal Society of London Series A-Mathematical Physical & Engineering Sciences 1997;453:1277.
[29] Muller B, Yuschenko VM, Derjaguin BV. On the influence of molecular forces on the deformation of an elastic sphere and its sticking to a rigid plane. J. Coll. Interf. Sci. 1980;77:91.
[30] Gao HJ, Yao HM. Shape insensitive optimal adhesion of nanoscale fibrillar structures. Proceedings of the National Academy of Sciences of the United States of America 2004;101:7851.
[31] W.Carpick R, Ogletree DF, Salmeron M. A General Equation for Fitting Contact Area and Friction vs Load Measurements. Journal of Colloid and Interface Science 1999;211:395.
[32] Gent AN, Schultz J. Effect of wetting liquids on the strength of adhesion of viscoelastic materials. Journal of Adhesion 1972;3:281.
[33] Kinloch AJ, Andrews EH. Mechanics of adhesive failure II. Proc.Roy.Soc.London A 1973;332:401.
[34] Kinloch AJ, Andrews EH. Mechanichs of adhesive failure I. Proc.Roy.Soc.London A 1973;332:385.
[35] Maugis D, Barquins M. Fracture mechanics and the adherence of viscoelastic bodies. J. Phys. D: Applied Physics 1978;11:1989.
[36] Johnson KL. Contact Mechanics and the adhesion of viscoelastic spheres. In: Tsukruk VV, Wahl KJ, editors. Microstructure and Microtribology of Polymer Surfaces. Washington D.C.: ACS, 1999. p.25.
[37] Lin YY, Hui CY. Mechanics of Contact and Adhesion between Viscoelastic Spheres: An Analysis of Hysteresis during Loading and Unloading. Journal of Polymer Science Part B-Polymer Physics 2002;40:772.
[38] Hui CY, Baney JM, Kramer EJ. Contact mechanics and adhesion of viscoelastic spheres. Langmuir 1998;14:6570.
[39] Haiat G, Huy MCP, Barthel E. The adhesive contact of viscoelastic spheres. Journal of the Mechanics and Physics of Solids 2003;51:69.
[40] Barthel E, Haiat G. Adhesive contact of viscoelastic spheres: A hand-waving introduction. Journal of Adhesion 2004;80:1.
[41] Barthel E, Haiat G. Approximate model for the adhesive contact of viscoelastic spheres. Langmuir 2002;18:9362.
[42] Barthel E, Roux S. Velocity-Dependent Adherence: An Analytical Approach for JKR and DMT Models. Langmuir 2000;16:8134.
[43] Arzt E, Gorb S, Spolenak R. From micro to nano contacts in biological attachment devices. Proc. Natl. Acad. Sci. U. S. A 2003;100:10603.
[44] Autumn K, Peattie AM. Mechanisms of adhesion in geckos. Integrative & Comparative Biology 2002;42:1081.
[45] Chaudhury MK, Weaver T, Hui CY, Kramer EJ. Adhesive contact of a cylindrical lens and a flat sheet. J.Appl.Phys. 1996;80:30.

[46] Persson BNJ. On the mechanism of adhesion in biological systems. J. Chem. Phys 2003;118:7614.
[47] Peressadko A, Gorb SN. When less is more: Experimental evidence for tenacity enhancement by division of contact area. Journal of Adhesion 2004;80:247.
[48] Peressadko A, Gorb S. Surface profile and friction force generated by insects. In: Boblan IB, R., editor. First International Industrial Conference Bionik, vol. 249. Düsseldorf: VDI Verlag, 2004. p.257.
[49] Persson BNJ, Gorb S. The effect of surface roughness on the adhesion of elastic plates with application to biological systems. Journal of Chemical Physics 2003;119:11437.
[50] Gao HJ, Wang X, Yao HM, Gorb S, Arzt E. Mechanics of hierarchical adhesion structures of geckos. Mechanics of Materials 2005;37:275.
[51] Ghatak A, Mahadevan L, Chung JY, Chaudhury AK, Shenoy V. Peeling from a biomimetically patterned thin elastic film. Proceedings of the Royal Society of London Series A-Mathematical Physical & Engineering Sciences 2004;460:2725.
[52] Lake GJ, Thomas AG. The strength of highly elastic material. Proc.Roy.Soc.London A 1967;A300:108.
[53] Ghatak A, Mahadevan L, Jun Young C, Chaudhury MK, Vijay S. Peeling from a biomimetically patterned thin elastic film. Proceedings of the Royal Society of London Series A-Mathematical Physical & Engineering Sciences 2004;460:2725.
[54] Kendall K. The Adhesion and surface energy of elastic solids. J.Phys.D: Appl.Phys. 1971;4:1186.
[55] Frost HJ, Ashby MF. Mechanism Maps:The Plasticity and Creep of Metals and Ceramics: Pergamon Press, Oxford, 1982.
[56] Dahlquist CA. Tack. Adhesion: Fundamentals and Practice, vol. 142. London: Ministry of Technology, 1969.
[57] Zosel A. Molecular Structure, Mechanical Behavior and Adhesion Performance of PSAs; published online. www.adhesivemag.com, 2000.
[58] Bhushan B. Springer Handbook of Nanotechnology. New York: Springer, 2004. p.609.
[59] Cappella B, Dietler G. Force-distance curves by atomic force microscopy. Surf. Sci. Rep 1999;34:1.
[60] Geim AK, Dubonos SV, Grigorieva IV, Novoselov KS, Zhukov AA, Shapoval SY. Microfabricated adhesive mimicking gecko foot-hair. Nature Materials 2003;2:461.
[61] Sitti M, Fearing RS. Synthetic gecko foot-hair micro/nano-structures as dry adhesives. Journal of Adhesion Science & Technology 2003;17:1055.
[62] Oliver WC, Pharr GM. An improved technique for determining hardness and elastic modulus using load and displacement sensing indentation experiments. Journal of Materials Research 1992;7:1564.
[63] FZK FK. online: www.fzk.de/fzk/ idcplg?IdcService=FZK&node=0329&lang=en. 2005.
[64] Yurdumakan B, Raravikar NR, A. PM, Dhinojwala A. Synthetic gecko foot-hairs from multiwalled carbon nanotubes. ChemComm 2005;30:3799.
[65] Northen MT, Turner KL. A batch fabricated biomimetic dry adhesive. Nanotechnology 2005;16:1159
[66] Steinhart M, Wendorff JH, Wehrspohn RB. Nanotubes a la carte: Wetting of porous templates. Chemphyschem 2003;4:1171.
[67] Steinhart M, Wehrspohn RB, Gosele U, Wendorff JH. Nanotubes by template wetting: A modular assembly system. Angewandte Chemie-International Edition 2004;43:1334.
[68] Wyant JC. Computerized interferometric measurement of surface structure. Proc. Soc. Photo-Opt. Instr. Eng. 1995;2576:122.
[69] Caber P. An interferometric profiler for rough surfaces. Applied Optics 1993;32:3438.

[70] Bhushan B. Surface Roughness Analysis and Measurement Techniques. In: Bhushan B, editor. Modern Tribology Handbook, vol. 1. CRC Press, 2001. p.85 ff.
[71] Yong-Qi F, Ngoi K, Bryan A. Microfabrication of microlens array by focused ion beam technology. Microelectronic Engineering 2000;54:211.
[72] Vasile MJ, Niu Z, Nassar R, Zhang W, Liu S. Focused ion beam milling - depth control for three-dimensional microfabrication. Journal of Vacuum Science & Technology B 1997;15:2350.
[73] Whitesides GM, Ostuni E, Takayama S, Jiang XY, Ingber DE. Soft lithography in biology and biochemistry. Annual Review of Biomedical Engineering 2001;3:335.
[74] LI M, B. C, Gerberich W. Nanoindentation Measurements of Mechanical Properties of Polystyrene Thin Films. Mat. Res. Soc. Symp., vol. 649: Materials Research Society, 2001. p.Q7.21.1.
[75] Bhattacharya AK, Nix WD. Analysis of Elastic And Plastic Deformation Associated with Indentation Testing of Thin Films on Substrates. International Journal of Solids and Structures 1988;24:1287.
[76] Shull KR. Contact mechanics and the adhesion of soft solids. Materials Science & Engineering R-Reports 2002;R36:1.
[77] De Souza E. Personal Communication. Max-Planck-Institute for Metals Research, 2005.
[78] Varenberg M. Modelling the mechanics of AFM cantilevers, personal communication. Max-Planck-Institute for Metals Research, 2005.
[79] Ashby MF. Materials Selection in Mechanical Design. Materials Selection in Mechanical Design. Butterworth Heinemann, 2000. p.32 ff.
[80] Lehmann V, Föll H. Formation mechanism and properties of electrochemically etched trenches in n-type Silicon. J. Electrochem. Soc. 1990;137:653.
[81] Matthias S, Muller F, Jamois C, Wehrspohn RB, Gosele U. Large-area three-dimensional structuring by electrochemical etching and lithography. Advanced Materials 2004;16:2166.
[82] Masuda H, Fukuda K. Ordered metal nanohole arrays made by a two-step replication of honeycomb structures of anodic alumina. Science 1995;268:1466.
[83] Gosset WSS. The probable error of a mean. Biometrika, reprinted on page 11- 34 in “Student’s” Collected Papers,
Edited by E. S. Pearson and JohnWishart with a Foreword by Launce McMullen, Cambridge University Press for the Biometrika Trustees, 1942 1908;6:125.
[84] Jin M, X. F, L. F, Sun T, Zhai J, Li T, Jiang L. Superhydrophobic Aligned Polystyrene Nanotube Films with High Adhesive Force. Advanced Materials Communications 2005;17:1977.
[85] Barquins M, Maugis D. Tackiness of Elastomers. Journal of Adhesion 1981;13:53.
[86] Muller VM. Viscoelastic pull-off of a sphere from flat surface. Colloid Journal 1996;58:612.
[87] White CC, Vanlandingham MR, Drzal PL, Chang NK, Chang SH. Viscoelastic Characterization of Polymers Using Instrumented Indentation. II. Dynamic Testing. Journal of Polymer Science Part B: Polymer Physics 2005;Volume 43:1812.
[88] Bausch GG, Stasser JL, Tonge JS, Owen MJ. Behavior of Plasma-Treated Elastomeric Polydimethylsiloxane Coatings in Aqueous Environment. Plasma and Polymers 1998;3:23.
[89] Kim HI, Koini T, Lee R, Perry S. Systematic Studies of Frictional Properties of Fluorinated Monolayers with Atomic Force Microscopy: Comparison of CF3- and CH3-Terminated Films. Langmuir 1997;13:7192.
[90] Yang FQ, Zhang X, Li JCM. Adhesive Contact between a Rigid Sticky Sphere and an Elastic Half Space. Langmuir 2001;17:716.

[91] Rolland JP, Van Dam RM, Schorzman DA, Quake SR, DeSimone JM. Solvent-Resistant Photocurable "Liquid Teflon" for Microfluidic Device Fabrication. J. Am. Chem. Soc. 2004;126:2322.
[92] Hui CY, Jagota A, Lin YY, Kramer EJ. Constraints on microcontact printing imposed by stamp deformation. Langmuir 2002;18:1394.
[93] Winkler E. Die Lehre von der Elasticitaet und Festigkeit mit besonderer Rücksicht auf ihre Anwendungen in der Technik: Dominicus, Prag, 1867.
[94] Mahrenholtz O. Zur Elastostatik des gebetteten Kreisringbalkens. Technische Mechanik 2004;24:264.
[95] Johnson KL. Contact Mechanics. Cambridge University Press, 1999. p.104.
[96] Wanner A. personal communication- Pillar foundation scheme. Max-Planck-Institute for Metals Research, 2003.
[97] Fajfrowski M. Surface Detection for Polymers, personal communication. 2004.
[98] Riethmüller J. personal communication- surface detection limit on the SA2 nanoindenter. 2005.
[99] Autumn K, Liang YA, Hsieh ST, Zesch W, Wai Pang C, Kenny TW, Fearing R, Full RJ. Adhesive force of a single gecko foot-hair. Nature 2000;405:681.
[100] Huber G, Gorb S, Spolenak R, Arzt E. Resolving the nanoscale adhesion of individual gecko spatulae by atomic force microscopy. biology letters 2005;1:2.

11 Deutsche Zusammenfassung

Die Fähigkeiten bestimmter Echsen, Spinnen und Insekten, aufgrund von Mikrohaftstrukturen an Wänden und Decken entlangzulaufen, hat bereits zu Beginn des letzten Jahrhunderts ernsthafte wissenschaftliche Untersuchungen inspiriert [9, 10]. Zwischenzeitlich wurden die Haftungsorgane der Tiere und deren Haftung genauer untersucht [11-13, 22, 99, 100]. Im Allgemeinen, zeichenen sich die biologischen Haftsysteme durch eine komplexe, oft hierarchisch gegliederte, Mikro- bzw. Nanostruktur auf. Arzt *et al.* [43] konnten zeigen, dass die Aufspaltung größerer Kontakte in kleinere Untereinheiten zu einer Erhöhung der Haftkräfte führt.
Zusätzlich zu den biologischen Untersuchungen wurden von mehreren Forschungsgruppen biomimetische Haftproben hergestellt und getestet ([3, 47, 53, 60, 61, 64, 65, 84] siehe Tabelle 2-3) . Im Hinblick auf technische Einsatzmöglichkeiten solcher Klebstoffe, wurden Leitlinien für die Auslegung geeigneter Haftstrukturen erarbeitet [3-5, 7].

Trotz zahlreicher Arbeiten zur Aufklärung der physikalischen Grundlagen, sind die Einflüsse der Geometrie und des Materials sowie die Haftungsmechanismen nicht erschöpfend geklärt. In der vorliegenden Arbeit wurde ein Verfahren zur Herstellung definiert geformter Mikrokontakte entwickelt und ein Messverfahren vorgestellt, das die Lücke zwischen makroskopischen Haftungsmessungen und sehr feinen, aber auf lokale Effekte beschränkte, Rasterkraftmikroskopie schließt.

Das genannte Strukturierungsverfahren erlaubt sowohl die direkte Herstellung harter Kontaktelemente als auch die Erzeugung von Mikrogussformen für weiche Kontaktelemente (siehe Kapitel 3.1) mittels eines fokussierten Ionenstrahlmikroskops (*FIB*). Der Strahl wird rasternd über das Substrat geführt und trägt abhängig von der Ionendosis ein definiertes Materialvolumen ab. Die Verweildauer des Strahls wird dabei für jede Probenposition so gewählt, dass die gewünschte Struktur freigelegt wird. Ein selbsterstelltes Computerprogramm generiert automatisch entsprechende Maskendateien nach den Vorgaben des Nutzers. Diese werden vom *FIB* direkt eingelesen und mit einem Galliumionenstrahl auf die Probe übertragen. In einer Machbarkeitsstudie wurde ein torisches Kontaktelement auf die Spitze eines Rasterkraftmikroskopfeder geschnitten (Abbildung 5-1 a und b), sowie Gussformen für torische und säulenförmige Kontaktelemente erzeugt (Abbildung 5-1 c und d). Ferner wurde ein Templat für hierarchische Säulenstrukturen hergestellt (Abbildung 3-9).

Desweiteren wurden periodische Wellenstrukturen gefertigt, die eingesetzt werden sollen, um den Einfluss der Rauhigkeit auf die Haftung zu untersuchen (Abbildung 3-1 b). Das Verfahren hat sich als universell einsetzbar und effizient erwiesen, allerdings wurden mit den so hergestellten Proben noch keine Haftungsversuche durchgeführt.

Für weitere Kontaktelemente mit vorbestimmter Form wurde ein Prägeverfahren auf einem handelsüblichen Nanoindenter erprobt. Mit dieser Methode ließen sich Mikrogussformen herstellen, die mit Polydimethylsiloxan (*PDMS*, Sylgard 184, Dow Corning) abgeformt wurden.

Es wurden auch säulenartiger Strukturen ohne definierte Spitzengeometrie mittels Photolithographie, Röntgenstrahllithographie und gerichtetem elektrochemischen Ätzen erzeugt. Eine Übersicht findet sich in Tabelle 5-1. Die Haftungseigenschaften einzelner Kontaktelemente und die Haftung fibrillärer Mikrohaftstrukturen wurden mit einem modifizierten kommerziellen Nanoindenter NanoXP ™ des Herstellers MTS gemessen. Es wurde eine Methode etabliert, um das Haftverhalten mikroskopische biomimetische Prototypen mit hoher Präzision zu untersuchen. Durch die Verwendung eines speziellen Probenhalters und eines eigens entwickelten Messverfahrens, konnte die Haftung von Proben mit einigen hundert Mikrometern Ausdehnung mit einer lateralen Positionierungsgenauigkeit im einfachen Mikrometerbereich gemessen werden. Das Verfahren erreichte eine Kraftauflösung im Submikrometer- und eine Wegmessung im Nanometerbereich. So konnte mit dem Nanoindenterverfahren eine Brücke zwischen den groben makroskopischen Messungen und der Rasterkraftmikroskopie geschlagen werden. Durch die präzise Kraft- und Wegkontrolle lassen sich Untersuchungen an sehr empfindlichen Mikroproben vornehmen, ohne diese zu zerstören.

Mit dem Messverfahren wurde das Skalierungsverhalten der Haftkräfte von mikroskopischen Einzelkontakten untersucht. Es wurden Haftungsmessungen mit verschiedenen Saphirhalbkugeln und Stempeln unterschiedlicher Größe auf einer glatten Silikonoberfläche durchgeführt. In der Kontaktmechanik spielt es bei geringen Eindringtiefen, in erster Nährung, keine Rolle, welcher der beiden Kontaktkörper nachgiebiger ist. Somit beschreibt das Haftverhalten der beschriebenen Messanordnung gleichzeitig die umgekehrte Konfiguration mit einem weichen Kontaktelement auf einem harten Substrat. Durch die Messungen konnten die theoretischen Vorhersagen von Spolenak *et al.* [5] für die Skalierung der Haftkräfte

verifiziert werden. Durch gezielte Wahl von Geometrie und Größe der Kontaktelemente, lassen sich folglich Haftkräfte definiert einstellen.

Der Einfluss von Oberflächenbehandlungen auf die Haftung, beispielsweise durch Oxidation und Silanisierung, wurde ebenfalls mit dem Messverfahren an *PDMS*-Proben untersucht (Kapitel 5.3.2). Bei der Oxidation wurde keine Veränderung des Haftverhaltens festgestellt. Bei der Silanisierung wurde, hingegen aller Erwartungen, eine Verdoppelung der Haftkräfte beobachtet. Dieser Effekt wurde kürzlich auch durch Northen *et al.* [65] beobachtet. In der zitierten Arbeit wurden Änderungen in der Kontaktelementgeometrie als möglicher Grund angeführt. In der vorliegenden Arbeit wurde diese Möglichkeit ausgeschlossen. Stattdessen wurde ein qualitatives Modell vorgeschlagen, welches die Haftkrafterhöhung durch die Reibung zwischen den Kontaktoberflächen erklärt. In der klassischen Kontaktmechanik wird die Grenzfläche als reibungslos angenommen. Basierend auf einer Arbeit von Kim *et al.* [89], wurde eine Erhöhung der Reibung bei den untersuchten silanisierten Oberflächen angenommen, und als mögliche Ursache für die Haftkrafterhöhung aufgezeigt.

Präzise gesteuerte Messungen an mikrofibrillären Haftoberflächen ermöglichten eine detailliertere Beschreibung der Haftungs- und Ablösevorgänge, ohne direkte mikroskopische Beobachtung (Kapitel 5.3).
Basierend auf den Messergebnissen wurde unter Verwendung eines Winklermodells die Ablösung einer fibrillären Kunststoffstruktur von einer Kugeloberfläche beschrieben (Abbildung 6-7). Die gemessenen Kräfte für die einzelnen Ablösevorgänge deckten sich gut mit den Berechnungen. Im Gegensatz dazu, sind die Verschiebungen im Modell etwas niedriger als gemessen. Während im Modell das Substrat als nicht verformbar angenommen wurde, bestand es bei den Experimenten aus dem gleichen Polymer wie die Säulen. Folglich läßt sich die zusätzliche Verschiebung durch die Dehnung des Substrates unter Zuglast erklären.

Das Haftverhalten wurde auch für tiefe Indentationen mit einem flachen, an den Flanken konisch zulaufenden, Stempel auf einer fibrillären *PDMS*- Probe gemessen. Die Proben wurden mindestens bis zu einem Drittel der Säulenlänge indentiert. Bei den vorgegebenen Verformungen kam es zur reversiblen elastischen Knickung der Säulen. Bei den verwendeten Proben wurde ein bleibender Ring von kondensierten Säulen um den Eindruck festgestellt (Abbildung 6-8). Die Säulen am Rand wurden durch die Seitenwände des Indenters seitlich

gegen benachbarte Säulen gedrückt, was zu einer Kondensation der Säulen führte. Es fiel auf, dass solche Verklebungen nie innerhalb der Kontaktfläche beobachtet wurden. Dies wurde als Hinweis dafür gewertet, dass die Säulenspitzen während der gesamten Belastung und Entlastung in Ihrer Kontaktposition fixiert waren. Im Gegensatz zu kürzlich veröffentlichen Ergebnissen [3], konnte bei den durchgeführten tiefen Indentationen keine Reduktion der Haftkräfte gegenüber Versuchen ohne elastische Knickung festgestellt werden. Elastische Knickung stellt also nicht generell ein Problem bei biomimetischen Haftstrukturen dar, muss aber bei der Auslegung künstlicher Haftstrukturen berücksichtigt werden.